Buckling of fluid interfaces laden with plate-like particles

Prakash, Suriya

DOI
10.4233/uuid:5ba69c5b-dc08-4798-a406-3aee970b3b20

Publication date
2025

Document Version
Final published version

Citation (APA)
Prakash, S. (2025). *Buckling of fluid interfaces laden with plate-like particles*. [Dissertation (TU Delft), Delft University of Technology]. https://doi.org/10.4233/uuid:5ba69c5b-dc08-4798-a406-3aee970b3b20

Important note
To cite this publication, please use the final published version (if applicable).
Please check the document version above.

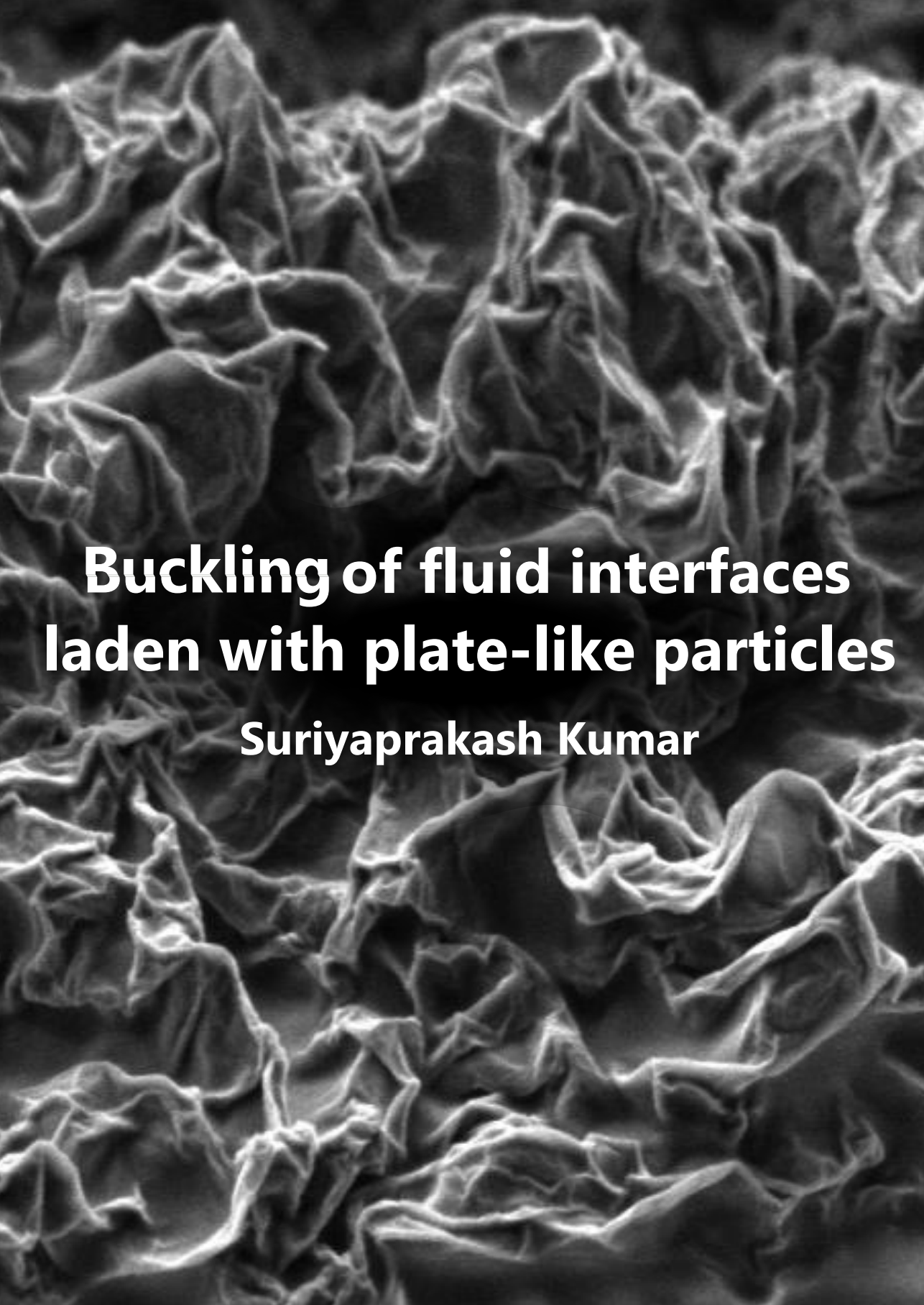

Buckling of fluid interfaces laden with plate-like particles

Suriyaprakash Kumar

Buckling of fluid interfaces laden with plate-like particles

Suriyaprakash KUMAR

Buckling of fluid interfaces laden with plate-like particles

Dissertation

for the purpose of obtaining the degree of doctor
at Delft University of Technology
by the authority of the Rector Magnificus,
Prof.dr.ir. T.H.J.J. van der Hagen,
chair of the Board for Doctorates,
to be defended publicly on
Tuesday 21 October 2025 at 15:00 o'clock

by

Suriyaprakash KUMAR

Master of Science in Mechanical Engineering,
Delft University of Technology, the Netherlands.
Born in Cuddalore, Tamil Nadu, India.

This dissertation has been approved by the promotors.

Composition of the doctoral committee:

Rector Magnificus	chairperson
Dr. L. Botto	Delft University of Technology, promotor
Prof.dr.ir. J.T. Padding	Delft University of Technology, promotor

Independent members:

Prof.dr.ir. J.R. van Ommen	Delft University of Technology
Dr. D.S.W. Tam	Delft University of Technology
Dr. J. de Graaf	Utrecht University
Dr. A. Alicke	Eindhoven University of Technology
Prof.dr. K. Hooman	Delft University of Technology, reserve member

This work was funded by the European Research Council (ERC) under the European Union's Horizon 2020 research and innovation programme (Grant agreement No. 715475, project FlexNanoFlow).

Keywords: Buckling, particles, monolayer, fluid interface, evaporation, spray drying experiments

Printed by: Ridderprint

Cover: Image of buckled graphene oxide capsule.

ISBN: 978-94-6518-140-0
An electronic version of this dissertation is available at
`https://repository.tudelft.nl/`

Contents

Summary

The remarkable properties of 2D nanomaterials make them promising candidates for the development of sustainable energy materials. However, the primary challenge in producing 3D materials from 2D nanosheets lies in the precise control of their microstructure. Previous studies have shown that buckling can be leveraged to control the microstructure of 3D materials assembled from nanosheets. Buckling is achieved by compressing fluid interfaces with adsorbed nanosheets. Therefore, understanding the buckling of fluid interfaces with adsorbed plate-like particles is crucial for producing functional 3D materials from 2D nanosheets. In this dissertation, we focus on two techniques used to control the microstructure of assembled nanosheets: the Langmuir-Blodgett assembly and spray drying.

In the Langmuir-Blodgett assembly, nanosheets adsorbed at planar fluid interfaces are compressed by barriers. The compression results in buckling of the fluid interface laden with a monolayer of nanosheets. To understand the buckling of a monolayer of nanosheets, we studied a simplified model system comprising millimetric Mylar sheets at a fluid-fluid interface. This model system allowed the precise measurement of both the buckling force and the buckling wavelength. The wavelength was found to be of the order of a few particle diameters. We developed a theoretical model based on energy minimization, which agrees well with the experimentally measured buckling force and wavelength. Building on insights from the model systems and accounting for van der Waals interactions between overlapping 2D nanosheets, we proposed a theoretical model to explain the buckling wavelengths observed in monolayers of nanosheets.

In spray drying, the evaporation of water drops containing particles results in the formation of buckled capsules. Previous studies on spherical colloids have shown that evaporation leads to accumulation of particles at the air-water interface. This accumulated particle layer (shell) buckles under further compression as evaporation proceeds. However, the following questions remain

unanswered: (1) how particle adsorption at the interface affects evaporation rate, (2) what criterion governs onset of buckling, (3) how this criterion depends on particles adsorption at the interface, and (4) how the evaporation rate affects the final buckled morphology. To address these questions, we studied the evaporation of a single water drop containing graphene oxide nanosheets deposited on superhydrophobic substrates.

We found that particle adsorption at the interface had a negligible effect on the evaporation rate of drops. We explain this by adapting mathematical models from an analogous electrostatic problem. The model predicts that when the particles are uniformly distributed at the interface and are much smaller than the drop, the evaporation rate is identical to that of a pure water drop. In contrast, the onset of buckling strongly depends on particle adsorption at the interface. To explain this dependence, we modeled the shell as a particle bilayer. The bilayer buckles when the total interfacial tension becomes negative, which is qualitatively in agreement with the experiments. Finally, the buckling wavelength of the dried capsule decreased with increasing evaporation rate. For a fixed solid fraction, faster evaporation results in thinner shells. In thin shells, the low bending energy compared to the stretching energy favors high-curvature deformations, producing shorter buckling wavelengths.

In conclusion, this dissertation advances the fundamental understanding of the buckling of interfaces laden with plate-like particles. The results obtained provide practical ways to control the microstructure of industrially produced 3D materials made from 2D nanosheets.

Samenvatting

De uitzonderlijke eigenschappen van 2D-nanomaterialen maken deze mogelijk geschikt voor de ontwikkeling van duurzame energiematerialen. De voornaamste uitdaging bij het produceren van 3D-structuren uit 2D-nanosheets is het nauwkeurig beheersen van hun microstructuur. Eerdere studies hebben aangetoond dat knikvorming kan worden benut om de microstructuur van 3D-materialen, opgebouwd uit nanosheets, te beheersen. Knikvorming wordt bereikt door vloeistofinterfaces met geadsorbeerde nanosheets samen te drukken. Daarom is het begrijpen van het knikvorming van vloeistofinterfaces met geadsorbeerde plaatvormige deeltjes van cruciaal belang voor het vervaardigen van functionele 3D-materialen uit 2D-nanosheets. In dit proefschrift richten we ons op twee technieken die worden gebruikt om de microstructuur van geassembleerde nanosheets te beheersen: de Langmuir-Blodgett-assemblage en sproeidrogen.

Bij de Langmuir-Blodgett-assemblage worden nanosheets die aan vlakke vloeistofgrensvlakken zijn geadsorbeerd, gecomprimeerd door barrières. De compressie resulteert in knikvorming van het vloeistofgrensvlak, beladen met een monolaag van nanosheets. Om de knikvorming van een monolaag bestaande uit nanosheets te begrijpen, bestudeerden we een vereenvoudigd modelsysteem bestaande uit millimetrische Mylar-vellen op een vloeistof-vloeistofgrensvlak. Dit modelsysteem maakte het nauwkeurig meten van zowel de buigkracht als de golflengte mogelijk. De golflengte bleek ter grootte te zijn van enkele deeltjesdiameters. We ontwikkelden een theoretisch model op basis van energieminimalisatie, dat goed overeenkomt met de experimenteel gemeten buigkracht en golflengte. Voortbouwend op inzichten uit de modelsystemen en rekening houdend met van der Waals interacties tussen overlappende 2D-nanosheets, stelden we een theoretisch model voor om de knikgolflengten te verklaren die in monolagen van nanosheets worden waargenomen.

Bij sproeidrogen leidt de verdamping van waterdruppels die deeltjes bevatten tot de vorming van geknikte capsules. Eerdere studies naar sferische colloï-

den hebben aangetoond dat verdamping leidt tot accumulatie van deeltjes aan het lucht-watergrensvlak. Deze geaccumuleerde deeltjeslaag (schil) knikt onder verdere compressie wanneer de verdamping voortschrijdt. De volgende vragen blijven echter onbeantwoord: (1) hoe de adsorptie van deeltjes aan het grensvlak de verdampingssnelheid beïnvloedt, (2) welk criterium het begin van een knik bepaalt, (3) hoe dit criterium afhangt van de adsorptie van deeltjes aan het grensvlak, en (4) hoe de verdampingssnelheid de uiteindelijke geknikte morfologie beïnvloedt. Om deze vragen te beantwoorden, bestudeerden wij de verdamping van een enkele waterdruppel die grafeenoxide-nanosheets bevat, gedeponeerd op superhydrofobe substraten.
We ontdekten dat de adsorptie van deeltjes aan het grensvlak een verwaarloosbaar effect had op de verdampingssnelheid van druppels. We verklaren dit door het aanpassen van bestaande wiskundige modellen voor een analoog elektrostatisch probleem. Het model voorspelt dat wanneer de deeltjes uniform over het grensvlak verdeeld zijn en veel kleiner zijn dan de druppel, de verdampingssnelheid identiek is aan die van een zuivere waterdruppel. Het begin van de knik hangt daarentegen sterk af van de adsorptie van deeltjes aan het grensvlak. Om deze afhankelijkheid te verklaren, modelleerden we de schil als een deeltjes-dubbellaag. De dubbellaag knikt wanneer de totale grensvlakspanning negatief wordt, wat met de experimenten overeenkomt. Ten slotte nam de knikgolflengte van de gedroogde capsule af met toenemende verdampingssnelheid. Voor een vaste fractie leidt snellere verdamping tot dunnere schillen. In dunne schillen bevordert de lage buigingsenergie in vergelijking met de rek-energie hoge kromming deformaties, wat kortere knikgolflengtes oplevert.
Concluderend verdiept dit proefschrift het fundamentele begrip van de knik van grensvlakken beladen met plaatachtige deeltjes. De verkregen resultaten bieden praktische manieren om de microstructuur te beheersen van industrieel geproduceerde 3D-materialen gemaakt van 2D-nanosheets.

Translated by Jip Zant and Marko Draskic

சுருக்கம்

(Summary in Tamil)

2டி நானோமெட்டீரியல்கள் என்பது மிக மெலிந்த தாள் போன்ற பொருட்கள். ஒரு தாளின் நீளம் சுமார் 1 மைக்ரான் மற்றும் தடிமன் வெறும் 1 நானோமீட்டர் மட்டுமே இருக்கும். இதை எளிதாக புரிந்து கொள்ள, மனிதன் தலைமுடியின் தடிமன் சுமார் 80,000–100,000 நானோமீட்டர்; அதாவது ஒரு முடியின் தடிமனுக்கு இணையாக 80,000 நானோ தாள்கள் அடுக்கி வைக்கலாம். 2டி நானோமெட்டீரியல்கள் மாசு இல்லா ஆற்றல் கருவிகளை உருவாக்குவதில் முக்கிய பங்கு வகிக்கின்றன. ஆனால், இந்த 2டி தாள்களை கொண்டு 3டி வடிவங்களை உருவாக்குவது ஒரு பெரிய சவாலாக உள்ளது, ஏனெனில் அவற்றின் நுண்ணமைப்பு மிகவும் நுட்பமாக கட்டுப்படுத்தப்பட வேண்டும்.

நுண்ணமைப்பை துல்லியமாக கட்டுப்படுத்த இந்த ஆய்வில் இரண்டு முயற்சிகள் மேற்கொள்ளப்பட்டன:
1. Langmuir-Blodgett assembly: நீர்-காற்று சந்திக்கும் இடத்தில் தாள்களை சீரமைத்து அடுக்குவது.
2. Spray drying: நானோ தாள்களுடன் கூடிய தண்ணீர் துளிகளை உலர்த்தி துகள்கள் உருவாக்குவது.

இரண்டிலும், தாள்கள் அழுத்தப்பட்டால் அவை “மடங்குதல்” (buckling) என்ற நிலையை அடைகின்றன. இதனால் அலைபோன்ற சுருக்கங்கள் (wrinkles) உருவாகின்றன. இந்த சுருக்கங்களை கட்டுப்படுத்துவதன் மூலம் 3டி வடிவங்களை வடிவமைக்க முடியும்.

முதலில், பெரிய பிளாஸ்டிக் தாள்களை மாதிரி பொருட்களாகக் கொண்டு, நீர்-எண்ணெய் அல்லது நீர்-காற்று சந்திக்கும் இடத்-

தில் வைத்து, அவை எவ்வாறு மடங்குகின்றன என்று கவனிக்-கப்பட்டது. இதனால், சுருக்கங்கள் எவ்வளவு இடைவெளியில் உருவாகின்றன என்பதை அளவிட முடிந்தது. இந்த அளவீட்டி-னை அடிப்படையாகக் கொண்டு ஒரு கணித மாதிரி உருவாக்-கப்பட்டது.

இந்த எளிய முயற்சிக்கு பிறகு, நானோ தாள்கள் துளிகளாக உல-ரும்போது அவை எப்படி மடங்குகின்றன என்பதை ஆராய்ச்சி செய்தோம். நானோ தாள்கள் கொண்ட தண்ணீர் துளிகளை உலர்த்-தும் போது, நீர்-காற்று சந்திக்கும் இடத்தில் ஒரு துகள்-அடுக்கு உருவாகிறது. இந்த அடுக்கு அழுத்தப்பட்டால், அது மடங்குகி-றது. ஆனால், இது எந்த நிலையில் மடங்கும் என்பதை புரிந்து-கொள்ள இரண்டு முயற்சிகள் செய்யப்பட்டன: கண்ணாடி கு-ழாயில் நானோத் துகள்கள் கலந்த தண்ணீர் ஆவியாகும் சோ-தனை மற்றும் ஒற்றைத் துளி ஆவியாகும் சோதனை.

இந்தச் சோதனைகளில் இருந்து இரண்டு புதிய முடிவுகளை கண்-டுபிடித்தோம். முதலாவது, நானோ தாள்கள் நீர்-காற்று சந்திக்-கும் இடத்தில் ஒட்டினாலும், ஆவியாகும் மொத்த வேகம் எந்த வி-தத்திலும் மாறவில்லை. இரண்டாவது, மடங்கல் எப்போது ஆரம்-பிக்கிறது என்பது, தாள்கள் நீர்-காற்று சந்திக்கும் இடத்தில் ஒட்-டியுள்ளதா இல்லையா என்பதையே சார்ந்திருந்தது. மூன்றாவ-து, துளி எவ்வளவு வேகமாக ஆவியாகிறது என்பதுதான், இறு-தியாக உலர்ந்த பிறகு உருவாகும் சுருக்கங்களின் இடைவெளி-யை நிர்ணயிக்கிறது. வேகமாக ஆவியாகும் துளிகள் நுண்ணிய சுருக்கங்களை உருவாக்குகின்றன; மெதுவாக ஆவியாகும் து-ளிகள் பெரிய இடைவெளியுள்ள சுருக்கங்களை உருவாக்குகின்-றன. இது, thin elastic shells என்ற கோட்பாட்டால் விளக்கப்பட-லாம்.

இந்த ஆய்வு, 2டி நானோத் தாள்களிலிருந்து உருவாக்கப்படும் 3டி பொருட்களின் நுண்ணமைப்பை கட்டுப்படுத்துவது தொ-டர்பான அடிப்படை அறிவை வழங்குகிறது. மேலும், பரிசோ-தனைகள், கோட்பாட்டு மாதிரிகள், மற்றும் கணினி சோதனை-கள் இணைந்து, நானோத் தாள் அடிப்படையிலான கருவிகளின் உற்பத்தி மற்றும் மேம்பாட்டுக்கு முக்கிய பங்களிப்பு வழங்கக்-கூடும்.

Chapter 1

Introduction

The thesis begins with the motivation to study fluid interfaces populated with plate-like particles. The motivation is understanding the process governing the fabrication of 3D structures from 2D nanosheets via Langmuir-Blodgett technique and spray drying. Despite the widespread use of these processes, the behavior of nanosheets adsorbed at fluid interfaces subjected to interface compression remains poorly understood. Addressing this research gap requires fundamental research into the mechanics of nanosheets at flat or curved fluid interfaces. A major challenge in understanding interfacial processes involving 2D nanomaterials is the poor control of experimental conditions in most published work. This challenge highlights the need to develop model experimental systems.

1.1 Motivation

2D nanomaterials, such as graphene and graphene oxide, are plate-like particles with lateral size of a few microns and a thickness of the order of nanometers (see Fig. 1.1). The 2D geometry and physico-chemical properties of these materials yields extraordinary optical, electrical, thermal, mechanical, and catalytic properties [1, 2]. The combination of these extraordinary properties has enabled the development of advanced materials, including electrodes and catalysts, for the energy transition [3–11].

Assembly of 2D nanomaterials by capillary forces remains one of the most important techniques for controlling the morphology of the 3D materials formed from 2D particles. In this dissertation, we are motivated by two such techniques: the Langmuir-Blodgett technique and the spray drying technique, both of which are widely adopted in academia and industrial settings [12, 13]. These processes involve assembling 2D nanosheets at either flat or curved fluid interfaces, with the Langmuir trough used for flat interfaces and spray drying for curved interfaces, as detailed in Sections 1.3 and 1.4. The fluid interface is then compressed, causing the layer formed by many nanosheets to undergo buckling. To better understand the buckling behavior, it is essential to study how multiple nanosheets adsorbed at fluid interfaces or interacting with fluid interfaces respond to mechanical compression. While the response of assemblies of spherical particles at fluid interfaces has been extensively studied [14–17], the interfacial compression mechanics of layers of non-spherical particles, particularly plate-like particles, remain poorly understood.

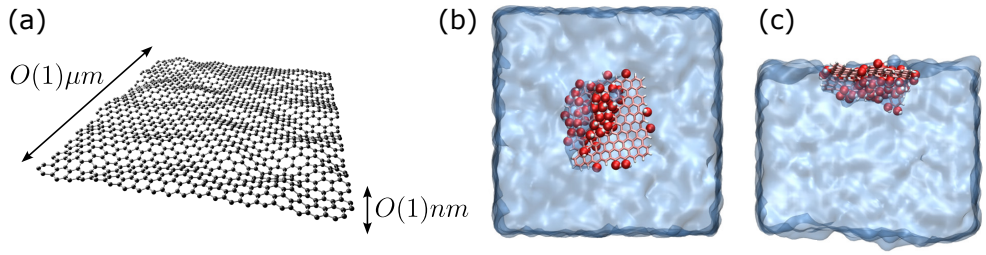

Figure 1.1: (a) Schematic of a single layer graphene sheet illustrating its characteristic dimensions. Subfigures (b) and (c) show single layer graphene oxide sheet adsorbed at an air-water interface, viewed from the top and side view, respectively. The red spheres on the sheet surface illustrate oxygen functional groups. Images adapted from [18].

2D nanomaterials are typically produced by shear exfoliation of layered materials in liquids [19, 20]. This process yields nanosheets with nanometric thickness and micrometric lateral dimensions, resulting in very high aspect ratios, of the order of 1000. Graphene, obtained by exfoliating graphite, consists of a single layer of carbon atoms arranged in a hexagonal lattice. It is not water-soluble and can be dispersed in solvents like N-Methyl-2-pyrrolidone (NMP) and Dimethylformamide (DMF), which are known to be toxic. In contrast, graphene oxide (GO) is a chemically modified derivative of graphene. GO has a similar geometry but contains oxygen groups on its surface, illustrated by red spheres in Fig. 1.1 b and c. These oxygen groups form hydrogen bonds with water molecules which makes GO dispersible in water [21, 22]. Changing the pH of the suspension modifies these hydrogen bonds leading to pH-dependent adsorption of GO at the air-water interface. At low pH, GO becomes less hydrophilic and adsorbs at the air-water interface as shown in Fig. 1.1 b [18, 23].

1.2 Buckling of slender structures

Buckling of monolayers at a fluid-fluid interface in Langmuir troughs and crumpling of spray dried capsules are mechanical instabilities. The buckling instability of thin structures is illustrated by analyzing a thin elastic sheet subject to uniaxial compression. Consider an elastic sheet of length L, width w and thickness t subjected to a uniaxial compressive displacement δ. The sheet can deform either by changing its length to $L - \delta$ or by undergoing an out of plane deformation with constant length. For a linear elastic material, the total elastic energy is

$$\mathcal{E}_e = \frac{1}{2} \iint dxdy \int_{-h/2}^{h/2} \sigma\epsilon \; dz \tag{1.1}$$

where σ and ϵ are the stress and strain, respectively. Hooke's law states $\sigma = E\epsilon$, where E is the elastic modulus. Substituting Hooke's law in Eqn. 1.1 gives the total elastic energy as a function of strain. For a slender beam ($L \gg t$) the strain is $\epsilon = \epsilon_0 + \epsilon_b$, where ϵ_0 is the middle surface strain and ϵ_b is the bending strain. The middle surface lies at $z = 0$, with $z \in (-t/2, t/2)$ and ϵ_0 is the change in length of the middle surface. The bending strain is $\epsilon_b \sim z/R$, where $1/R$ is the local curvature of the beam. Substituting ϵ_0 and

ϵ_b in Eqn. 1.1, we obtain

$$\mathcal{E}_e \sim \underbrace{Et \iint dxdy\ (\epsilon_0)^2}_{\text{Stretching}} \ + \ \underbrace{Et^3 \iint dxdy\ (1/R)^2}_{\text{Bending}}. \tag{1.2}$$

The shape of the deformed elastic sheet is determined by the configuration that minimizes the total elastic energy. The prefactors to the stretching and bending energies are of the order Et and Et^3, respectively. For thin sheets, the energy of bending deformations is much smaller than the energy required for stretching. Thus, the total energy is minimized by infinitely small stretching and finite bending deformations [24]. This prediction is appreciated when we realize that it is easier to bend a sheet of paper than to stretch it.
We apply the principle of total energy minimization in Chapters 2 and 3 to predict the buckled shapes of particle monolayers and multilayers, respectively. Conversely, the observed buckling patterns reveal the dominant energy contributions at play.

1.3 Langmuir-Blodgett technique

The Langmuir trough is a device used to study the interfacial rheology of complex fluid interfaces [25–28]. Figure 1.2 shows a schematic of a Langmuir trough with 2D nanosheets trapped at an air-liquid interface. The Langmuir trough has two movable barriers at the open end of the trough. A liquid, usually water or oil, can be added to the trough such that the air-liquid interface coincides with the open end of the trough. A particle monolayer is prepared by spreading the particles by using a volatile liquid, for example hexane. The volatile liquid evaporates leaving a monolayer of particles trapped at the air-liquid interface. By varying the distance between the barriers, the surface concentration of the particles can be controlled.
The particle monolayer is subjected to uniaxial compression by decreasing the distance between the barriers. The compression results in particle-particle repulsive forces that translates to a surface pressure Π opposing the surface tension γ. The effective interfacial tension $\gamma_{eff} = \gamma - \Pi$ can be measured by a Wilhelmy plate [16]. Compression of the monolayer beyond the jamming point results in $\gamma_{eff} \simeq 0$ and interface buckling [28].
Recently, Langmuir troughs have been used to produce films of 2D nanosheets at industrial scale [12, 29, 30]. Layer-by-layer assembly of buckled monolayers of nanosheets has been leveraged to fabricate corrugated films with superior

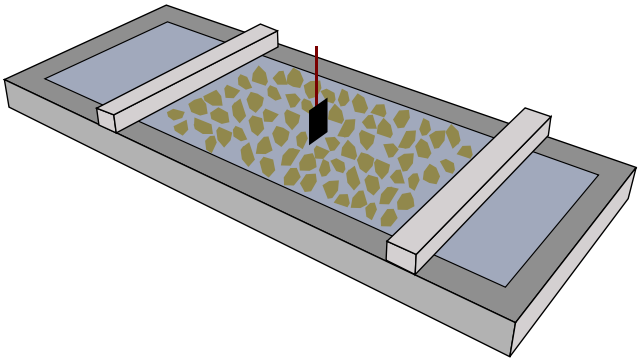

Figure 1.2: Schematic of a Langmuir trough with a monolayer of 2D nanosheets. The black plate illustrates a Wilhelmy plate that measures the surface pressure.

electrical properties [31]. Further, by tuning compression and nanosheet lateral size, the properties of the layer-by-layer assembly such as porosity, pore size, and conductivity can be precisely controlled. To engineer such corrugated films, the macroscopic response, such as the buckling wavelength, of the monolayer must be known as a function of the particle size. Previous studies have only characterized qualitative macroscopic response of the monolayers of nanosheets [25, 26, 31]. Mathematical models predicting the macroscopic buckling wavelength are not available.

Understanding the buckling of monolayers of spherical particles at fluid interfaces provides a basis for studies on plate-like particles. A monolayer made of spherical particles at a fluid interface has been shown to buckle similar to a thin elastic sheet (see Fig. 1.3) [14]. The equation governing the shape of a thin elastic sheet is

$$B\frac{d^4h}{dx^4} + T\frac{d^2h}{dx^2} + \rho g h = 0, \tag{1.3}$$

where B is the effective bending rigidity of the interface, h is the out of plane deformation, T is the compressive force per unit length, ρ is the density of the heavy fluid, g is the gravitational acceleration and x is the direction of compression. Eqn. 1.3 is obtained by minimizing the total energy associated with deforming the elastic sheet. The total energy comprises the elastic energy of the sheet and the gravitational energy of the liquid beneath the sheet. Assuming a sinusoid for the interface shape, the characteristic buckling wave-

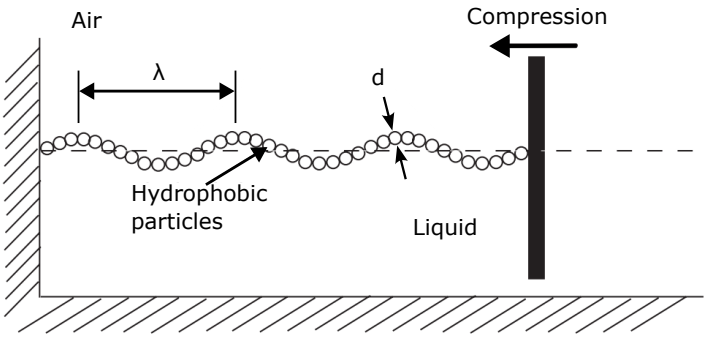

Figure 1.3: Schematic of a monolayer of spherical particles undergoing buckling instability due to uniaxial compression. Figure adapted from [14].

length is $\lambda \sim (B/(\rho g))^{1/4}$. Vella et al. [14] assumed that a bending rigidity of the form $B \propto \gamma d^2$, where d is the diameter of the spherical particles, obtaining a wavelength prediction $\lambda \sim (\gamma d^2/(\rho g))^{1/4}$. This result agreed well with experimentally measured buckling wavelength.

In an attempt to explain the stability of emulsions stabilized by particles, Kralchevsky et al. [32] proposed a physical reason for the $B \propto \gamma d^2$ dependence. Emulsions can destabilize by coalescence of drops stabilized by particles embedded in the fluid-fluid interface. Prior to coalescence, the spherical interface must bend from its equilibrium shape. A particle free interface has no resistance to bending [33], however, this is no longer the case if the interface is populated with particles.

The dependence is understood by analyzing, for example, an air-water interface with adsorbed spherical particle subject to a bending deformation. Figure 1.4 shows the equilibrium shape of an interface of radius R with an adsorbed spherical particle of diameter d. It is assumed that the particle diameter is much smaller than the interface radius ($d \ll R$). The interface undergoes a small change in radius δR as a result of bending. The total interfacial energy is $E = \gamma_{wa}A_{wa} + \gamma_{sw}A_{sw} + \gamma_{sa}A_{sa}$, where A_{aw}, A_{sw} and A_{sa} are the areas of the air-water, solid-water and solid-air interface, respectively and γ_{aw}, γ_{sw} and γ_{sa} are the interfacial energies (per unit area) of the air-water, solid-water and solid-air interface, respectively. As the interface curvature changes, the particle protrudes out of the interface in order to satisfy the Young angle at the contact line. The motion of the contact line leads to a change in interfacial

energy per unit area given by $(\delta E/A) \propto \gamma_{aw} d^2/R^2$. The bending rigidity of the interface is defined as $B = \frac{1}{\kappa}\frac{\partial(\delta E/A)}{\partial \kappa}$, where $\kappa = 1/R$ is the interfacial curvature. Using this relation, the bending rigidity of a fluid interface laden with spherical particles is found to be proportional to $\gamma_{aw} d^2$.

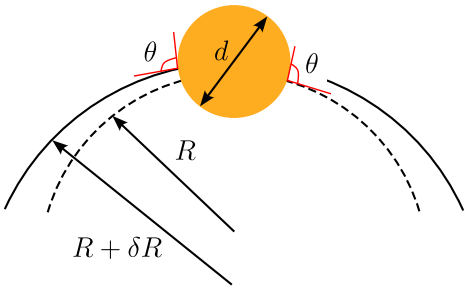

Figure 1.4: Schematic showing the equilibrium position of an adsorbed spherical particle at an air-water interface. When the curvature of the air-water interface changes, the adsorbed particle shifts its position to preserve a constant Young angle θ.

The bending rigidity of a particle monolayer is thus closely linked to the contact line motion. Therefore, the analysis of monolayers of plate-like particles must account for the change in contact line shape corresponding to the rearrangement of the particles upon bending of the fluid interface. Previous studies on plate-like particles trapped at fluid interfaces suggest a pinning of the contact lines at the edges of the particles [34–36] or presence of small undulations in the contact line at the particle edges [37]. Figure 1.5 shows two possible contact line configurations in plate-like particles at fluid interfaces. In both cases, the contact line undulation amplitude is of the order of particle thickness. This suggests the any contact line motion resulting from interface bending is limited to the particle thickness.

1.4 Spray drying

Spray drying is the industrial process of producing dry powders from liquid dispersions. Figure 1.6 shows a schematic of an industrial spray dryer. The dispersion is atomized by a spray nozzle into fine drops which undergo evaporation in a chamber in which hot gas is flowing. The dried powders are then

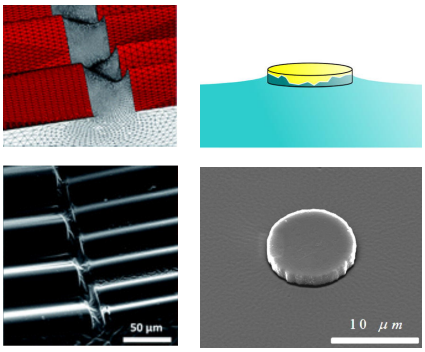

Figure 1.5: Top panel shows different configurations of contact lines observed for plate-like particles. The bottom panel shows the corresponding SEM images of the contact line adapted from [36, 37].

collected in a cyclone centrifuge. Spray dryers are widely used in the pharmaceutical [38] and food industries [39] and in the fabrication of functional materials [40–44].

Spray drying has also been employed to produce crumpled capsules from suspensions of 2D nanosheets [45]. Crumpling has several advantages: the presence of sharp corners om the surface of a crumpled capsule reduces restacking of the 2D nanosheets [46]. The crumpled capsules remain stable when redispersed in water and do not unfold [45, 47]. Crumpled graphene, produced by spray drying [45], has found application as lubricant additives [5] and as electrode materials [3, 4, 10].

Most studies on the formation of crumpled capsules have focused on single nanosheets confined within shrinking droplets [46, 48–53]. However, practical applications typically involve droplets containing many nanosheets [45, 48]. Given the lack of information for nanosheets, we review a few studies on droplet evaporation containing multiple spherical particles in the following.

During the evaporation of drops containing multiple spherical particles, the interface retracts and capillary forces confine the particles within the droplet. The confinement may result in different particle arrangements in the dried capsule as shown in Fig. 1.7. For applications to optics, a uniform arrangement as seen in Fig. 1.7 a is desired [40]. For many applications involving nanosheets, buckled capsules are desired, similar to the capsule in Fig. 1.7 d. Figure 1.7 b and c show spray dried capsules of bidispersed particle sus-

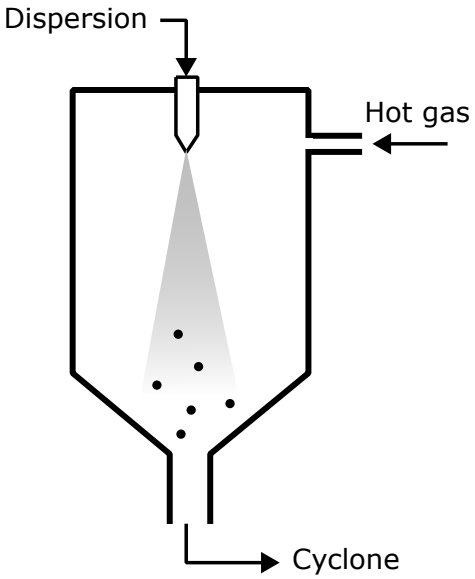

Figure 1.6: Schematic of a spray dryer in operation. The dried powders are illustrated as black circles.

pensions at different conditions. A key area of interest in spray drying is the control of capsule morphology, as the morphology significantly influences functionality.

The particle distribution in an evaporating drop is understood by considering the Péclet number, defined as the ratio of the Brownian diffusion time scale to the fluid convection time scale [58]. The diffusion time is given by L^2/D_p, where L is the characteristic length scale of diffusion and D_p is the translational diffusion coefficient of the particle. The fluid convection time scale is L/v, where v is the fluid velocity. When the drying of the drop is slow compared to the Brownian motion $Pe \ll 1$, a dense spherical aggregate forms [59]. Fast evaporation $Pe \gg 1$, leads to the formation of a dense layer of particles near the interface [60, 61]. This layer can undergo buckling.

Tsapis et al. [60] proposed that buckling of the shell layer of spherical particles occurs when particles are forced into contact overcoming electrostatic repulsion. The particles adhere to each other due to attractive van der Waals forces. At this point, the shell layer becomes a solid that immediately buckles.

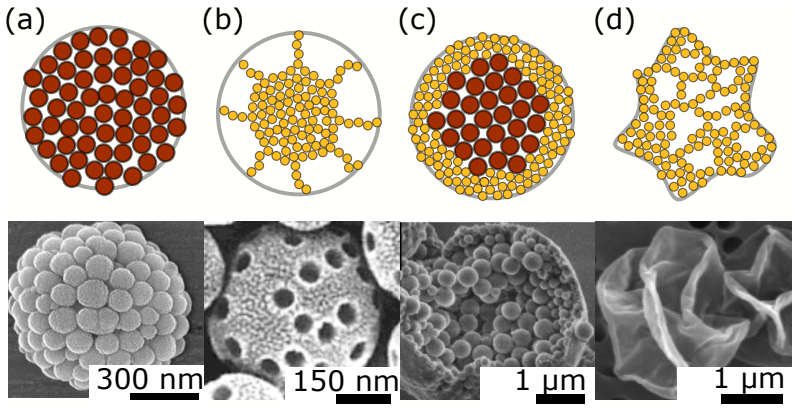

Figure 1.7: Top panel shows the schematic of different capsule morphologies obtained from spray drying. The bottom panel shows corresponding SEM images adapted from [54–57]

Milani et al. [62] showed that buckling can occur without colloidal destabilization. At a high solid fraction of spherical particles in the shell layer, the repulsive colloidal particles form a glassy state. Buckling occurs when the deformation due to the retraction of the interface is faster than the microscopic rearrangement of the particles in the glassy shell layer.
Archer et al. [61] showed that there is a strong correlation between the buckled shape and the evaporation rate. However, the physical reason for such dependence remains unclear. Moreover, the role of particle adsorption at the interface and its influence on the onset of buckling has not been investigated.

1.5 Research objectives

A few theoretical models of the mechanical response of monolayers of spherical particles to compression are available in the literature (see Eqn. 1.3). These models have advanced our understanding of the mechanics of fluid interfaces embedded with a monolayer of spherical particles and have enabled engineering applications [63–65]. In contrast, we have seen that the mechanics of monolayers of plate-like particles is not understood.
Previous studies used Langmuir-Blodgett technique to probe the mechanics of monolayers of nanosheets at fluid interfaces [25, 26, 66]. The nanoscopic thickness of the sheets limits optical accessibility making it difficult to ob-

serve how individual sheets interact and modify the shape of the interface. Moreover, nanosheet polydispersity obscures the relationship between monolayer mechanics and sheet size. Therefore, well controlled experiments using optically accessible monodisperse particles are essential to advance our understanding of the mechanics of monolayers of plate-like particles at fluid interfaces. The experimental results can be used to formulate mathematical models.

In the context of spray drying, the mechanism responsible for formation of crumpled capsules following evaporation of drops filled with nanosheets is poorly understood. Previous studies have primarily used lab scale spray dryers, where the process parameters such as drying rate and drop size are not well controlled and the evaporation process cannot be visualized. It is not possible to identify the mechanism responsible for the crumpling only by studying the final shape of the dried capsules resulting from uncontrolled experiments. To address this challenge, controlled experiments that enable real-time observation of the shape evolution of individual evaporating drops are essential.

Studies on the evaporation of drops with spherical particles suggest that a dense layer of particles forms at the air-water interface and eventually undergoes buckling. In the case of evaporation of drops with nanosheets, we also expect the accumulation of a multilayer of nanosheets near the fluid interface. The specific objectives of this thesis are:

- To develop model experimental systems to understand the buckling mechanics of monolayers of nanosheets at fluid interfaces.
- To develop mathematical models to predict the onset of buckling and the buckling wavelength following uniaxial compression.
- To develop controlled evaporation experiments to observe the shape evolution of evaporating water drops containing 2D nanosheets, using graphene oxide as model 2D nanomaterial.
- To investigate the formation of a multilayer of nanosheets near the air-water interface during drop evaporation, with the aim of understanding the morphology of crumpled nanosheet capsules produced by spray drying.

The overall objective of this dissertation is to investigate the buckling of fluid interfaces with monolayers and multilayers of plate-like particles through model experiments and to develop theoretical and numerical models that explain the observed phenomena

1.6 Thesis outline

Chapter 2 focuses on the uniaxial compression of fluid-fluid interface laden with a monolayer of millimetric plate-like particles. The resulting buckling patterns are analyzed using optical measurements. Mathematical models are developed to explain the buckling wavelengths and forces. Building on the understanding of buckling of monolayers, Chapter 3 investigates the buckling of curved fluid interface populated with multilayer of graphene oxide nanosheets. Experiments are conducted with single evaporating drops sitting on a superhydrophobic substrate. Key process parameters such as solid concentration, pH and evaporation rate are systematically varied to examine their influence on the final morphology. Finally, Chapter 4 summarizes the key conclusions drawn from the experimental studies and mathematical analysis. The chapter also discusses recommendations and outlines potential directions for future research.

Chapter 2

Buckling of a monolayer of plate-like particles trapped at a fluid-fluid interface

Particles trapped at a fluid-fluid interface by capillary forces can form a monolayer that jams and buckles when subject to uni-axial compression. Here we investigate experimentally the buckling mechanics of monolayers of millimeter-sized rigid plates trapped at a planar fluid-fluid interface subject to uni-axial compression in a Langmuir trough. We quantified the buckling wavelength and the associated force on the trough barriers as a function of the degree of compression. To explain the observed buckling wavelength and forces in the two-dimensional monolayer, we consider a simplified system composed of a linear chain of plate-like particles. The chain system enables us to build a theoretical model which is then compared to the two-dimensional monolayer data. Both the experiments and analytical model show that the wavelength of buckling of a monolayer of plate-like particles is of the order of the particle size, a different scaling from the one usually reported for monolayers of spheres. A simple model of buckling surface pressure is also proposed, and an analysis of the effect of the bending rigidity resulting from a small overlap between nanosheet particles is presented. These results can be applied to the modeling of the interfacial rheology and buckling dynamics of interfacial layers of 2D nanomaterials.

Related publication: **Suriya Prakash**, Hugo Perrin and Lorenzo Botto, *Buckling of a monolayer of plate-like particles trapped at a fluid-fluid interface.* PRE (2024).

2.1 Introduction

The buckling wavelength of monolayers of nearly spherical particles trapped at a fluid interface under compression has been studied with both realistic particles (Lycopodium, Chemigum) [14] as well as model particles (glass beads, zirconium oxide beads) [17]. In these experiments, the particles were spread at an air-water interface and the particle layer subject to uni-axial compression in a Langmuir trough. Both the buckling wavelength and the force on the barrier, proportional to the surface pressure [68], were measured. A mathematical model that treats the monolayer as a continuous elastic sheet captured the buckling wavelength measured in these experiments. The relation between the effective mechanical properties of the monolayer and the particle size was obtained by assuming an effective Young modulus $E \sim \gamma/d$, where γ is the surface tension of the bare fluid/fluid interface and d is the nominal sphere diameter [14]. According to this model, and in agreement with experimental results [14, 15, 17], the buckling wavelength of the monolayer scales as $\sim \sqrt{\ell_c d}$, where $\ell_c = \sqrt{\gamma/(\tilde{\rho} g)}$ is the capillary length, $\tilde{\rho}$ is the density difference between the two fluids across the interface and g is the acceleration of gravity.

Compression experiments on buckling of interfacial monolayers of graphene oxide show a buckling wavelength in the range of 4 - 20 particle diameters, with an average wavelength of 7.6 particle diameters [26]. The theory developed for spheres would give approximately 250 particle diameters, largely overestimating the observed wavelength. Given the large aspect ratio of graphene oxide sheets, applying models for spheres is questionable and developing mathematical models specifically tailored to plate-like particles is thus necessary. Deriving such models starting from experimental data obtained with nanoparticles, which is affected by uncontrolled variables such as polydispersity in size [69] and possibility of particle-particle overlap [66] is challenging. With a model experimental system, in which macroscopic particles of controlled shapes are used, one can investigate the associated interfacial mechanics without the complications of an actual nanoparticle system.

In this paper, we study experimentally the uni-axial compression of a monolayer of millimeter-sized plate-like particles trapped at a fluid-fluid interface by capillary forces. We start with observations of a two-dimensional monolayer of hexagonal particles at an air-water interface. We then consider a linear chain of square plates (1D system). We develop a theory to explain the linear chain system which is then applied to the two-dimensional (2D) particle monolayer. In our experiments, the particles are not overlapping for most of the

monolayer deformation. However, we use the one-dimensional mathematical model to discuss possible implications of small overlaps between the particles in terms of an increased effective bending rigidity of the particle layer.
In our experiments, the Bond number based on the weight of the particles is small [70], so the downward distortion of the fluid interface owing to the weight of the particle (minus buoyancy) is relatively unimportant. However, as we will see, when in contact the particles can displace fluid by rotating around an axis parallel to the fluid interface. This results in a gravitational contribution to the interfacial mechanics. In the linear chain case, we are able to investigate the regime in which capillary forces are dominant over gravitational forces by density matching of the upper and lower fluids.
The motivation for the current work is to better understand the compression of 2D nanomaterials at fluid-fluid interfaces. Two-dimensional nanomaterials, of which the most discussed are graphene and graphene oxide, can take the form of a colloidal dispersion of nanometrically thin plate-like particles of large aspect ratios [20,71]. Recently, the use of fluid interfaces has emerged as a way to control the assembly of these systems [72, 73]. In the Langmuir-Blodgett technique, for example, a monolayer of 2D nanomaterials is adsorbed at a flat fluid-fluid interface, and the monolayer compressed by barriers [25]. The monolayer is then transferred to a solid substrate [12, 74]. Critical to the performance of the resulting particle coating is predicting the particle coverage in the fluid interface upon uni-axial compression in the trough, and whether the particle monolayer displays a solid-like behavior. If the particles jam at the fluid interface, the particle monolayer can buckle and the signature of this buckling is visible in the profile of surface pressure vs. barrier displacement [17,31,66,75]. The analysis of the relation between buckling wavelength and associated force on the barrier discussed in the current paper is therefore relevant for interpreting interfacial rheology measurements with 2D nanomaterials. More broadly, the current investigation could help understanding the mechanics of particle rafts, armored bubbles or droplets, a research field that has received increasing attention recently from the soft matter physics, colloidal science and fluid mechanics communities [76].

2.2 Experimental methods

Uni-axial compression experiments are carried out in an in-house-made rectangular trough of length 200 mm and width $W_t = 50$ mm, see Fig. 2.1. A stationary barrier mounted on a force sensor allows us to measure the force F

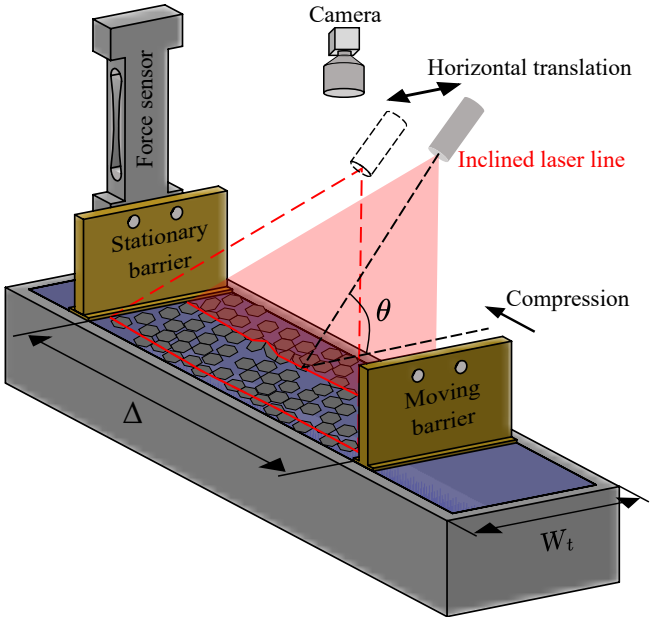

Figure 2.1: Schematic of the experimental setup to measure surface pressure and topology of the interfacial monolayer of plates.

on the barrier and the surface pressure $\Pi = F/W_t$. A moving barrier mounted on a linear stage allows us to control the distance Δ between the barriers in steps of 10 μm. To measure forces of the order of mN we used a load cell with a resolution of $\pm\,0.1$ mN. For small forces of the order of μN, produced by the smallest particles we considered, we used a cantilever-based force sensor, that is described later in detail.

For the 2D monolayer experiments, we used transparent hexagonal plates made of Mylar (density $\rho_p \simeq 1400\,\mathrm{kg/m^3}$) purchased from *Geotech International*. The plates have thickness $t = 50\,\mu$m and two different lateral sizes, $L = 1.5$ mm and 3 mm. Here L refers to the inscribed circle diameter of the hexagonal plates. To remove possible contaminants, we aspirate the fluid interface using a suction pipette after moving the barriers to minimum opening [77]. The process is repeated until the fluid interface is clean. The interface is assumed to be clean if the surface pressure at maximum compression is below 4 mN/m. The 2D monolayer is prepared by gently sprinkling the particles on the air/water interface at maximum $\Delta \simeq 3W_t$. Overlapping particles were separated by a stirring rod. The 2D monolayer is then compressed at a velocity of $200\,\mu$m/s. The monolayer undergoes out-of-plane deformations, whose amplitude A is measured by the inclined laser line method [78, 79]. The technique involves projecting a laser sheet at an angle θ with respect to the particle-laden fluid interface (Fig. 2.1). The intersection of the laser sheet with the monolayer results in a line that is imaged from the top by a camera. The intersecting line is straight for a flat monolayer and distorted for a deformed monolayer. The out-of-plane deformation amplitude can be calculated from the lateral distortion of the laser line, accounting for a proportionality constant $\tan(\theta)$. The angle $\theta \approx 28^\circ$ is the angle of inclination of the laser sheet, with respect to the air-water interface (see Fig. 2.1). After positioning the laser, this angle was measured precisely by measuring $\tan(\theta)$, the factor of conversion between in plane displacement of the laser line and out of plane deformation, for a rectangular block of known height (15 mm) placed on the fluid interface by using a microstage [78]. The resolution of the out-of-plane deformation is $60\,\mu$m. The novelty of our method is that we use a laser line that sweeps the monolayer which provides a continuous topographic map, instead of the height profile along a single line. To do so, the laser source is mounted on a linear stage controlled by a stepper motor.

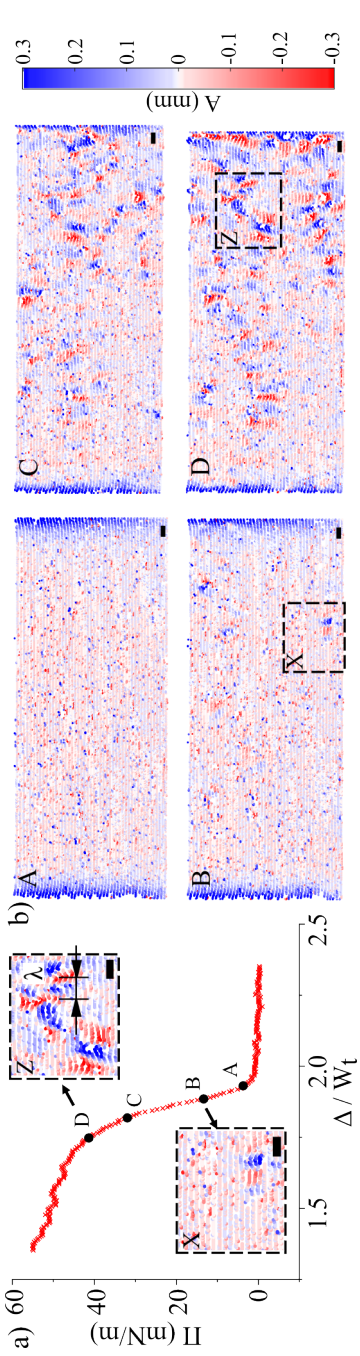

Figure 2.2: a) Surface pressure Π versus normalized separation distance Δ/W_t between the barriers for uni-axial compression of $N \simeq 1590$ hexagonal plates of lateral size 1.5mm trapped at a water/air interface. We identified four characteristic points A, B, C, and D in correspondence to which the topology of the particle-laden interface is measured. The insets show zoomed-in micro-structures highlighting key features of topology in points B and D. The same data normalized by Δ_0 in shown in Appendix 2.5, where Δ_0 is the compression distance at which the surface pressure becomes finite. b) Surface topology map of the entire trough area corresponding to the characteristic points in Fig. 2 a. The blue color at the left and right ends of the topology maps corresponds to the curved menisci near the barriers. The scale bar shown as a black line is 3 mm, i.e. 2 particle diameters.

For the single chain experiments, we used square-shaped Mylar plates of lateral sizes $L = 1$, 3, 5, 7, 10, 15, & 20 mm and thickness $t = 125$ μm, except for the 1 mm Mylar plates for which the thickness is $t = 23$ μm. For all the particles the aspect ratio L/t is larger than 23. The smallest plates are manufactured by laser cutting (*Optec Laser Systems*). Using the length and thickness of the plates and Young's modulus $\simeq 3$ GPa of Mylar, we estimate an Euler buckling threshold for the plates of ≥ 240 mN. Therefore, the plates do not buckle under compression forces of the order of a few mN and are considered to be rigid in our experiments. Experiments are carried out with both a glycerol/air interface and a water/sunflower oil interface; corresponding density differences between the two fluids are $\tilde{\rho} = 1200 \pm 1 \mathrm{kg/m^3}$ and $80 \pm 1 \mathrm{kg/m^3}$, respectively, as measured by an Anton Paar density meter (DMA 5000). The surface tensions of the glycerol/air and water/sunflower interfaces are 65 ± 1mN/m and 26 ± 1mN/m, respectively, measured by the pendant drop method in a Dataphysics Goniometer (OCA 25).

For the water/oil interface, the particles are first arranged at an air/water interface and the oil is gently added. Care is taken to arrange the particles in a straight chain between the barriers. Upon compression, the chain undergoes out of the plane deformation. A camera captures the side view of the chain and from the images we extracted the average amplitude $\langle A \rangle$ of individual plates in the chain. As mentioned earlier, for forces of the order of mN the load cell is used. For forces of the order of few μN we used a cantilever force sensor similar to the micropipette force sensor described in Ref. [80]. The deflection ξ of the cantilever is measured from the side view by a calibrated camera with a zoom lens. The force is computed from $F = k\ \xi$. The stiffness k of the cantilever was obtained by calibration; see Appendix 2.5 for the calibration procedure and calibration curves. We used cantilevers of stiffnesses $k = 29$ and 58 μN/mm. The resolution of the force F is $\sim 1\,\mu$N. This value is set by the resolution of the camera ($\simeq 11 \mu$m/pixel) and the stiffness of the cantilever.

2.3 Results

2.3.1 Observations on the 2D monolayers

Figure 2.2 (a) shows a typical evolution of the surface pressure $\Pi = F/W_t$ for decreasing values of the normalized distance Δ/W_t between the barriers. Fig. 2.2 (b) shows amplitude maps corresponding to 4 characteristic points of the $\Pi\, vs.\, \Delta$ curve, denoted A, B, C and D. For $\Delta/W_t > 2$ the plates are not

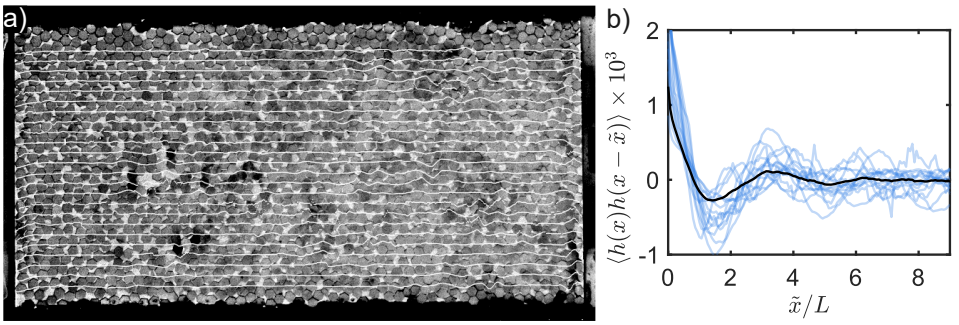

Figure 2.3: a) Tracked laser lines overlaid on the image of plate particle monolayer corresponding to the point D of Fig. 2.2 a. The vertical spacing between the lines is approximately one particle diameter. b) Height-height correlation functions based on the amplitudes from the tracked laser lines (in blue). The black line is the average over all tracked lines. Here the coordinates x and $\tilde{x}$ are along the compression direction.

touching each other and $\Pi \simeq 0$, as expected. As Δ/W_t decreases, contacts between the particles are established and a non-zero value of Π is measured. In correspondence to point A, $\Pi > 0$ because of the formation of force chains, but the interface remains flat (see panel A in Fig. 2.2). Buckling of the monolayer becomes measurable in correspondence to the point B. Buckling is evident from the change in amplitude of the particle-laden interface (inset X of Fig. 2.2 (a) and inset X in panel B of Fig. 2.2 (b)). Further compression leads to an increase in the number of buckled regions as the surface pressure rises. The characteristic point C belongs to this region of behavior. Buckling is predominantly present near the moving barrier (on the right in panel C of Fig. 2.2 b). The point D which we define as the "collapse point" is the value of Δ for which the experimental images start showing the local formation of multilayers. From A to D, the surface pressure increases relatively steeply, while for values Δ/W_t smaller than the one corresponding to D the surface pressure increases comparatively mildly. A video corresponding to the data of Fig. 2.2 is given in the Supplementary Information.

Figure 2.3 (a) shows the tracked laser lines overlaid on a top view of the 2D monolayer. The compression displacement for this figure corresponds to the "collapse point". To measure the local periodicity of the buckled zones (see inset Z of panel D in Fig. 2.2), we calculated the height-height correlation function $\langle h(x)h(x+\tilde{x})\rangle$ of the out-of-plane deformations along the compres-

sion axis x (blue curves in Fig. 2.3 (b)). The height-height correlation averaged over all the laser lines (black curve in Fig. 2.3 b) shows a maximum at $\tilde{x} \approx 3.1L$, which provides evidence that $\lambda \sim L$ for the 1.5 mm plates. For the larger ($L = 3$ mm) plates we measured $\lambda = 2.25L$ for small compression displacement, again suggesting $\lambda \sim L$. The key observation from the height-height correlation function is that the local wavelength in the regions where buckling occurs is of the order of the particle diameter.
For small compression (panel B in Fig. 2.2 b) the deformations are localized in a single buckled region of approximate extent $\approx 2.4\ L$ in the compression direction. For large compression (panel D in Fig. 2.2 b) the height-height correlation indicates a characteristic correlation length of about 3.1 L. Thus the periodicity of the buckled zones is approximately independent of Δ. Also, the monolayer does not show long-range ordered wave-like patterns, as reported for spheres [17]. The fact that no wavelengths much larger than the particle size occur is compatible with a simple model of chain compression, which we now describe.

2.3.2 One-dimensional chain model and comparison with experiment

We now analyze the compression of a linear chain of $N = 16$ square plates of size $L = 10$ mm trapped at an air-glycerol interface. The measured force F and the normalized average amplitude $\langle A \rangle / L$ of the out-of-plane deformation are shown in Fig. 2.4 as a function of $\Delta/(NL)$. From this plot, two regimes can be identified. For $\Delta/(NL) > 1$, the distance between the barriers is larger than the total length of the chain. Therefore, $F = 0$ and $\langle A \rangle \simeq 0$ ("flat state"). For $\Delta/(NL) = 1$, the plates touch each other and F starts to increase. The measured average amplitude increases when $\Delta/(NL)$ is approximately equal to 0.9995. The fact that F can be nonzero while $\langle A \rangle \simeq 0$, a feature that was also observed in the 2D system, is due to small particle rearrangements before jamming. The "buckled state" for $\Delta/(NL) < 0.9995$ is characterized by a sharp increase in F followed by a plateau. In the rest of this paper, we will call the plateau value of F the buckling force, as it represents the magnitude of the force that would be required to buckle the monolayer in an experiment conducted at applied force.
The dependence of amplitude on the compression displacement in the buckled state is compared against a simple analytical prediction based on the assumption that the triangular wave is perfectly periodic (see Appendix 2.5). The model predicts the trend correctly, but overestimates the experimental data.

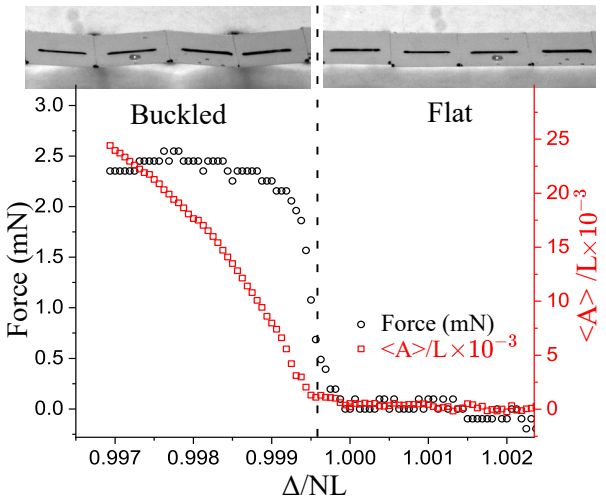

Figure 2.4: Single chain compression experiment. Force F (black markers) on the barrier and normalized average amplitude of out-of-plane deformation $\langle A \rangle / L$ (red markers) plotted against normalized distance $\Delta/(NL)$ between the barriers for $N = 16$ square plates of size $L = 10$ mm at a glycerol/air interface. The vertical dashed line at $\Delta/(NL) = 0.9995$ marks the transition from the flat to the buckled state. The two insets illustrate a configuration in the flat state $\Delta/(NL) > 0.9995$ and in the buckled state $\Delta/(NL) < 0.9995$.

Possible explanations for this discrepancy are that the experimental wave is not perfectly periodic and the observed amplitude at the barriers is slightly smaller than the amplitude away from the barrier. The wavelength λ of the monolayer corrugation was obtained by visual inspection. Experiments with different numbers of plates, from 5 to 16, consistently gave $\lambda \simeq 2L$, as shown for $N = 16$ in the inset of Fig. 2.4.

To analyze the observed behaviour, we developed a mathematical model based on a balance between capillary forces, gravity and contact forces. The total free energy of the system is then given by the gravitation potential energy of the fluid (located both below the fluid interface and below the plates), and the interfacial energy of the fluid-fluid interface. Calling $h(x, z)$ the height of the fluid-fluid interface (see Fig. 2.5), and assuming that the plates pin the contact line at their edges [37], the gravitational potential energy contribution

to the total free energy is

$$E_g = \int_0^{\Delta} dx \left[\frac{1}{2}\tilde{\rho} g L h^2(x,0) + 2\int_0^{\infty} \frac{1}{2}\tilde{\rho} g h^2 dz \right], \tag{2.1}$$

where $\tilde{\rho} = \rho_l - \rho_a$ is the difference in density between the heavier fluid and the lighter fluids, x is the coordinate along the chain and z is the coordinate perpendicular to the chain in the plane of the unperturbed fluid interface, with $z = 0$ corresponding to the contact line on one side of each plate (see Fig. 2.5). The first term in Eqn. (2.1) is the gravitational energy of the liquid below the plates and the second term is the gravitational energy of the liquid in the two side menisci. The capillary energy associated with the menisci on both sides of the chain is

$$E_\gamma = 2\gamma \int_0^{\Delta} dx \int_0^{\infty} \sqrt{1 + \left(\frac{\partial h}{\partial x}\right)^2 + \left(\frac{\partial h}{\partial z}\right)^2}\, dz. \tag{2.2}$$

We neglect the contribution to the capillary energy due to the average displacement of the contact line in the vertical direction caused by the particle weight minus buoyancy (giving rise to the capillary monopole term important in the "Cheerios effect" [81]). The perimeter-averaged vertical interface displacement caused by the plate weight is of the order of $Bo_p \ell_c$ where $Bo_p = \rho_p g L t/\gamma$ is the particle Bond number and $\ell_c = \sqrt{\gamma/(\tilde{\rho} g)}$ is the capillary length [35, 82]. Based on this estimate, the average vertical contact line displacement is about $0.1\ell_c$. This deformation is not negligible. However, the interfacial energy associated to this displacement is approximately independent of Δ (the particle centers do not translate vertically), and thus the contribution to the buckling force or the selection of the dominant buckling mode is negligible. Note that we neglected the capillary contribution due to the fluid interface in the gap between the particles (i.e. in $-L < z < 0$). To enforce the constraint that the total length of the chain is constant, we add to the total free energy a constraint term

$$E_c = F\left[NL - \int_0^{\Delta} dx \sqrt{1 + \left(\frac{\partial h}{\partial x}\right)^2 \Big|_{z=0}} \right], \tag{2.3}$$

where F is a scalar Lagrange multiplier. Physically, F represents the contact force between the plates.

The Lagrangian to be minimized is obtained by adding the capillary and gravitational energy contributions, Eqns. (2.1) and (2.2) to Eqn. (2.3). Imposing

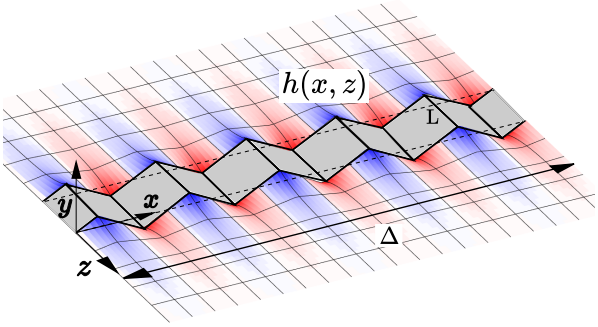

Figure 2.5: Sketch and notations of a chain of N plates of length L displaced by $NL - \Delta$. The air/liquid or the liquid/liquid side menisci pinned to the edges of the particles is indicated by $h(x, z)$. The color code indicates the vertical (along the y axis) deformation of the interface.

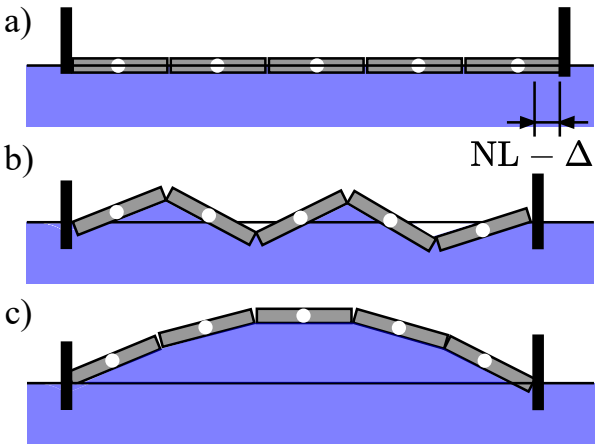

Figure 2.6: Upon compression of an initially flat monolayer (a), both configuration (b) and configuration (c) are local energy minima. We only observe configuration (b).

$\delta(E_g+E_\gamma+E_c)=0$, where δ denotes the functional derivative, yields two equations (the full expressions for δE_g, δE_γ and δE_c are given in Appendix 2.5). The first equation is the small-amplitude Young-Laplace equation governing the shape of the fluid-fluid interface for $-L>z>0$:

$$\tilde{\rho}gh=\gamma\left(\frac{\partial^2 h}{\partial x^2}+\frac{\partial^2 h}{\partial z^2}\right). \tag{2.4}$$

The second equation is the boundary condition at $z=0$:

$$\tilde{\rho}gLh-2\gamma\frac{\partial h}{\partial z}+F\frac{\partial^2 h}{\partial x^2}=0. \tag{2.5}$$

The small amplitude assumption holds for the 1D chain because the maximum amplitude is only $A/L\simeq 2.5\times 10^{-2}$ (see Fig. 2.4). Upon multiplication by L, equation (2.5) is a balance of moments. The first term represents the moment of the hydrostatic pressure force due to the weight of the fluid below the plates. The second term represents the moment of the vertical projection of the surface tension force at the contact line, located at $z=0$ and $z=-L$. The third term represents the moment of the contact forces F between the particles.

The leading-order Fourier mode solution of Eqn. (2.4) that matches the triangle-wave profile of the contact line is [34]

$$h(x,z)=Ae^{-z\sqrt{\left(\frac{2\pi}{\lambda}\right)^2+\frac{1}{\ell_c^2}}}\sin\left(\frac{2\pi x}{\lambda}\right), \tag{2.6}$$

where $\ell_c=\sqrt{\gamma/\tilde{\rho}g}$ is the capillary length. Equation (2.6) satisfies $h(x,z=0)=A\sin(2\pi x/\lambda)$ and $h(x,z\to\infty)=0$. For $\lambda\gg\ell_c$ and $\lambda\ll\ell_c$, the decay lengths of the meniscus in the z direction are ℓ_c and $\lambda/2\pi$, respectively. Thus, in the surface tension-dominated regime the buckling wavelength and the decay length of the fluid interface distortion are roughly of the same order of magnitude.

Substituting Eqn. (2.6) into Eqn. (2.5) yields the contact force as a function of the wavelength:

$$F=\frac{1}{4\pi^2}\delta\rho gL\lambda^2+\frac{1}{2\pi^2}\gamma\lambda\sqrt{(2\pi)^2+\left(\frac{\lambda}{\ell_c}\right)^2}. \tag{2.7}$$

Because of the small amplitude assumption the buckling force becomes independent of A. The capillary energy, the gravitational energies and the

constraint term are proportional to NL in the limit of small compression displacement (since $\Delta \approx NL$). Therefore, the buckling force is independent of N. In Fig. 2.6 we show two configurations of buckled chains, with $\lambda = 2L$ in configuration (b) and $\lambda = 10L$ in configuration (c). While both wavelengths are solutions to Eqn. (2.5), the absolute minimum of $F(\lambda)$ is the total energy minimum, similar to the buckling of an Euler beam [83]. Since $F(\lambda)$ is a monotonically increasing function of λ and wavelengths smaller than $2L$ are not possible, the equilibrium wavelength is

$$\lambda = 2L. \tag{2.8}$$

The contact force corresponding to $\lambda = 2L$ is the buckling force:

$$\frac{F_b}{\gamma \ell_c} = \frac{1}{\pi^2}\left(\frac{L}{\ell_c}\right)^3 + \frac{2}{\pi}\frac{L}{\ell_c}\sqrt{1+\left(\frac{L}{\pi \ell_c}\right)^2}. \tag{2.9}$$

Figure 2.7 shows $F_b/(\gamma \ell_c)\, vs.\, \sqrt{Bo} = L/\ell_c$, comparing Eqn. (2.9) with the experimental data. Here $Bo = \tilde{\rho} g L^2/\gamma$. Despite Eqn. (2.9) having no free parameters, the agreement between the experimental data and the theory is excellent, except for the smallest values of Bo where a perfect alignment of the plates cannot be ensured. For $Bo \gg 1$ the gravitational force dominates and $F_b \sim \tilde{\rho} g L^3$. In this regime, the buckling force is of the order of the weight of the liquid displaced by each plate as the chain deforms. For $Bo \ll 1$, $F_b \sim \gamma L$. In this regime, the buckling force is of the order of the capillary force exerted by the side meniscus on each plate. Equating the first and second terms in Eq. (2.9) provides a threshold $L/\ell_c \simeq \pi$ for the transition between the capillarity-dominated and gravity-dominated regimes.

Reference [84] reports compression experiments performed on an air bubble covered with a monolayer of spherical particles. The data shows both smooth buckling indentations of the order of the bubble size, and small-scale undulations of the order of the particle size. The authors explain the appearance of the small-scale undulations with a discrete model that includes a capillary energy contribution due to displacement of each particle from the plane of the fluid interface. Similar to ours, this model does not treat the particle monolayer as an elastic membrane (the model, however, does not include capillary-induced bending energy contributions which could be important for spheres [14, 32]). The scaling of this model is similar to ours but the physics is different: in our case the particle centers of mass do not translate with respect to the average plane of the interface when the dominant, small wavelength

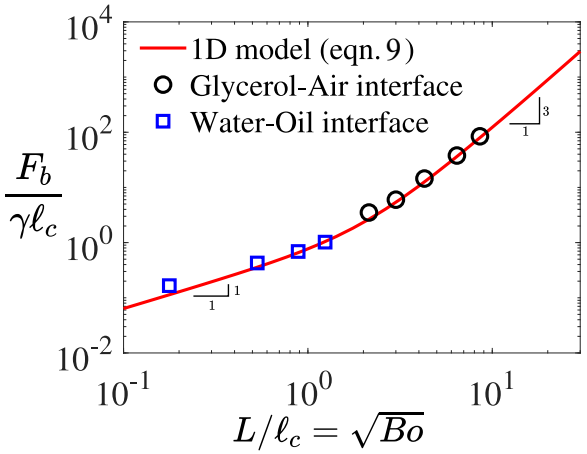

Figure 2.7: Normalized buckling force $F_b/(\gamma \ell_c)$ versus normalized particle length L/ℓ_c for the 1D chain experiments. The markers correspond to experimental data, blue squares for chains at a water-oil interface and black circles for chains at a glycerol/air interface. The red line is Eqn.(2.9).

mode is selected (see Fig. 2.6 (b)). The experiments are however interesting because they show that small-scale undulations could be superimposed on smoother ones in the case of spherical particles embedded in curved fluid interfaces.

2.3.3 Comparison of 1D model with 2D experiment

It is instructive to compare the prediction of the chain model to the experimental data for the 2D monolayer. The model predicts $\lambda = 2L$, close to the peak-to-peak value in the height-height correlation function measured from the 2D monolayer data (see Sec. 2.3.1). A peak-to-peak distance slightly larger than $\lambda = 2L$ is expected because the buckled regions are not exactly perpendicular to the laser line (for a non-zero angle between the laser line and the buckling direction, the measured peak-to-peak distance in the correlation function is larger than the actual separation between the "crests" of the monolayer).

A comparison between an estimate of the surface pressure obtained from 1D model and the measured surface pressure for 2D system (see Fig. 2.2 a) is also possible. The buckling surface pressure from Eqn. (2.9) is

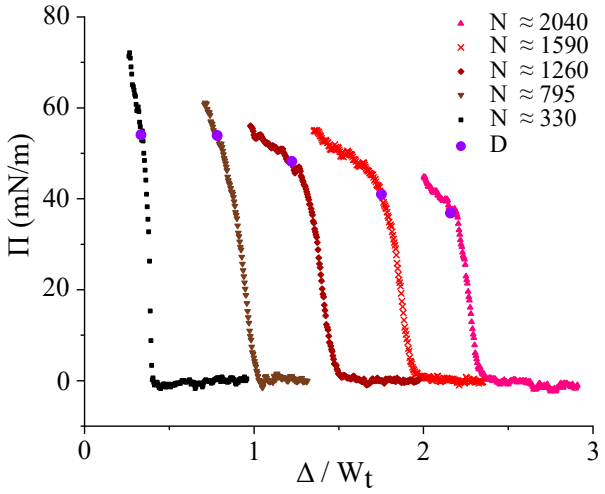

Figure 2.8: Surface pressure Π measured at the stationary barrier for 2D monolayers of $L = 1.5$mm hexagonal particles at a water/air interface against the distance between the barriers normalized by the trough width Δ/W_t for different number of plates. The points D (in purple markers) are the collapse points.

$$\Pi_b = \frac{F_b}{L} = \frac{1}{\pi^2}\tilde{\rho} g L^2 + \frac{1}{\pi^2}\gamma\sqrt{(2\pi)^2 + \left(\frac{2L}{\ell_c}\right)^2}. \tag{2.10}$$

Such a comparison should account for two differences. First, in the 1D chain the internal stress in the monolayer due to particle-particle contact forces is essentially homogeneous along the compression direction (on a scale $\gg L$). In the 2D assembly, the contact forces are instead a random function of position and orientation. Secondly, in the 2D monolayer the balance of forces on the entire monolayer should account for friction with the lateral walls [16, 85]. Evidence of the importance of the lateral walls in our experiments is the fact that the amplitude of the monolayer deformation is larger near the moving barrier (see panel C and D in Fig. 2.2 b). A larger deformation occurs in this region because the gradient of the surface pressure along the compression direction must balance the frictional stresses on the lateral walls, leading to a larger surface pressure and deformations near the moving barrier. However, the 1D chain model could still provide an estimate of the average value of Π in regions where buckling occurs and sufficiently away from the lateral walls.

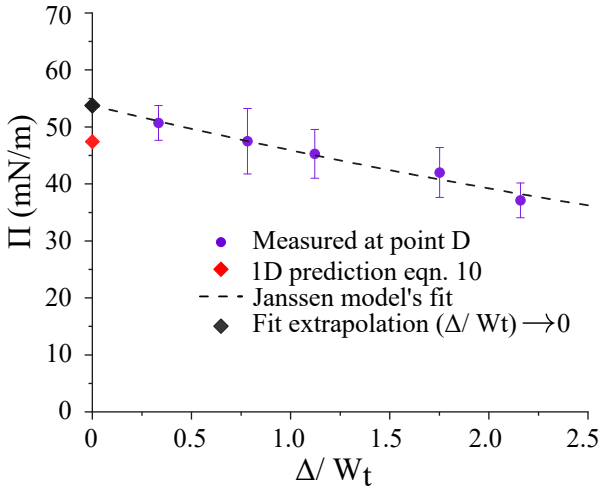

Figure 2.9: Surface pressure at collapse point D for 2D monolayers of $L = 1.5$mm hexagonal particles at a water/air interface, averaged over 3 realizations and plotted against the distance between the barriers (normalized by the trough width). The error bars represent the standard deviations. The dashed curve is the Janssen model's fit to the experimental data. The black marker is the extrapolation of the Janssen model's fit for $\Delta/W_t \to 0$. The red marker is the surface pressure predicted by the 1D chain model Eqn. (2.10).

We performed buckling experiments at different trough aspect ratios. Trough aspect ratios are changed by varying the number of particles between the barriers for a fixed trough width. The particle sizes are fixed ($L = 1.5$mm) in all experiments. Figure 2.8 shows the surface pressure profiles for the 2D monolayer as a function of Δ/W_t for $N \simeq 330 - 2040$. We see from this curve that the surface pressure profile depends on the initial trough area, another manifestation of the effect of lateral wall friction [16, 85, 86].

Figure 2.9 shows the experimental data for the surface pressure in the 2D monolayer, averaged over 3 different measurements, for different values of Δ/W_t. This figure is obtained from Fig. 2.8 by reporting the value of Π and Δ/W_t corresponding to the collapse point D. In order to compare the collapse surface pressure in the 2D monolayer with the 1D model we used a Coulomb model for the lateral wall friction as done in [16] for a monolayer of spherical particles. This model assumes that the frictional force per unit length is proportional to the local values of Π according to a proportionality constant μ_{wall}. This approximation yields an exponential decay law also referred to as the Janssen model, $\Pi = \Pi_0 \exp(-2\mu_{wall}\nu\Delta/W_t)$ [16]. Here Π_0 is the pressure at the moving barrier and ν is the ratio of surface pressures perpendicular and parallel to the compression direction. Assuming $\nu = 1/3$ [16], the best fit to the data (dashed curve in Fig. 2.9) gives $\Pi_0 = 53.8\ mN/m$ and $\mu_{wall} = 0.24$. The trough walls are made of PLA plastic. While we could not find the data for the friction coefficient of Mylar on PLA in water, the reported friction coefficients for Mylar against different engineering materials such as copper and wood are in the range $0.13 - 0.41$ [87]. The black square dot in figure 2.9 is the extrapolation of the experimental data for the 2D monolayer to $\Delta/W_t = 0$, which yields $\Pi_0 = 53.8$mN/m. The red square dot in figure 2.9 is obtained by using the parameters of our problem in Eqn. (2.10). The value of Π_0 from the friction model is larger than the value from the 1D chain model, but the difference is small (about 13%). Considering the simplicity of the chain model, the agreement with the 2D data is surprisingly good. We would like to emphasize that, given the limited range of Δ, we cannot establish the full validity of Janssen model for our system. The fitting via this model is used here only to illustrate the effect of lateral wall friction on the expected trend of Π and the limited effect of friction in the limit $\Delta/W_t \to 0$.

As stated before, the 2D monolayer differs from the 1D chain in the distribution of contact forces between the particles. Statistics of contact forces between jammed particles have been studied extensively in the context of granular materials [86, 88–90]. These studies reveal that the probability of

contact forces attaining a value f larger than the mean value $\langle f \rangle$ decays fast, approximately as $p(f/\langle f \rangle) \sim \exp(-\beta f/\langle f \rangle)$, with β an $O(1)$ numerical coefficient [86, 88–90]. Therefore it is expected that the monolayer contains few contact forces that are large compared to the average contact force [86]. Upon monolayer compression, the first buckling events will occur for groups of particles for which the contact force exceeds the estimate in Eqn. (2.9). Because such large forces are small in number, the buckling regions are initially localized, as seen in panel B in Fig. 2.2 b. If the mechanical response of the monolayer is dominated by these spatially scattered regions, Eq. (2.10) could provide an upper bound for the surface pressure measured at the barrier in the 2D experiment.

In our experiments, the buckled zones do not show long range periodicity. Even for large compression displacements the average height-height correlation function becomes negligible for $\tilde{x} \approx 7L$ (see Fig. 2.3 (b)). A possible explanation is spatial localization of forces chains. Studies on jammed granular packing reveal that the force chains do not extend over more than a few particle diameters [91, 92].

In the 1D chain, the decay length of the side meniscus is $L/\pi \sim 0.3L$ in the capillary regime. In a randomly packed 2D system, the average distance between the edges of the particle is $L(1/\sqrt{\phi} - 1)$, where ϕ is the surface fraction of the plate particles. For $\phi \simeq 0.84$, the value appropriate for a random close packing of disks [85], we obtain an average distance of $\simeq 0.1L$ between the particle edges. Therefore in the capillary regime the meniscus decay length and the distance between the particle edges are of the same order of magnitude. Because of this, the solution for the 1D chain could be used as a local approximation to the contact force in the 2D system. In the gravity-dominated regime the side meniscus deformation gives a negligible contribution to the contact force, so also in this regime the application of the 1D model to the 2D system is justified as a first approximation.

2.3.4 1D model with bending rigidity

Key in our derivations is the absence of bending energy in the energy functional. Experiments with graphene oxide [26] seem to be compatible with the our model, but the observed wavelength is slightly larger than 2L. A possible explanation for observing wavelengths larger than $2L$ could be the presence of a small but finite bending rigidity of the monolayer. An extension of Eqn. (2.5) accounting for an effective monolayer bending rigidity (per unit width) D is

$$DL\frac{\partial^4 h}{\partial x^4} + \tilde{\rho}ghL - 2\gamma\frac{\partial h}{\partial z} + F\frac{\partial^2 h}{\partial x^2} = 0, \tag{2.11}$$

Substituting Eqn. (2.6) into Eqn. (2.11) gives

$$\frac{F}{\gamma L} = \frac{D}{\gamma L^2}\left(\frac{2\pi L}{\lambda}\right)^2 + 2\left(\frac{\lambda}{2\pi L}\right)\sqrt{1 + Bo\left(\frac{\lambda}{2\pi L}\right)^2} + Bo\left(\frac{\lambda}{2\pi L}\right)^2. \tag{2.12}$$

For $\gamma = 0$ Eqns. (2.11) and (2.12) predicts $\lambda_b = (D/\tilde{\rho}g)^{1/4}$, which is the result of Ref. [15]. For $D/(\gamma L^2) \ll 1$ bending rigidity effects are negligible and we recover the results of Sec. III b. For intermediate values of $D/(\gamma L^2)$, the wavelength that minimizes the force is larger than $2L$. Its precise value can be found by solving $dF/d\lambda = 0$. For $Bo \ll 1$, gravity becomes negligible and the buckling mechanics is dominated by bending rigidity and capillary forces. The buckling wavelength in this limit is

$$\frac{\lambda_b}{2L} = max\left\{1,\ \pi\left(\frac{D}{\gamma L^2}\right)^{1/3}\right\} \tag{2.13}$$

and the corresponding buckling force is

$$\frac{F_b}{\gamma L} = max\left\{\frac{2}{\pi},\ 3\left(\frac{D}{\gamma L^2}\right)^{1/3}\right\}. \tag{2.14}$$

Figure 2.10 shows $F/(\gamma L)$ *vs.* $\lambda/(2L)$ for $Bo = 0$ and selected small values of $D/(\gamma L^2)$. The wavelength that minimizes F is indicated by the red dots. From Eqn. (2.13) and (2.14) we see that both the buckling wavelength and buckling force are proportional to $(D/(\gamma L^2))^{1/3}$, thus $F_b \propto \lambda_b$ (red dashed line in Fig. 2.10). For increasing values of $D/(\gamma L^2)$ the wavelength that minimizes the force becomes larger than $2L$.

In an interfacial monolayer of 2D nanosheets, the nanosheets can overlap slightly [18, 25, 93]. This overlap can result in a small but nonzero effective bending rigidity because of the attractive force between the sheets in the overlapping region. In Ref. [94] a Lennard-Jones potential was used to model the attractive interaction potential between parallel sheets of graphene. Using the Lennard-Jones potential, and assuming that the angle between pairs of

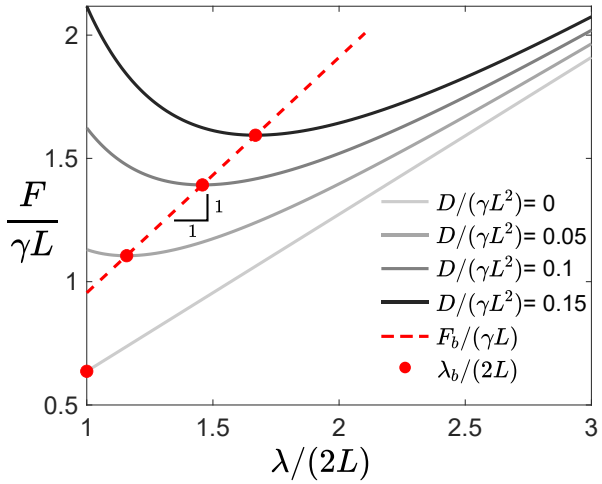

Figure 2.10: Normalized force $F/(\gamma L)$ as a function of normalized wavelength $\lambda/(2L)$ for small values of normalized bending rigidity and $Bo = 0$ (see Eqn. (2.14)).

overlapping sheets is small, it is easy to estimate the effective bending rigidity corresponding to an average overlap length ℓ (see Appendix 2.5):

$$D \simeq \frac{40\Gamma L \ell^3}{3r_0^2}. \tag{2.15}$$

Here Γ is the adhesion energy per unit area and r_0 is the nanometric equilibrium separation between the nearly-parallel sheets. The model suggests a strong ℓ^3 scaling with the overlap length. For graphene oxide sheets in high-humidity conditions, molecular dynamics simulations suggest $r_0 \simeq 7.7 - 12$ A° [95, 96] and $\Gamma \simeq 0.1 - 0.2$ J/m^2 [18, 97]. Taking realistic values $\Gamma = 0.2$ J/m^2, and $r_0 = 12$ A° and an average sheet length $L = 1\mu$m, $D/(\gamma L^2)$ is estimated to be 0.02 and 26 for $\ell = 1$nm and 10nm, respectively (assuming the surface tension of water, $\gamma = 0.07$ J/m^2). The corresponding wavelengths are 2 μm and 20 μm, respectively. An overlap length of 1 nm does not change the wavelength appreciably from 2L, whereas an overlap length of 10 nm increases the buckling wavelength to $20L$. For a randomly distributed overlap lengths between 1 - 10 nm, the predicted wavelength range is $2 - 20L$ which is is similar to wavelength range observed in the experiments with graphene oxide [26]. The inclusion of the effect of overlaps therefore enables the analytical predic-

tion developed for small amplitudes to be closer to the experimental data for graphene oxide nanoparticles.

2.4 Conclusions

We have measured the amplitude of deformation, wavelength and force on the barrier for a two-dimensional and one-dimensional monolayer of plates trapped at a fluid-fluid interface and subject to uni-axial compression. The amplitude and wavelength of the corrugations of the 2D monolayer were measured by a laser scanning technique.

The model we have developed to predict the experimental data for the linear chain (one-dimensional monolayer) predicts the buckling force well over a wide range of values of L/ℓ_c, where ℓ_c is the capillary length and L is the particle length, and without adjustable parameters (Fig. 2.7). The 1D chain model provides a reasonable order of magnitude estimate of the buckling surface pressure Π for the two-dimensional monolayer, provided that this pressure is identified as the collapse pressure corresponding to the point D in Figs. 2.2 and 2.8. The chain model does not contain a dependence on the trough aspect ratio Δ/W_t, but the inclusion of frictional forces with the lateral wall via a Coulomb friction model enables us to model the observed dependence of Π on Δ/W_t. A more complete model should include statistics of force chains, for which theories developed for 2D granular systems [98,99] could be applicable. The chain model predicts a buckling wavelength $\lambda = 2L$, independent of L/ℓ_c. The 2D monolayer does not display a regular wave pattern, but the characteristic local wavelength in the regions where buckling occurs is of the order of the particle size, as in the 1D chain model. Uni-axial compression of monolayers of spherical particles gives smooth undulations with a wavelength $\lambda \sim \sqrt{\ell_c L}$ [14], different from the one we observe. In our case, the effective bending rigidity of the monolayer is negligible, as the plates can "hinge" at their contact points without a bending energy penalty. In the case of spheres, even in the absence of colloidal force contribution bending energy can originate from the motion of the contact line on the surface of each particle as the mean interface curvature changes [32]. An indication of this is that the order of magnitude of the effective bending rigidity corresponding to $\lambda \sim \sqrt{\ell_c L}$ is $\gamma\ d^2$; this can be seen as the change in interfacial energy as a sphere of diameter d protrudes in the fluid interface over a distance comparable to d. In our case, the undulations of the contact line relative to the particles, if present, are at most limited to a scale $t \ll L$, where t is the particle thickness.

The corresponding changes in interfacial energy upon a change in interfacial curvature is $O(\gamma Lt)$ [37,100]. For $L/\ell_c \ll 1$ and $t/L \ll 1$, this contribution is negligible in comparison to the dominant contribution, of order $\gamma A\lambda \sim \gamma L^2$, due to the rotation of each particle as the monolayer is compressed. In Ref. [17] a scaling $\lambda \propto L$ was reported for experiments with spheres, but only for very small compressive displacements, whereas $\lambda \propto \sqrt{L}$ was observed for larger displacements. Perhaps this transition could be the result of depinning of the contact line at large compression. These comparisons suggest that both the particle aspect ratio and contact line motion could determine the characteristic buckling wavelength.

In our experiments, we prepare the particle-laden interface ensuring no initial overlaps. If a monolayer of 2D nanosheets is prepared with care, overlaps can be largely prevented (nanosheet stacking requires overcoming an energy barrier [93]), but probably not completely eliminated at large degrees of compression. Tuning the pH of the liquid [66] or adding surfactants [31] has been shown to suppress the stacking of 2D materials at fluid interfaces, so one may realize the experimental systems described in the current paper using real 2D materials. If particle overlaps did occur even before the compression of the particle-laden interface, the analysis would need to account for particle-particle interactions as well as statistics of the geometry of the overlapping regions. Overlaps contribute to a nonzero bending rigidity as a result of the adhesion forces between the nanosheets. We have shown mathematically that this effect increases the buckling wavelength compared to 2L (see Fig. 2.10).

Compression of plate-like particles trapped at fluid interfaces occurs in a variety of applied settings, for instance in the manufacturing of thin films [25,31,101], in the deformation of Pickering emulsions [71,102], or in the production of crumpled graphene by aerosolization [103]. This work contributes to our understanding of the link between particle shape, contact mechanics, and response of the fluid interface during the compression of monolayers of plate-like particles of controlled geometry.

2.5 Appendix

Appendix A: Micro force sensor

The cantilever force sensors are Mylar sheets with lengths of 80 and 100 mm, a width of 10 mm, and a thickness of 125 μm. One end of the sheet is clamped and the free end is unconstrained. The free end is passed through another Mylar sheet, with a rectangular hole, which acts as the barrier (see Fig. 2.11). The deflection of the Mylar sheet (ξ) from its undeformed position is calculated by imaging from the side view.

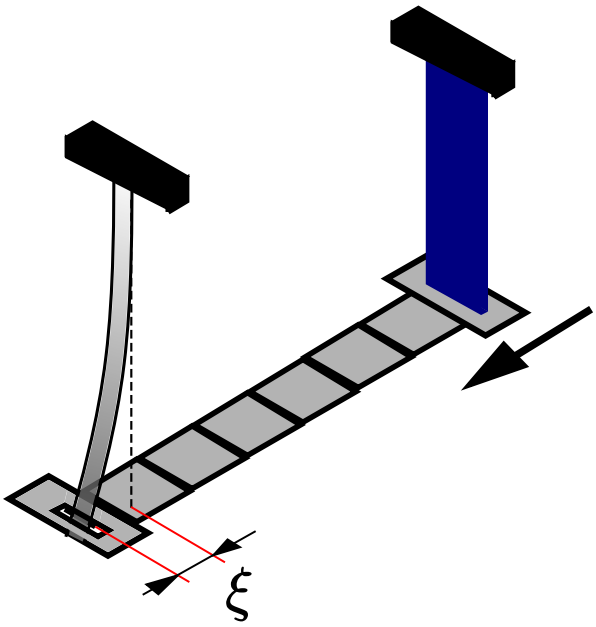

Figure 2.11: Forces measurement with cantilever force sensor.

To calibrate the force sensors, the fixed end of the cantilever is mounted on a manual precision stage and the free end is rested on a knife edge placed on a Mettler Toledo precision micro-balance. Imposing successive displacements of 0.5 mm in the manual precision stage, the corresponding forces are read from the balance. Figure 2.12 shows force *vs.* displacement of the manual stage. The force values are linear with respect to the displacement for displacements as larger as 5 mm. The slope of the line fitted to the experimental data gives the stiffness k of the beam.

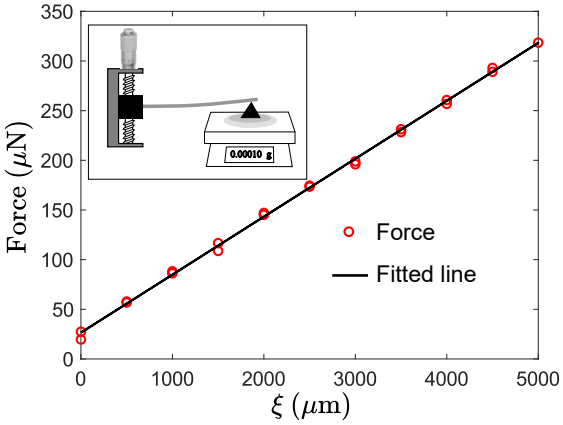

Figure 2.12: Calibration curve of the force sensor. The inset shows the schematic of force sensor calibration with precision balance.

Appendix B: Dependece of amplitude on Δ in 1D experiments

A simple geometric argument assuming that the buckled 1D system is a perfectly periodic triangular wave gives $A/L = (1/2)\sqrt{1-(\Delta/(NL))^2}$ without considering boundary effects. We compare this analytical prediction to the experimental data for the mean amplitude in 1D experiments (see Fig. 2.4) shown in Fig. 2.13. To enable the comparison, we shift the experimental data so that $\langle A \rangle = 0$ exactly when $\Delta = NL$. It can be seen that the simple model gives the correct trend. However it over predicts the mean amplitude by about 40%.

Appendix C: Euler-Lagrange minimization

The variation of the gravitational energy in the 1D model is

$$\delta E_g = \int_0^\Delta dx \tilde{\rho} g L h_0 \delta h_0 + 2\int_0^\Delta dx \int_0^\infty \tilde{\rho} g h \delta h dz.$$

Here $h_0 = h(x, z = 0)$. The variation of the capillary energy is

$$\begin{aligned} \delta E_\gamma &\simeq 2\gamma \int_0^\infty [h_x \delta h]_0^\Delta \, dz + 2\gamma \int_0^\Delta [h_z \delta h]_0^\infty \, dx \\ &- 2\gamma \int_0^\infty \int_0^\Delta (h_{xx} + h_{zz}) \delta h dx dz \end{aligned}$$

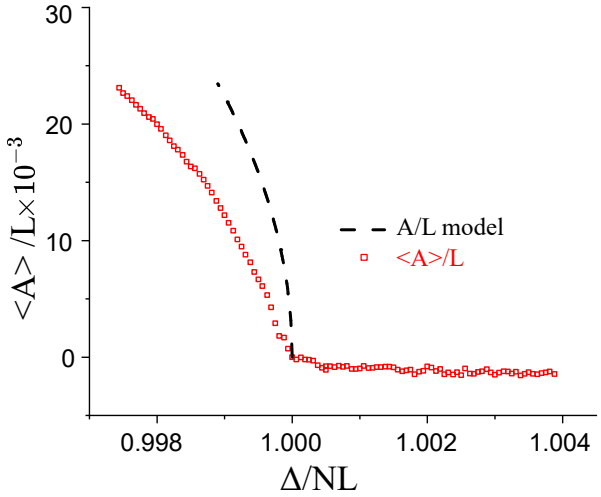

Figure 2.13: Amplitude data in Fig. 2.4 plotted against the analytical prediction $A/L = (1/2)\sqrt{1-(\Delta/(NL))^2}$.

and the variation in length constraint evaluated at $z = 0$ is

$$\delta E_c \quad = \quad -F\left[h_{0_x}\delta h_0\right]_0^{\Delta} + F\int_0^{\Delta} h_{0_{xx}}\delta h_0 dx$$

At equilibrium, the sum $\delta(E_g + E_\gamma + E_c)$ is zero for an arbitrary δh, from which we get Eqn. (2.4) and for an arbitrary δh_0 gives Eqn. (2.5).

Appendix D: Surface pressure vs. Δ/Δ_0

Fig. 2.14 shows the data presented in Fig. 2.2 a) with a different normalization for compression displacement Δ.

Appendix E: Bending rigidity due to overlap between two adhesive plates

The equilibrium distance between two nanosheets is determined by the competition between the attractive van der Waals and the repulsive electrostatic forces between the solid surfaces. A Lennard-Jones potential has been used to model the interaction between two nanosheets in [104, 105]. We use the

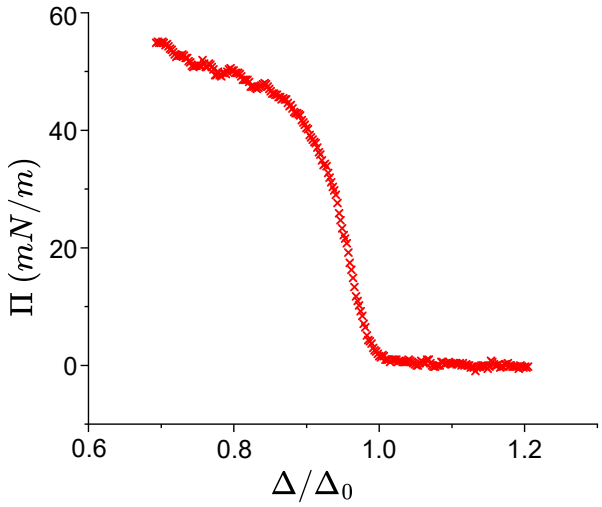

Figure 2.14: Surface pressure Π versus normalized separation distance Δ/Δ_0, where Δ_0 is the compression distance at which Π becomes finite.

standard 4-10 Lennard-Jones potential energy of interaction (per unit area) between two thin parallel plates [94]:

$$\phi(r) = \frac{\Gamma}{3}\left(5(r_0/r)^4 - 2(r_0/r)^{10}\right),$$

where r is the separation distance between the plates, r_0 is the equilibrium separation and $\Gamma = \phi(\infty) - \phi(r_0)$ is the adhesion energy. If the separation distance $r > r_0$ the plates attract each other due to van der Waals forces and if $r < r_0$ the plates repel each other due to electrostatic forces. In the limit of small displacement around r_0, a quadratic approximation to the energy per unit area is [105]

$$\phi(r) \simeq \frac{20\Gamma}{r_0^2}(r - r_0)^2.$$

We consider a 1D chain of plate-like particles at a fluid interface where each particle pair has a small overlap of length ℓ (see Fig. 2.15). We model the interface as a continuous curve parameterized by $\theta(s)$, the local rotation angle along the curvilinear coordinate s. The configuration of a single overlap is illustrated in the inset of Fig. 2.15. Referring to this figure, we take r in the direction normal to the top plate and ζ in the direction tangential to the top plate. Under compression the plates are rotated with respect to each other by

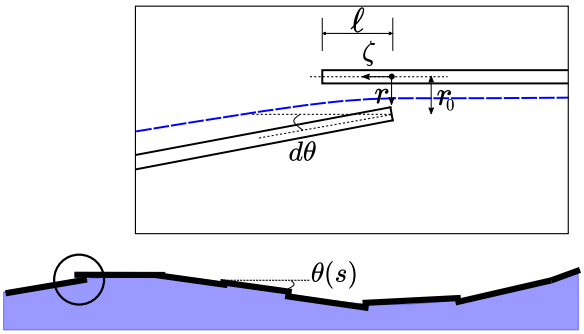

Figure 2.15: Schematic of a fluid interface populated by slightly overlapping sheets. The inset shows the zoom of the overlap region. The blue dashed line is the average position of the particle-laden fluid interface.

an angle $d\theta$. The displacement of the second plate is $r(\zeta) = r_0 + \zeta \tan(d\theta)$ (see figure 2.15). The energy required to impose this rotation for a particle pair is

$$dE \simeq w \int_0^{\ell} \frac{20\Gamma}{r_0^2}(r(\zeta) - r_0)^2 \, d\zeta.$$

Carrying out the integration for $|d\theta| \ll 1$ we obtain

$$dE \simeq \frac{w}{2}\left(\frac{40\Gamma\ell^3}{3r_0^2}\right) d\theta^2$$

Multiply and divide by $(ds)^2$, where ds is an infinitesimal element of curvilinear coordinate, we obtain

$$dE \simeq \frac{w}{2}\left(\frac{40\Gamma\ell^3}{3r_0^2}ds\right)\left(\frac{d\theta}{ds}\right)^2 ds. \tag{2.16}$$

For a continuous surface, the bending rigidity D (per unit width) is defined so that $dE = \frac{1}{2}wD\kappa^2 ds$, where $\kappa = d\theta/ds$ is the curvature. Comparing this expression to Eqn. (2.16) we obtain $D = (40\Gamma\ell^3)/(3r_0^2)ds$. In our case, because dE represents the energy per particle pair, ds is the distance between two particle centers, i.e. $ds = L - \ell$. For $\ell \ll L$ the estimate of the bending rigidity is $D = (40\Gamma\ell^3)/(3r_0^2)L$, as in Eq. (2.15). The assumption of a continuous

surface is reasonable if $N \gg 1$, where N is the total number of plates [106]. The bending rigidity thus scales proportionally to the adhesion energy Γ and depends strongly on the overlap length ℓ.

Chapter 3

Evaporation driven buckling of a drop laden with graphene oxide nanosheets

The time-dependent shape of an evaporating spherical water drop containing graphene oxide (GO) nanosheets is measured for varying solid concentration, humidity level, and pH. The drop is sitting on a superhydrophobic surface, depinned from it. Three different stages of evaporation are identified: isotropic retraction of the drop interface, buckling of the shell of particles accumulated at the fluid interface, and shrinking of the buckled shell at constant shell shape. Marked differences between acidic and basic drops are reported. It is argued that this feature is caused by the pH-dependent interfacial adsorption of the GO particles. For intermediate values of GO concentration, dried capsules with remarkably repeatable folding patterns could be obtained, whose mode numbers are compatible with those predicted by an inertialess, linear elastic shell model. When redispersed in water, the dried capsules from acidic drops retain their shape better than capsules from basic drops.

Chapter based on publications:
Suriya Prakash, Eva Krolis, Alvaro Marin & Lorenzo Botto, *Evaporation driven buckling of a drop laden with graphene oxide nanosheets*, Soft Matter (2025).
Suriya Prakash & Lorenzo Botto, *Evaporation driven particle adsorption at drop interface* (in preparation).

3.1 Introduction

A small spherical drop containing micro or nanoparticles can form a semi-solid (visco-elastic) particle "skin" when the droplet evaporates. The "skin", or particle shell, is caused by the motion of the contracting fluid interface that sweeps the particles suspended inside the drop [60, 108]. In addition to its fundamental interest, this phenomenon has been studied due to its application to spray drying, for the large-scale production of dried microstructured particles to be used in food products [109], lubricants [5], pharmaceuticals [38] and functional materials [40–42, 44].

The recent explosion of interest in 2D material nanosheets (graphene, graphene oxide, boron nitride, MXenes, MOS_2, etc.) has stimulated research on the use of evaporation driven buckling ("crumpling") of shells formed from droplets laden with dilute suspensions of these colloidal materials [3,4,10,110]. Graphene oxide (GO), which is easily dispersable in water at dilute concentrations, is the most used 2D material in spray drying applications [45, 48, 111], but its behaviour in evaporating drops is not well understood.

This paper reports a comprehensive investigation of the evaporation of GO-filled droplets and of the different stages that characterise the shell buckling process. We work with single millimeter-sized droplets that are placed on a superhydrophobic surface. This is a common configuration in which colloidal droplets adopt spherical shapes during most of the evaporation process until buckling occurs. This configuration has prior been used to investigate evaporating particle-laden droplets [112–114]. As far as we are aware, the current study is the first report of repeatable measurements of the time-dependent single GO drop evaporation under controlled conditions of humidity, GO concentration, and pH.

Only very few experimental studies on evaporation of GO droplets are available [45, 47–49, 115]. These studies have provided a useful characterization of the shapes of dried capsules formed from spray drying, but have not provided insights into the drying process at the level of a single drop. Spray drying of GO-water suspension has been reported to produce dried capsules whose shape are highly polydispersed, and dependent on the flow conditions (temperature, humidity level, flow rate). A relevant study on GO reports dissolution of an aqueous GO solution deposited on a hydrophobic substrate immersed in the liquid phase of ethanol in toluene [116]. In this study, the time dependent radius of the drop was measured, and found to follow a diffusive dynamics (square of the drop radius R linear in time t). In this study, the structure

formed were porous, but not hollow. Studies on evaporation of drop containing *spherical* colloids are abundant [61, 62, 113, 114, 117–120]. These studies indicate that a particle shell is only obtained for large values of the Péclet number Pe based on the translational diffusivity D_p of the particles, the initial drop radius R_0 and the characteristic velocity v_i of the fluid interface (or alternatively based on the ratio of diffusion and evaporation times [58–60]). For a given temperature, the interface velocity depends primarily on the humidity level, with low humidity giving fast evaporation because of the large difference in water vapour concentration between the drop surface and regions away from the drop surface. For slow drying, Brownian diffusion leads to a uniform distribution of particles inside the drop and therefore to dried structures that are not hollow. The thickness of the shell, and therefore whether a hollow capsule or a filled ball is obtained, depend also on the initial particle concentration ϕ_0 [108, 121]. Assuming that all the particles accumulate in the shell adjacent to the fluid interface, the shell thickness can be estimated from a basic mass conservation argument [60].

A possible distinction between GO and other colloidal particles is in the interfacial adsorption properties. GO is known to be amphiphilic, i.e. it has a tendency to adsorb at fluid interfaces [25,66,102]. The degree of amphiphilicity depends on the amount of oxygen groups present at its surface, but adsorption energies much larger than the thermal energy has been reported both in simulation and experiments [18, 23]. Furthermore, the important effect of GO on interfacial rheology of flat interfaces is well recognised [26]. Adsorption of GO at fluid interfaces is pH dependent [23, 66]. The amphiphilic character of GO may have implications for the onset of buckling, and that is why we include pH in our controlling variables. When a fluid interface is populated with adsorbed particles, buckling upon interface compression occurs even when a thick particle layer is not present in the region adjacent to the interface [67, 77, 122, 123]. The possible importance of GO amphiphilicity on interfacial stresses has not been discussed in the context of GO droplet evaporation experiments.

The literature on evaporation-driven buckling, also of spherical particles, has up to this point only focused on the effect of hydrophilic particles, i.e. particles that are completely wet by the liquid. Buckling can occur when the compression of the shell formed by particles completely wetted by the liquid is sufficiently large that the force of repulsion between charge-stabilized particles is overcome and therefore the particle adhere to each other [60]. For large repulsive forces, charge-stabilised particles can also form a glassy repulsive state at volume fractions even smaller than the packing fraction. If the pressure

corresponding to this repulsion is sufficiently large, a buckling instability can occur [62]. These explanations are plausible and may apply to most cases, but neglect the possible contributions of interfacial particles. To study the effect of interfacial particles on the onset of buckling, we also performed Brownian dynamics simulations in model 2D drops.
The shape of the dried GO buckled structure (capsule) is also of interest, because the morphology of the capsule determines its surface area and affects the stability against aggregation of the capsules upon re-dispersion in solution [45]. The morphology of buckled shells obtained from drying drops containing spherical colloids have been studied experimentally in Refs. [59, 60, 119, 124]. These experiment reported the formation of either torus-shaped capsules [59, 119, 124] or capsules with multiple depressions [60, 61]. The experiments of Ref. [61] with spherical colloids are particularly relevant as the authors could obtain buckling shapes with high repeatability, by a careful control of the initial drop diameter and solid concentration. The buckled shapes were found to depend on the rate of drying. Specifically, the number of depressions were found to increase for increasing evaporation rates [61]. A possible cause of this correlation was not proposed.
In our experiment, we are able to control the main parameters that govern the evaporation process and the main particle transport characteristics, namely the initial GO particle concentration ϕ_0, the humidity level RH, and the solution's pH. The use of a camera, by which we can observe the drop from the side, allows us to observe the different stages and rates of evaporation, detect with precision the onset of buckling and quantify the post-buckling morphologies. Scanning Electron Microscopy allows us to analyze the shape of the dried and buckled GO capsules.

3.2 Experimental methods

To study the evaporation of a single GO drop, we place a drop of controlled diameter on a superhydrophobic substrate. The superhydrophobic surface is a SiO_2 substrate with fractal-like micro-structure, coated with fluorooctatrichlorosilane [114]. The setup is contained in an acrylic chamber equipped with a humidity controller that maintains a set relative humidity RH (Fig. 3.1).
Due to the superhydrophobicity of the substrate, the drop rolls if the substrate is not perfectly horizontal. Therefore, the humidity chamber with the substrate is mounted on an anti-vibration table on leveling screws. The drop is

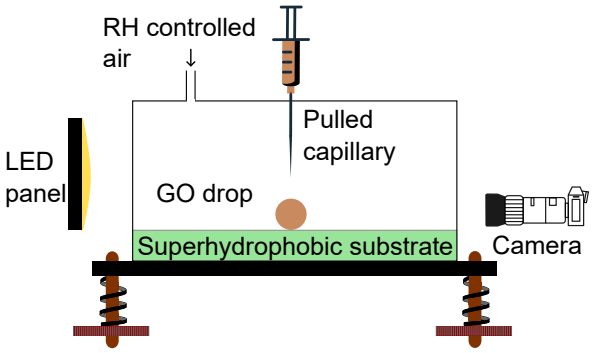

Figure 3.1: Schematic of the experimental setup.

produced by a syringe with the pulled capillary needle. The syringe is mounted on a precision linear stage platform that is used to gently place the drop on the substrate. We used a 1 ml syringe (B Braun Injekt-F Fine Dosage) housed in a 3D printed screw feeder. The initial drop diameter $2R_0 = 1.5 \pm 0.03$ mm is smaller than the capillary length, so the drops are approximately spherical. The drop is observed from the side by a camera equipped with a zoom lens, with a time resolution of 1 fps. The drop projected area A and contact angle are measured by detecting the drop edges with an in-house developed MATLAB code. The drops of pure water and GO suspension are in a Cassie-Baxter state and undergo evaporation at a constant contact angle ($\theta \approx 155°$) for most of the drop's life time (see Appendix A).

The graphene oxide suspensions are purchased from Graphenea. The average lateral size of the particles is $\ell = 1.08 \pm 0.44$ μm measured by scanning electron microscopy (SEM, JEOL JSM 6500 F). The particle thickness is $t = 1.00 \pm 0.14$ nm measured by atomic force microscopy (Bruker). See Appendix B for more details on sample preparation and characterization of sheet sizes. The densities of the purchased solutions are measured by a density meter (DMA 5000 Anton Paar). The density of the suspension is $\rho_{GO-sus} = \phi\rho_{GO} + (1-\phi)\rho_w$, where ρ_{GO-sus}, ρ_w and ρ_{GO} are the densities of purchased GO suspension, water and GO sheets, respectively. From this expression, the volume fraction ϕ of GO particles is calculated as $(\rho_{GO-sus} - \rho_w)/(\rho_{GO} - \rho_w)$. The density of water and GO suspension are measured with an accuracy of ± 1 kg/m^3. By assuming that the density of the GO sheets [125] is $\approx 2000 \pm 100$ kg/m^3, the volume fractions of GO in the suspensions is calculated to be $\approx 0.0023 \pm 0.0002$ and $\approx 0.0034 \pm 0.0004$ for acidic and basic suspensions,

respectively.
The bending energy of the GO sheets used in this study is of the order $Et^3 \sim 2 \times 10^{-16}$ J taking $E = 200$ GPa [126], which is much larger than $k_BT \sim 4 \times 10^{-21}$ J. Thus the sheets do not fold on themselves due to thermal fluctuations. Moreover, it has been shown by in-situ confocal microscopy [127] that GO sheets remain flat when suspended in water, and at high concentration they show the nematic order expected for relatively rigid sheets [128].
The Péclet number, based on the drop drying time τ_{dry}, is $Pe = R_0^2/(D_p\tau_{dry})$ [60], where D_p is the translational diffusion coefficient of the GO particles. The particle diffusivity is calculated as $D_p = k_BT/(f\mu\ell)$, where k_B is the Boltzmann constant, T is the absolute temperature, μ the viscosity of water, and f the coefficient of hydrodynamic resistance to translation. Since GO sheets are thin and can be assumed to remain planar in aqueous dispersion at not too high values of the shear rate [127], we use for f the value $48/7$ appropriate for isotropically oriented, infinitely thin disks [129]. The diffusion coefficient is estimated to be 5.9×10^{-13}, leading to a Péclet number in the range $\sim 150 - 500$ for RH varying between 30% and 80%. The Stokes settling velocity v_s of the GO particles, which can be estimated with the formula $v_s = \pi(\rho_{GO} - \rho_w)\ell tg/(4f\mu)$ for disks, is much smaller that the air-water interface velocity v_i. Since $v_s \ll v_i$, we neglect the effect of gravity on the particle distribution.
The pH of the purchased suspensions are measured using a pH meter (Metrohm) and found to be ≈ 2.5 and ≈ 8.0 for acidic and basic suspensions, respectively. Milli Q water (18.2 MΩ.cm at 25° Celcius) was used to dilute the parent suspension to a range of solid volume fractions $\phi_0 \approx 0.57, 2.8, 5.7 \times 10^{-5}$ for both acidic and basic drops. The corresponding measured pH was approximately $5, 4.5, 4$ for acidic suspensions. For the basic suspensions, the pH was slightly larger than 7 for all the three volume fractions.

3.3 Simulation method

The evaporating drop is modeled in two dimensions as a circle with a shrinking radius. The radius of the drop follows the d-squared law: $R(t) = (R_0^2 - kt)^{1/2}$, where t is time in seconds and $k = R_0^2/t_e$; here t_e is the drying time of a drop without particles. The Péclet number is $Pe = R_0^2/(D_pt_e)$, where D_p is the diffusion coefficient of the particles. The particles are modeled as discs of diameter $d_p = 1$ μm and are homogeneously distributed within the 2D drop with initial radius $R_0 = 100d_p$. The corresponding initial solid concentration

(area fraction) is $\phi_0 = N(d_p/2R_0)^2$, where N is the number of particles in the drop. The inertia of colloidal particles is negligible and therefore neglected [58]. The particle positions are updated by solving the force balance on each particle and by adding a random displacement due to Brownian motion. The updated position of the particle i after time step dt is

$$\vec{x}_i(t+dt) = \vec{x}_i(t) + \vec{\zeta}(2D_p dt)^{1/2} + \frac{dt}{3\pi\mu d_p}\left[\vec{F}_{pp,i} + \vec{F}_{s,i}\right], \tag{3.1}$$

where $\vec{F}_{pp,i}$ is the inter-particle repulsive force on i due to all the other particles, $\vec{F}_{s,i}$ is the particle-interface interaction force and $(2D_p dt)^{1/2}$ corresponds to the displacement due to Brownian motion [130]. Here $\vec{\zeta}$ is a vector whose components are two random numbers with zero mean and variance 1.

The interparticle repulsion force $\vec{F}_{pp,i}$ is the vector sum of the repulsive forces that act on particle i due to all the other particles. The repulsive force on a particle i due to particle j is modeled using a soft potential $\vec{F}_{ij} = F_{p0}\hat{r}_p/r_p^2$, where r_p is the distance between the particle centers of i and j and $\hat{r}_p$ is the unit vector pointing from j to i. If $r_p > r_c$, then $\vec{F}_{ij} = 0$, where r_c models a finite Debye length [131]. Such a soft potential is typically found in short-range electrostatic repulsion [132]. The value of F_{p0} is $\gamma d_p^2/2$, where γ is the interfacial tension. The characteristic time, force and length scales are t_e, γd_p and R_0, respectively.

The force acting on the particle i from the fluid-fluid interface is

$$\vec{F}_{s,i} = \begin{cases} (F_{s0}/r_s^2)\hat{r}_s, & r_s \le r_{sc} \\ 0, & r_s > r_c, \end{cases} \tag{3.2}$$

where $r_s = R - |\vec{x}_i|$ is the radial distance between the center of the particle i and the drop interface and $\hat{r}_s$ is a unit vector that points from the drop interface to the center of particle i. We used a particle-interface interaction potential analogous to the potential used for inter-particle repulsion. To simulate different particle-interface interaction conditions, we consider the dimensionless parameter F_{s0}/F_{p0}. A value of $F_{s0}/F_{p0} = 0$ simulates a condition in which the colloidal particles do not experience repulsion from the interface. For a value of $F_{s0}/F_{p0} = 1$, the particles are repelled from the interface.

Adsorption occurs when particles come into contact with the fluid-fluid interface, that is, when $r_s \le d_p/2$. Once particles are adsorbed at the interface, their radial position is fixed, making the adsorption irreversible. The adsorbed particles remain mobile in the θ direction due to either Brownian motion or

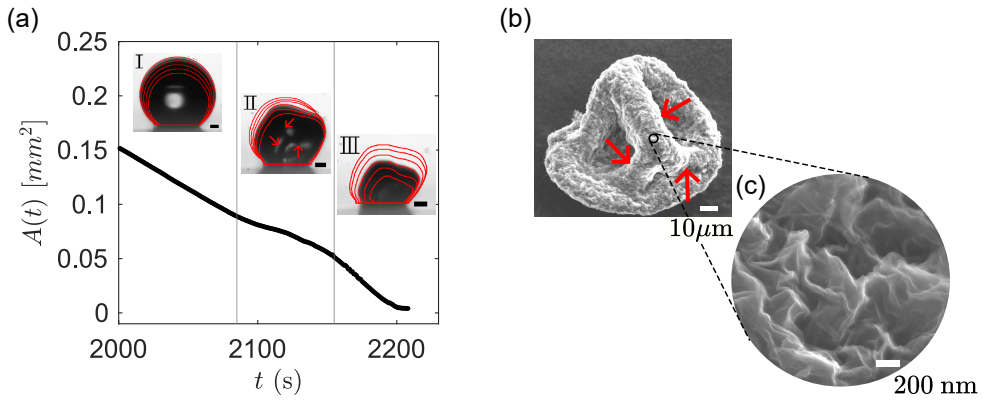

Figure 3.2: a) Time evolution of projected drop area $A(t)$ for $\phi_0 = 5.7 \times 10^{-5}$ and RH = 30%. The insets show the contours of drop edges (red curves) at selected times, superimposed on side view images of the drop. The black scale bars are 50 μm. b) SEM image of the buckled shell. c) SEM image at higher magnification of the buckled shell surface shows nano-scale wrinkles.

inter-particle repulsion. When the particle-interface condition is set to be repulsive, particle adsorption occurs if $(F_{pp,i} + F_{drag}) \geq F_{s,i}$. This condition results in an adsorption barrier at the fluid-fluid interface.
The surface pressure Π is the tension acting in the tangential direction due to the adsorbed particles at the interface and σ is the average tension in the tangential direction due to the particles in the bulk. These tensions are calculated by locally averaging the particle-interface and inter-particle forces per unit area. Appendix G provides more details on the calculation of particle stresses and their validation. The characteristic time, tension and length scales are t_e, γ and R_0, respectively.

3.4 Results and discussion

We start by looking at how the drop shape changes in time. Figure 3.2 shows the time evolution of the drop's projected area for $\phi_0 \approx 5.7 \times 10^{-5}$ and pH ≈ 4. In the same figure we also show contours of the drop edges (red curves) at selected times, superimposed on side images of the drop. From this figure we can identify three characteristic regions. In region I the drop has a nearly spherical shape. Region II begins when the projected drop shape deviates from

a circle, approximately at a buckling onset time $t = t_b \approx 2090$ s. In region II the rate of change of projected area decreases slightly with respect to region I, because the shape perturbations are growing faster than the evaporation induced change in projected area of the spherical drop. In region III the buckled shell shrinks in volume while preserving its overall shape. Looking at Fig. 3.2 b, which shows SEM images of the dried buckled capsule considered in Fig. 3.2 a (the side view of the buckled shell is captured by rotating the sample 35° with respect to the angle of incidence of the electron beam), we can see a correspondence between the folds in Fig. 3.2 b and those in the central panel of Fig. 3.2 a (indicated by red arrows). This comparison confirms that in region III no change in overall shape takes place.
While in region III the overall shape does not change, we hypothesize that compression induces small-scale wrinkles, which are visible in Fig. 3.2 c. From the auto-correlation of the intensity profile of the SEM image in Fig. 3.2 c, we estimate a wrinkle wavelength of roughly 100 nm (see Appendix C), one order of magnitude smaller than each GO sheet's length, and two orders of magnitude larger than each sheet's thickness.

3.4.1 Stage I: Evaporation

The drop projected area in region I decays linearly in time t, following the well-known law which states that for diffusion dominated evaporation of clean drops the square of the drop diameter decreases linearly in time [133]. This is confirmed in Fig. 3.3 a and b, which shows for region I the time evolution of the drop diameter square plotted against normalized time t/t_e, where $t_e = \rho R_0^2/[D(c_s - c_\infty)]$ is the characteristic evaporation time of the water droplet [114]; here ρ is the density of water, c_s is the saturation vapour concentration of water drop and c_∞ is the vapour concentration far away from the drop. Fig. 3.3 a is for fixed RH = 30% and different ϕ_0. Fig. 3.3 b is for different RH and fixed $\phi_0 \approx 5 \times 10^{-5}$. Fig. 3.3 a compares acidic and basic droplets, while Fig. 3.3 b is for acidic droplets. The experiments were performed for initial drop diameter $2R_0 = 1.5 \pm 0.03$ mm. It is seen that the effect of the initial particle volume fraction, RH and pH on the evaporation rate is minimal. In region I, the GO drops evaporate approximately following the same law as pure water drops.
As the GO drops evaporate, the particle concentration increases near the air-water interface, so a change in evaporation rate might be expected if some of the particles are adsorbing at the fluid interface. Recent experiments on tracer diffusion across the interface of emulsion drops covered with a mono-

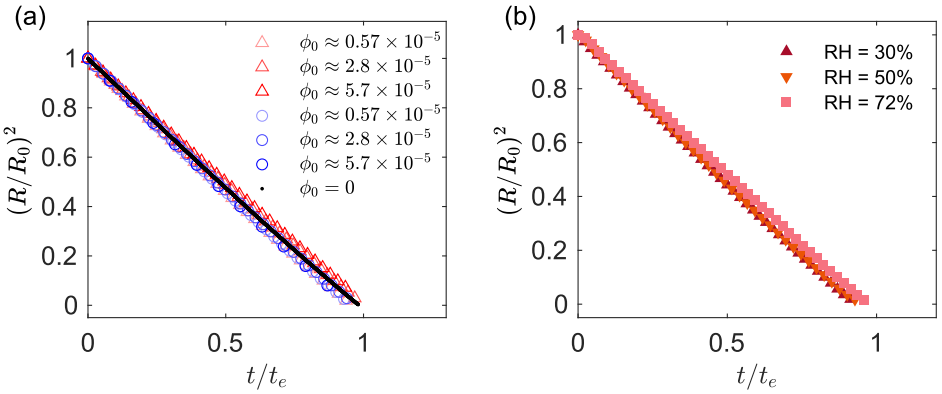

Figure 3.3: a) Ratio $(R/R_0)^2$ vs. t/t_e. The diameters R and R_0 are the current and initial drop radius computed from the projected drop area, respectively ($R = \sqrt{A/\pi}$). Red and blue markers correspond to acidic and basic pH, respectively. b) Ratio $(R/R_0)^2$ vs. t/t_e plotted for different values of relative humidity. The formula used for the time scale t_e is the same for all the data sets presented. The value of t_e depends on the value of RH% for the specific experiment considered.

layer of spherical particles demonstrate that the rate of mass transfer across the interface is unaffected by the presence of the embedded particles [134]. Drop evaporation, drop dissolution and tracer diffusion across an interface are driven, from a continuum perspective, by diffusive processes that depend in an identical manner on the difference between the interfacial concentration and the concentration "at infinity", so similarities between tracer mass transfer at a liquid-liquid interface with spherical particles and evaporation at a water-air interface with sheet-like GO particles may be expected. However, the negligible effect of interfacial particles on the rate of evaporation appears counter-intuitive. After all, if the drop surface was entirely covered with a layer of solid impermeable to diffusion, the evaporation rate would be zero. This apparent paradox can been resolved by analyzing the dependence of the evaporation flux on surface coverage [135–138].

The average diffusive mass flux across the surface of a drop covered with particles is *approximately* the same as the drop surface without particles, provided that i) a sufficient number of exposed patches of fluid interfaces are homogenously distributed on the fluid interface and ii) the size of the exposed patches q is small compared to the drop radius ($q/R \ll 1$). This result is suggested by a mathematical model that considers patches of characteristic size q homogeneously distributed on the surface of the drop. The patches are regions permeable to diffusion on the impermeable layer made by the GO particle assembly (for a GO monolayer, q is a fraction of the particle diameter). On these patches, the vapour concentration is fixed to the saturation concentration c_s. On the impermeable surface of the GO particles, the boundary condition is of homogeneous Neumann type: the gradient of vapour concentration along the normal to the surface is zero. For $t \gg D/R^2$, where R is the radius of the drop, the quasi-steady vapour concentration field around the drop satisfies the Laplace equation, $\nabla^2 C = 0$ [139]. The mass transfer problem of calculating the mass flux out of the droplet, which corresponds to the solution of $\nabla^2 C = 0$ for mixed Neumann-Dirichlet boundary conditions, is mathematically identical to the electrostatic problem of calculating the average electric field on the surface of a dielectric sphere covered with patches held at a fixed electric potential. Asymptotic solutions to the electrostatic problem are available for circular patches located at sufficient distance from each other [140, 141]. The asymptotic expression of Berg & Purcell [142], translated in the language of mass diffusion, gives the following ratio between the mass flux when the

patches permeable to diffusion cover an area fraction α to the maximum flux:

$$\frac{J(\alpha)}{J(\alpha=1)} = \frac{\alpha}{\alpha + kq/R}, \tag{3.3}$$

where $k = \pi/4$. An important insight from this expression is that α does not need to be large for $J(\alpha)$ to be numerically close to $J(\alpha = 1)$. Indeed, as can be seen in Fig. 3.4 for selected small values of q/R, $\frac{J(\alpha)}{J(\alpha=1)}$ grows fast with α. The linear part of the graph, corresponding to the asymptotic limit $\frac{J(\alpha)}{J(\alpha=1)} \simeq \frac{\alpha}{k}(R/q)$, has indeed a large slope, because R/q is much larger than 1 for all practical conditions encountered in our experiment (taking q to be the particle diameter we have q/R of the order of 10^{-3}).

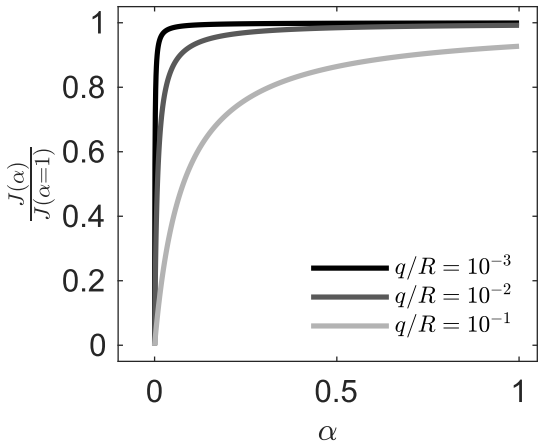

Figure 3.4: Ratio of vapour mass flux of a particle-covered interface to that of a clean interface, from Eqn. 3.3; q is the characteristic size of the exposed patch permeable to diffusion and R is the drop radius.

The condition that the patches are homogeneously distributed is essential. To take a limiting case, if the drop was entirely covered with solid with a single exposed fluid interface patch the mass flux would be drastically reduced, because on most of the drop surface the concentration would be significantly smaller than the saturation concentration.
The trend predicted by Eqn. 3.3 is qualitative similar to the one predicted by the solution via conformal mapping of the 2D Laplace equation for the concentration field in a plane bounded by a periodic flux/no flux line boundary and

a line boundary held at a fixed concentration [137, 143]. These planar models, which have been used to explain evaporation from porous media, also predict a strong dependence on α but unlike Eqn. 3.3 require the prescription of the mass transfer boundary layer thickness. Numerical solutions for diffusion from permeable patches on a sphere have recently become available [141].

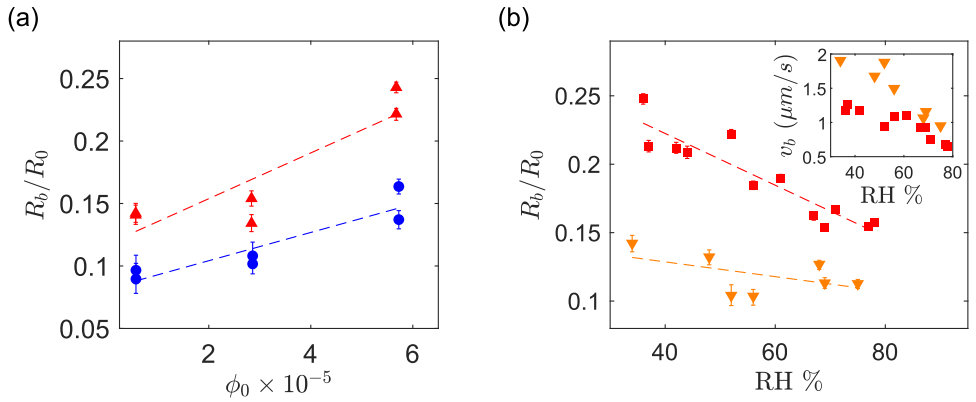

Figure 3.5: a) Normalized buckling radius (R_b/R_0) vs. ϕ_0 for different pH ranges. The red triangle marker (▲) and the blue circle marker (●) correspond to acidic and basic pH, respectively. b) Normalized buckling radius (R_b/R_0) vs. RH for drops with acidic pH. The error bar is calculated at the radius $R(t_b \pm 5\ s)$. The inset shows the velocity of the interface at the onset of buckling v_b vs RH. The red square marker (■) and the yellow triangle marker (▼) correspond to $\phi_0 \approx 5 \times 10^{-5}$ and $\phi_0 \approx 5 \times 10^{-6}$, respectively. The dashed lines serve as a visual guide.

3.4.2 Stage II: Onset of buckling

To characterize the onset of buckling in region II we introduce the buckling radius R_b, defined as the minumum drop radius for which $\zeta > 1$, where $\zeta = P^2/(4\pi A)$ is a circularity parameter, with P and A the projected drop perimeter and area, respectively. Figure 3.5 a shows R_b, normalised by the initial drop radius R_0, versus ϕ_0 for acidic and basic drops. The buckling radius increases with increasing ϕ_0, a trend that can be explained by the earlier formation of a particle shell for higher initial particle concentration [60, 108]. Indeed, the average mass flux of particles towards the fluid interface is approx-

imately $\phi_0 v_i$, so for a given fluid interface velocity v_i the maximum jamming fraction is reached earlier if ϕ_0 is larger. Figure 3.5 b shows R_b/R_0 for a range of relative humidity values for acidic drops with selected particle volume fractions (in this figure R_b is found by measuring the deviation from a circular projected contour, see Appendix D). The inset shows the interface velocity at the onset of buckling v_b. Higher evaporation rate results in higher interfacial velocity and, for a given ϕ_0, earlier particle jamming.

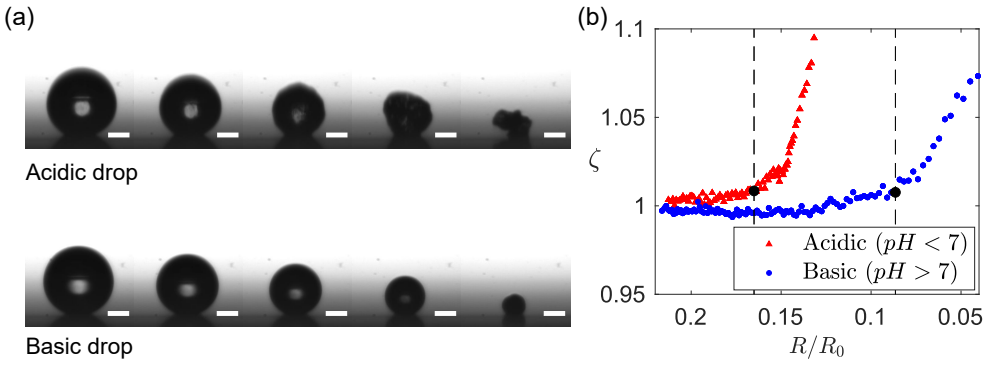

Figure 3.6: a) Time evolution of drop morphology comparing acidic and basic drops. The time increases in steps of 25 seconds. Scales bars represent 100 μm. b) Circularity parameter $\zeta = P^2/(4\pi A)$ vs. normalised radius of the drop. Here P and A are the projected drop perimeter and area, respectively.

Less trivial is the dependence on pH. For any given ϕ_0, acidic drop's R_b is about 1.5 times as large as for the basic drops. In figure 3.5 the acidic and basic suspensions are suspensions at different pH ranges obtained from the same manufacturer. To avoid the possible influence of different compositions in the different samples provided by the supplier, we repeat the experiment of Fig. 3.5 by changing the pH of a suspension of GO from basic to acidic by bubbling CO_2 through the suspension. The CO_2 dissolves in water forming carbonic acid, which yield a pH of approximately 4, as measured by a pH meter. The results are shown in Fig. 3.6 a and b. The experimental condition of temperature, humidity and initial drop size are the same as in Fig. 3.5 with initial particle volume fraction $\phi_0 = 8.5 \times 10^{-6}$. In Fig. 3.6 a we show the time evolution of drop morphology and in Fig. 3.6 b we plot the circularity parameter ζ vs R/R_0 (vertical dashed lines indicate the point of onset of buckling). Fig. 3.6 confirms that the acidic drop deviates from a spherical shape before the basic drop does. The acidic drop buckles at approximately

2 times larger radius compared to the basic drop. Together, Fig. 3.5 and 3.6 provide evidence that the pH has a strong influence on the onset of buckling. A similar observation of pH dependent buckling has been recently reported for dissolving drops with spherical colloidal particles [144].

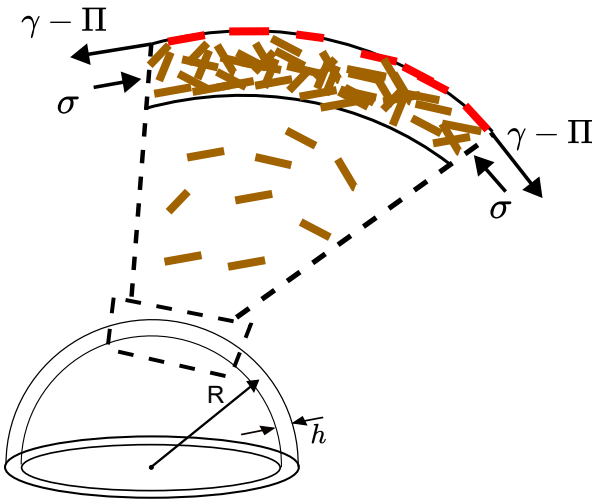

Figure 3.7: Schematic illustrating the two contributions to the tangential stresses: GO particles adsorbed at the liquid-air interface (red) and suspended particles below the liquid-air interface (brown).

To understand the pH dependence of buckling, we describe the particle shell as a particle bilayer (Fig. 3.7) composed of i) the liquid-air interface with partially-wetted particles embedded in it and ii) the dense layer of completely wetted particles in the vicinity of the liquid-air interface. Depending on the pH of the drop the first layer can form or not. Contact between the adsorbed particles yields a surface pressure Π [16,17,28,67,123,145–148]; Π is the lateral (tangential to the drop surface) force per unit length acting on a line element of particle-laden interface and is positive when the embedded particle layer is compressed (provided that the particles touch forming a percolating [148] or packed layer [16,17,67]). On a scale larger than the particles, the macroscopic tension acting *on the fluid interface* with the embedded particles is $\gamma - \Pi$, where γ is the bare air-water interfacial tension. The tension *on the bilayer* must account for the compressive lateral force (per unit thickness) acting on the fully immersed particles (brown particles in Fig. 3.7). Calling σ this tension, the total tension on the bilayer is $\gamma - \Pi - \sigma$.

For the bilayer to buckle, the bilayer needs to be compressed, so $\gamma - \Pi - \sigma \leq 0$. For example, a flat or curved monolayer of particles embedded in a fluid interface with $\sigma = 0$ buckles when $\Pi \simeq \gamma$, as demonstrated in experiments and numerical simulations [16, 17, 67, 123, 146, 148]. The buckling condition $\gamma - \Pi - \sigma \leq 0$ can also be analysed in terms of fluid pressure. If p_i is the water pressure inside the drop and p_o is the air pressure outside the drop, a quasi-static normal force balance on the fluid interface requires [149, 150]

$$p_i - p_o = 2\frac{(\gamma - \Pi - \sigma)}{R}, \tag{3.4}$$

where $R = R_b$. For the drop to buckle there must be a normal force acting on the shell towards the center of the drop. Thus $p_i \leq p_o$, which also gives $\gamma - \Pi - \sigma \leq 0$.

For a particle layer having a finite bending rigidity, one may expect that $\gamma - \Pi - \sigma$ should be sufficiently negative for the particle shell to buckle, so the condition $\gamma - \Pi - \sigma \leq 0$ is approximate. For instance, an Euler beam of Young modulus E, moment of inertia I and length L buckles when the compressive load is larger than $\pi^2 EI/L^2$. For a homogeneous elastic shell, the critical pressure for buckling is of the order of $p_c \approx E(h_b/R_b)^2$ [151, 152]. The maximum pressure from capillary compression is of the order of γ/r_m, where r_m is the characteristic radius of curvature of the small menisci between the interfacial particles [60, 146]. Taking r_m to be of order of particle size ℓ, we get $\gamma/r_m \sim 10^5$ Pa, while p_c is in the range $70 - 2200$ Pa (we take $E \approx (\phi_{shell} - 0.002)^{2.7}$ GPa [125] and use the values of h/R measured in Sec. III C). We can thus safely neglect the influence of the bending rigidity and consider the condition $\gamma - \Pi - \sigma \leq 0$ a reasonable approximation.

Given that γ is independent of pH [153], a dependence on the buckling threshold on pH can be explained if either Π or σ depend on pH. As mentioned in the introduction, there is ample of evidence in the literature that for GO the main effect of pH is to change Π. Uniaxial compression experiments in a Langmuir trough with an air-water interface populated with a monolayer of GO particles show that the propensity of the GO particles to adhere to the fluid interface is strongly pH dependent [66]. These experiments show that for acidic solutions (pH = 5.5) the GO particles are adhered to the air-water interface and the monolayer buckles upon compression when $\Pi \approx \gamma$ [26, 66]. For a basic solutions at pH = 10.5, the GO sheets instead desorb from the fluid interface already at $\Pi \approx 2.5$ mN/m. Molecular dynamics simulations show that in an acidic environment the GO particles are attracted to the liquid-air interface while they are repelled from the interface for basic pH [23].

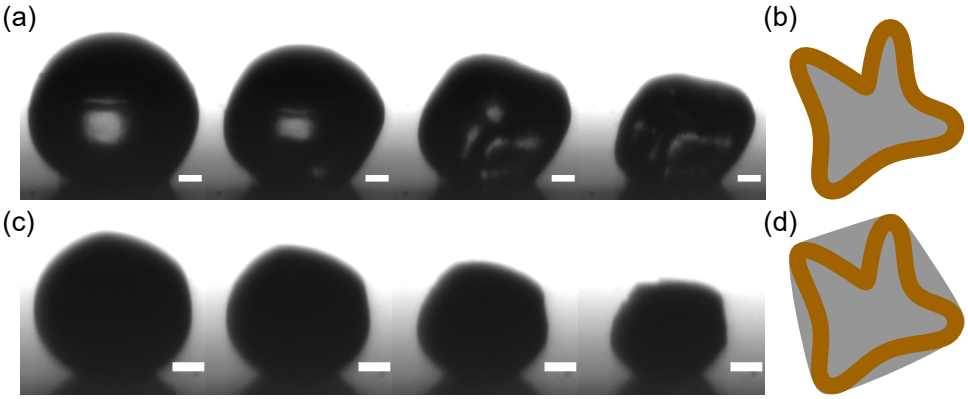

Figure 3.8: Difference in post-buckling morphology between acidic (a) and basic (c) drops for $\phi_0 \approx 5.7 \times 10^{-5}$. Concave depressions are observed on the interface of acidic drops, while basic drops exhibit convex interface shapes (better seen in the supplementary movie M1). The time increases in steps of 25 s for acidic drops and 10 s for basic drops. Scale bars represent 50 μm. The schematics on the right illustrate the difference in interface shape when the particle are adsorbed at the fluid interface (b) or detached from it (d).

The hypothesis that changes in pH mainly changes Π is also supported by the fact that ignoring the effect of pH on Π would give a purely convex shape of the fluid interface, as illustrated in the schematic in Fig. 3.8 d, because the absence of adsorbed particles means that the particles can only push outwards on the interface, but not pull inwards. Yet the experimental images clearly show inward indentations of the water-air interface for acidic drops (see Fig. 3.8 a). It may be possible that the contrast of the images for basic drops in Fig. 3.8 b is not sufficient to detect concave depressions. We performed experiments with basic drops at higher concentrations $\phi_0 \approx 28 \times 10^{-5}$. Since buckling starts earlier for increased ϕ_0, a better contrast is obtained for this set of experiments. The supplementary movie (M1) shows the evaporation of this drop at RH = 30%. The drop has a convex non-spherical shape after the onset of buckling, as suggested in the illustration of Fig. 3.8 d.

3.4.3 Post buckling morphology (after stage III)

We now study the effect of relative humidity and initial particle concentration on the post-buckling morphology of GO drops with acidic pH and initial di-

ameter $2R_0 = 1.65 \pm 0.05$mm. Figure 3.9 a shows SEM images of the dried capsules of acidic drops for a range of values of relative humidity and initial concentrations. For the lowest concentration $\phi_0 \approx 5 \times 10^{-6}$, buckling leads to highly convoluted folds, while for the highest concentration buckling does not occur. The absence of buckling at $\phi_0 \approx 2.5 \times 10^{-4}$ suggests the formation of a relatively thick shell. Our observations indicate that for this concentration the drop essentially skips stage Ⅱ and enters directly stage Ⅲ where the nearly spherical shell shrinks in volume maintaining a constant shape (see supplementary movie M2 corresponding to $\phi_0 \approx 2.5 \times 10^{-4}$ and $RH = 32\%$). We could only detect small deviations from a perfectly spherical shape at $R/R_0 \approx 0.34$. At this radius, the interface velocity is $v_i = 0.43$ μm/s, which gives a particle Péclet number $v_i \ell / D_p \approx 0.7$. For Péclet number smaller than 1 diffusion could lead to a porous shell of thickness larger than what could be estimated by Eqn. 3.5, which is a good approximation only for large Pe. A thick porous shell, formed as a result of the particles assembling into a percolating network, could deform isotropically rather than buckle.

For intermediate values of ϕ_0, we observe a clear correlation between the number of folds in the buckled shape and the value of RH (Fig. 3.9 b). The mode number n was taken as the number of concave depressions observed in the SEM images of buckled capsules. Faster evaporation leads to higher buckling modes. A similar trend and identical buckled shapes have also been reported for evaporating drops laden with spherical colloids [61].

The observation of reproducible buckled shapes at intermediate ϕ_0 is in sharp contrast to the buckling of elastic shells in Refs. [151, 152, 154–158] which is known to be sensitive to defects. The repeatable shapes of Fig. 3.9 b suggest a shell with small imperfections of negligible influence. Recent studies on the role of imperfections in shell buckling report that the smaller the ratio of the imperfection's characteristic size to the shell thickness, the closer the shell is to being a perfectly homogeneous [157, 158].

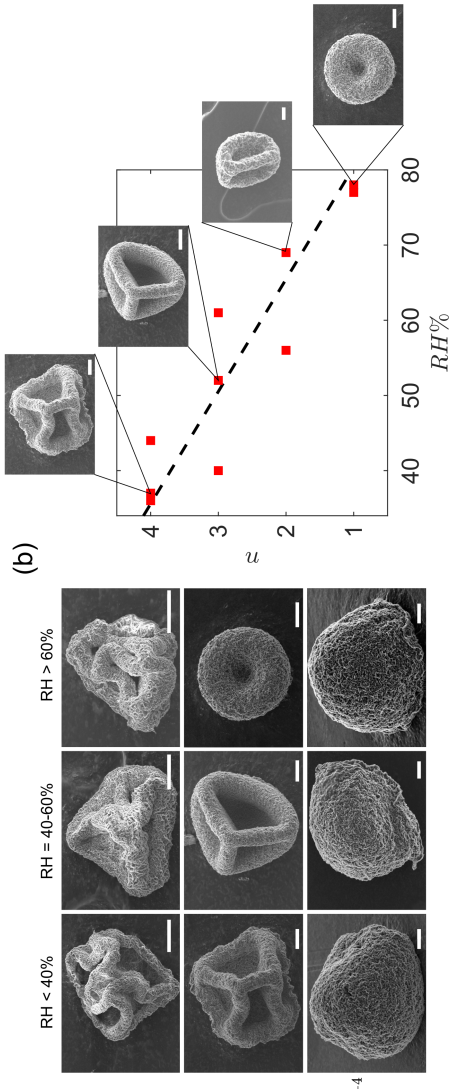

Figure 3.9: a) Scanning electron microscope (SEM) images of dried capsules for selected initial concentrations and relative humidity values. b) Buckling mode number vs. relative humidity for $\phi_0 \approx 5 \times 10^{-5}$. Insets show corresponding SEM images of the buckled capsule. All the scale bars represent 20 μm. Black dashed line serves as a visual guide. All experiments here correspond to GO drops with acidic pH.

The mode number dependence on the evaporation rate (Fig. 3.9 b) could be explained by geometric arguments from perfect shell theory [152] or by the inertia of the shell [159,160]. To rule out the second, less plausible hypothesis, knowledge of the thickness of the shell is necessary. Direct measurement of the thickness of the shell in an evaporating drop is challenging, unless sophisticated experimental techniques are used [62,124]. We estimated the shell thickness by measuring the evaporation of GO suspensions from the tip of a capillary tube placed in a humidity controlled chamber [161–163]. The water evaporates from the open end of the capillary tube, resulting in the accumulation of the GO particles at the air-water interface and the formation of a planar particle layer. The solid fraction in the layer can be calculated as $\phi_s \approx (v_c/v_{shell})\phi_0$ [58], where v_c is the rate of change of height of the liquid column in the capillary (due to evaporation) and v_{shell} is the rate of change of thickness of the particle layer. Detailed explanation of the experiments are found in the Appendix E. The measured solid fraction was $\phi_{shell} = 0.018 \pm 0.004$ for the same initial solid fraction and similar range of particle Pe numbers as in the drop experiments of Fig. 3.9 b. The ratio of shell thickness to radius at the onset of buckling can be estimated from mass conservation of the particulate phase [60]:

$$\frac{h_b}{R_b} = 1 - \left[\frac{(\phi_{shell} - \phi_0(R_0/R_b)^3)}{(\phi_{shell} - \phi_0)}\right]^{1/3} \tag{3.5}$$

According to this expression, h_b/R_b decreases with increasing R_b/R_0. Because our experimental data shows that R_b/R_0 increases with decreasing RH (Fig. 3.5), faster evaporation will be associated to smaller values of h_b/R_b. Using the measured values of R_0/R_b and ϕ_{shell}, h_b/R_b is estimated to be in the range $0.06 - 0.34$, where 0.06 and 0.34 correspond to the smallest and largest values of RH. Thus, the humidity level has a direct effect on the slenderness of the shell at buckling.

The ratio of the kinetic energy of the shell to the bending energy ($B \sim Eh_b^3$) of the shell is of the order of $\rho_{shell} R_b^2 h_b v_b^2/B$. For buckled GO capsules in Fig. 3.9, this ratio is in the range 10^{-14} to 10^{-10}. Since $\rho_{shell} R_b^2 h_b v_b^2/B \ll 1$, the role of inertia can be safely neglected.

For inertia-less, homogeneous, linear elastic shells, the mode number n is obtained by the minimization of elastic bending and stretching energy contributions [24, 151]. For a perturbation of amplitude w and characteristic wavelength λ, the bending energy per unit area is $Eh^3(w/\lambda^2)^2$, where w/λ^2 is an estimate of the local curvature. The perturbation also results in an in-plane strain w/R and the corresponding stretching energy per unit area is

$Eh(w/R)^2$. Balancing the two energies gives a prediction for the mode number $n \propto R/\lambda \approx (R/h)^{1/2}$. For a constant shell radius, increasing the shell thickness increases the bending energy contribution: it is energetically favourable to select large wavelengths (small mode numbers) as this minimizes the bending energy. For inertia-less, homogeneous, linear elastic spherical the mode number is predicted to satisfy [152]

$$n(n+1) = [12(1-\nu^2)]^{1/2}(R_b/h_b) \tag{3.6}$$

The underlying theory holds for large values of the Föppl-von Kármán number $\kappa = EhR^2/B$ [151,164]; in our case κ is in the range 76−2200 for $\phi_0 \approx 5\times10^{-5}$. Figure 3.10 shows n vs. $(R_b/h_b)^{1/2}$ for $\phi_0 \approx 5 \times 10^{-5}$. The black curve is the theoretical prediction $n(n+1) = [12(1-\nu^2)]^{1/2}(R/h)_b$ [152], where $[12(1-\nu^2)]^{1/2} = 3$ with $\nu \approx 0.5$ (ν is usually taken to be of order 1 [125]). It is seen that the prediction follows the experimental trend, but is shifted by approximately 1. The prediction does not account for the fact that contact with the substrate reduces the number of concavities. Shifting the the mode number prediction by one to account for this effect (black dashed line) improves prediction of the experimental data.

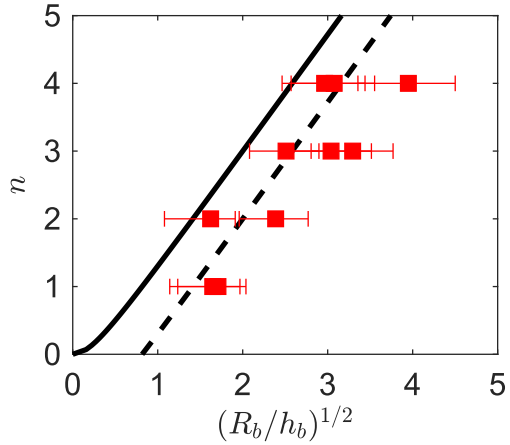

Figure 3.10: Buckling mode number n vs. $(R_b/h_b)^{1/2}$ for $\phi_0 \approx 5 \times 10^{-5}$. The black curve corresponds to Eqn. 3.6. The black dashed line is $n-1$.

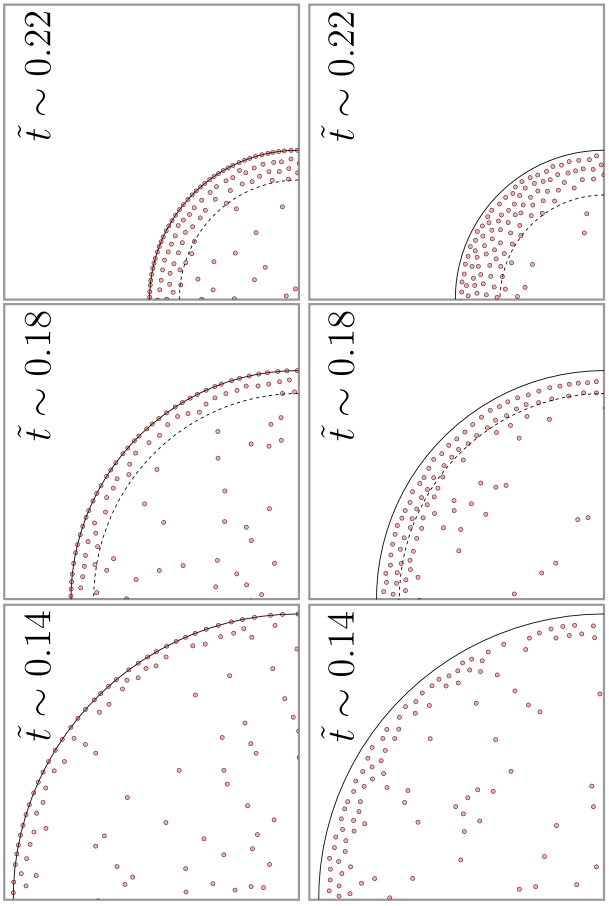

Figure 3.11: Particle distribution in evaporating drops. Sub figures a and b correspond to drops with non-repulsive ($F_{s0}/F_{p0} = 0$) and repulsive ($F_{s0}/F_{p0} = 1$) particle-interface interaction conditions, respectively. The $Pe \approx 93$ and $\phi_0 = 0.01$ for both a and b. The normalized time is $\tilde{t} = t/t_e$.

3.4.4 Simulation results

Figures 3.11 a and b show the time evolution of the particle distribution in an evaporating drop with non-repulsive ($F_{s0}/F_{p0} = 0$) and repulsive ($F_{s0}/F_{p0} = 1$) particle-interface interaction conditions, respectively. Here $Pe \approx 93$ and $\phi_0 = 0.01$ for both cases. Sub figure a shows particles irreversibly attached to the interface during the drop evolution, while sub figure b shows that repulsion between particle and interface results in no interfacial particle adsorption. Nevertheless, a dense particle layer forms near the retracting liquid-gas interface for both particle-interface interaction conditions, as indicated by black dashed lines in Fig. 3.11.

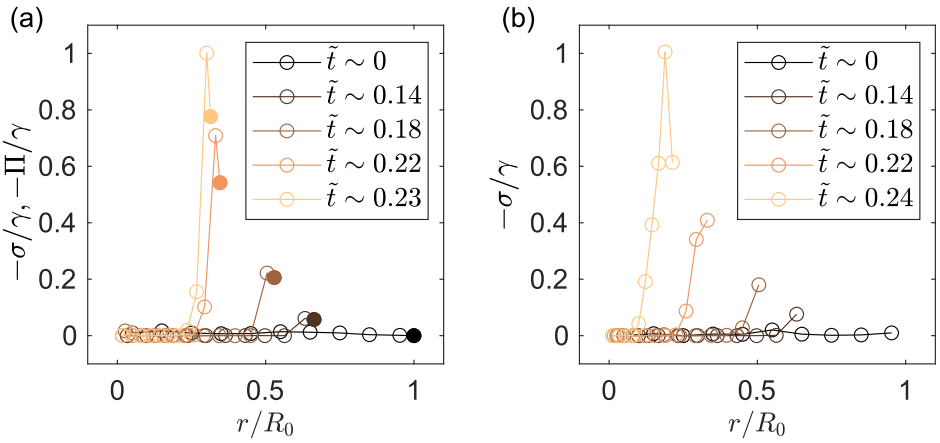

Figure 3.12: Time evolution of normalized particle tension and surface pressure $-\sigma/\gamma, -\Pi/\gamma$ vs. normalized radius r/R_0 in evaporating drops. Sub figures a and b correspond to drops with non repulsive ($F_{s0}/F_{p0} = 0$) and repulsive ($F_{s0}/F_{p0} = 1$) particle-interface interaction conditions, respectively. The open and filled circles correspond to $-\sigma/\gamma$ and $-\Pi/\gamma$, respectively.

Figure 3.12 shows the time evolution of normalized particle tension and surface pressure $-\sigma/\gamma, -\Pi/\gamma$ as a function of normalized radius r/R_0 for the same cases discussed in Fig. 3.11. Here, $r \in (0, R)$ represents the radial distance inside the drop. Sub figures a and b correspond to non-repulsive and repulsive particle-interface interaction conditions, respectively. We assume that buckling occurs when the particle tension or the surface pressure becomes equal to γ. The instant of time when $max(|\Pi, \sigma|)/\gamma \approx 1$ is satisfied is chosen as the buckling time t_b and the corresponding drop radius R_b (see Sect. 3.4.2). In

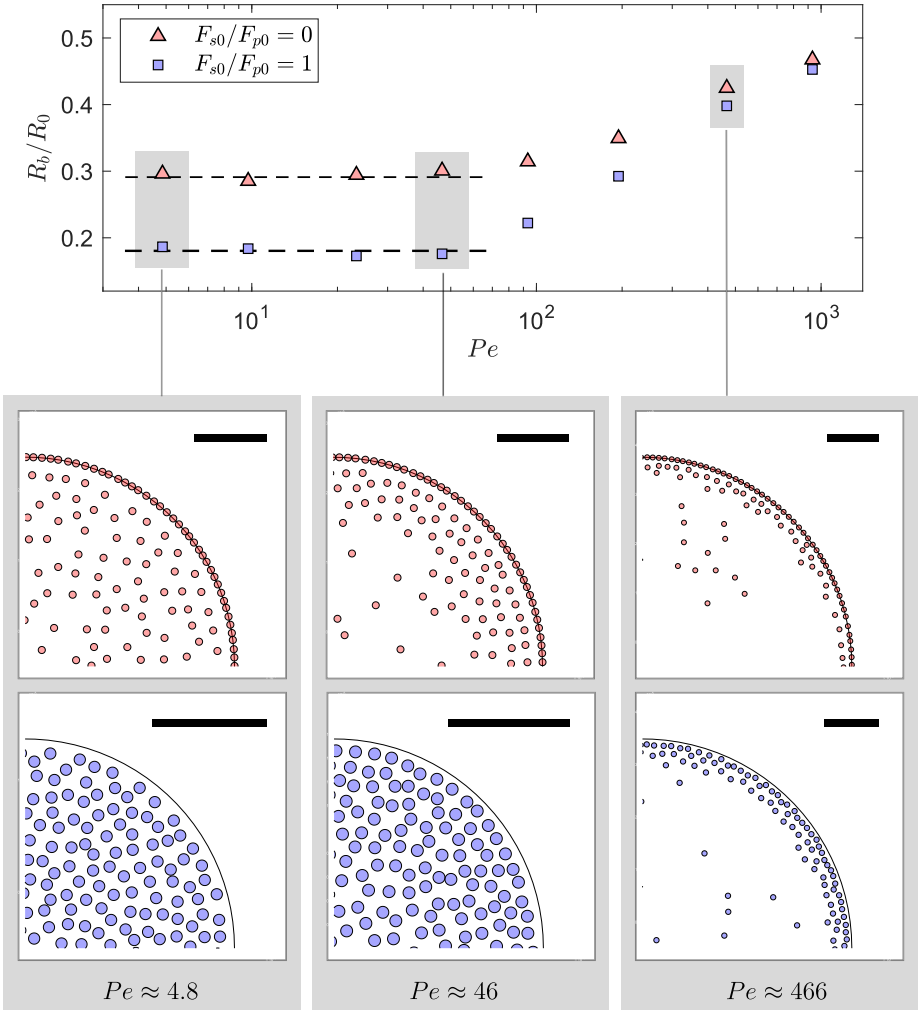

Figure 3.13: Normalized buckling radius R_b/R_0 vs. Pe. The red triangle markers corresponds to no repulsion between particle and interface ($F_{s0}/F_{p0} = 0$) and the blue square markers corresponds to repulsion between particle and interface ($F_{s0}/F_{p0} = 1$). The particle distribution at R_b/R_0 are shown for $Pe \approx 4.8, 46$ & 466 in the bottom panel. The initial drop radius $R_0 = 100d_p$ and the initial solid fraction $\phi_0 \approx 0.01$ is the same for all data presented. The scale bars correspond to $10d_p$.

our simulations, the term 'buckling' refers only to satisfying the above criterion. However, for buckling to occur, another criterion must be met: the shell thickness h_b must be significantly smaller than R_b.

It can be seen that the drop buckles earlier at $\tilde{t} \approx 0.23$ when the particles adsorb at the interface (Fig. 3.12 a) compared to the case when particles do not adsorb at the interface, $\tilde{t} \approx 0.24$ (Fig. 3.12 b). The earlier buckling is further explored in Fig. 3.13 which shows the normalized drop radius R_b/R_0 vs. Pe for two particle-interface adsorption conditions. The red triangle and blue square markers correspond to non-repulsive ($F_{s0}/F_{p0} = 0$) and repulsive ($F_{s0}/F_{p0} = 1$) particle-interface conditions, respectively. We observe that the drops with interface adsorbing particles always buckle earlier than the drops with hydrophilic particles for all Pe numbers. For $Pe \geq 10^2$, R_b/R_0 increases with Pe whereas, for $Pe < 10^2$, R_b/R_0 plateaus. This plateauing behavior that has not been reported so far.

We first focus on $Pe \geq 10^2$. For large Pe numbers, the diffusive flux away from the interface is very small compared to the convective mass flux towards the interface $\propto v_i\phi_0$. Thus larger v_i leads to earlier buckling of the drop with larger R_b. This explains the trend of increasing R_b/R_0 with respect to Pe. For either of the particle-interface interaction conditions, the convective flux remains the same whereas the diffusive flux depends on the particle adsorption to the interface. In case of particles repelled from the interface, the diffusive flux is small but finite. For interface adsorbing particles, the diffusive flux away from the interface is zero, since the particles are irreversibly adsorbed at the interface. The irreversible particle adsorption at the interface leads to earlier jamming and thus earlier buckling of drops with particles adsorbed at the interface.

For $Pe < 10^2$, the value of R_b/R_0 plateaus for both particles-interface adsorption conditions, albeit at different values. In the case of no particles adsorption, R_b/R_0 reaches a plateau at ≈ 0.2 which corresponds to a homogeneous dense packing of particles (see bottom panel corresponding to $Pe \approx 4.8$ & 46). Thus for $Pe < 10^2$ and no particles adsorption, buckling cannot occur. In case of particles adsorbed at the interface buckling occurs due to the formation of a shell layer composed of a monolayer of particles at the interface. The insets in Fig. 3.13 corresponding to $Pe \approx 4.8$ and 46 show the jamming of monolayer of particles at the interface for adsorbing particles, while no buckling occurs for the same Pe numbers in the case of non-adsorbing particles.

The specific value of $R_b/R_0 \approx 0.3$ is understood by analyzing the rate of particle adsorption to the interface. Figure 3.14 shows the number of parti-

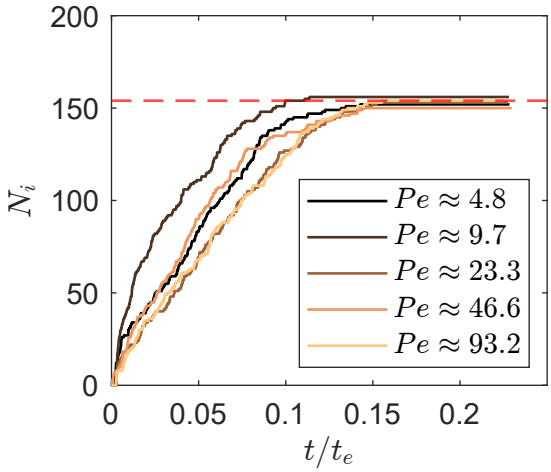

Figure 3.14: The number of particles at the interface as a function of normalized time for different values of $Pe < 100$. The red dashed line is $N_{eq} = 154$.

cles at the interface N_i as a function of normalized time t/t_e for $Pe < 10^2$. It can be seen that for time $t/t_e > 0.15$, the number of particles in the interface reaches a constant value $N_{eq} \approx 154$ (indicated by red dashed line). The rate of adsorption becomes zero because the particles already adsorbed at the interface repel other particles near the fluid-fluid interface, effectively changing the particle-interface interaction into a repulsive one. As the drop continues to evaporate, N_{eq} remains constant but the surface fraction increases leading to jamming at the interface. The buckling radius can be calculated as $2\pi R_b \phi_j = 154 d_p$, where $\phi_s \approx 0.8$ is the surface fraction at R_b (obtained from the simulation). Substituting the initial condition $R_0 = 100 d_p$, we get $R_b/R_0 = 154/(2\pi 100 \phi_s) = 0.3$. This is close to the plateau value $R_b/R_0 \approx 0.3$ seen in Fig. 3.13 for non repulsive particle-interface condition indicated by red triangle markers.

The hypothesis for onset of buckling of drops requires a large Pe number, resulting in the formation of a shell layer that undergoes buckling [60]. However, we have shown that drops with small Pe numbers can also undergo buckling due to the formation of a shell composed of a monolayer of particles at the interface (see Fig. 3.13). Thus, for small Pe numbers, the onset of buckling is decided solely based on particle adsorption to the interface and the necessary criterion for onset of instability is $(\gamma - \Pi) = 0$. The effect of bulk stresses can be neglected.

3.4.5 Stability of buckled capsules in water

Figure 3.15 a and b show the morphology of the dried capsules from drop evaporation experiments of acidic and basic drops for $\phi_0 \approx 5.7 \times 10^{-5}$. Each dried capsule is first re-suspended in water and then drop casted onto a carbon tape for SEM imaging. The buckled capsule of the acidic drop retains its buckled morphology upon contact with water, while the capsule from the basic drops partially unfolds. A possible explanation is that the thicker shell of basic droplets undergoes a smaller in-plane compression in region III, $A/A_{dry} \approx 3$ as opposed to $A/A_{dry} \geq 10$ for acidic drops. The stability of buckled capsule of graphene oxide re-suspended in water is attributed to the formation of permanent bonds due to plastic deformation of the sheets [45]. The weaker compaction of basic droplets may not result in the formation of such permanent bonds, so unfolding for basic droplets is more likely.
As an illustration of the practical implications of this observation, powders obtained by spray drying acidic and basic GO suspensions ($\phi_0 \approx 2 \times 10^{-3}$) in a lab scale spray dryer are collected and re-suspended in water (see Appendix F for experimental details). The suspension is then drop casted onto a polished copper tape and imaged by SEM (figures 3.15 c and d). Figure 3.15 c shows a few buckled capsules (red circles) and some unfolded capsules (red arrows). Figure 3.15 d entirely has only flat sheets with some folds, indicating that all buckled capsules have unfolded. Of course conditions in a spray drier are much more complicated than in our single-drop experiments, but the simple test of figures 3.15 c and d illustrates that the pH of the solution has a drastic effect on the ability of GO capsules, produced by spray-drying, to maintain their shape when redispersed in water.

3.5 Conclusions

We investigated experimentally the evaporation of water drops containing graphene oxide nanosheets. Single drops are placed on a superhydrophobic surface and are observed from the side by a camera and the buckled capsules imaged by SEM. Different stages of evaporation are identified, and the effect of solid concentration, pH and relative humidity assessed. Evaporation gives rise to a particle-rich shell that buckles, forming folded structures. For certain ranges of particle concentration and relative humidity the folded structures display distinct buckling modes (Fig. 3.9).
Before buckling, when the drop has a nearly spherical shape, the rate of decrease of drop volume is found to be independent of the initial particle con-

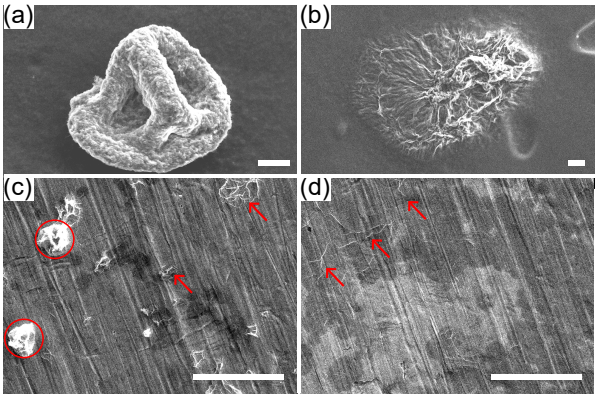

Figure 3.15: Comparison of dried buckled capsules from single evaporating drops (top panels) and from spray dried drops (bottom panels) after resuspension in water. Top: SEM images of capsules from acidic (a) and basic (b) drops from experiments on super-hydrophobic substrates. The buckled capsules are re-suspended in water and drop casted onto carbon tapes. Bottom: SEM images of spray-dried GO powders from acidic (c) and basic drops (d). The powders are re-suspended in water and drop casted onto polished copper tapes. Scale bars represent 20 μm.

centration. A theoretical model based on Berg & Purcell's [142] asymptotic solution for a sphere covered with a uniform distribution of patches permeable to the evaporation flux is used to demonstrate that even in the presence of GO particles adsorbed on the fluid interface, the evaporation flux across the particle-laden and clean drop surface are almost identical.

The initial particle concentration and pH have a marked effect on the drop radius at which buckling occurs. Buckling of basic droplets (pH>7) occurs later, for a given particle concentration, than buckling of acidic drops. Dried capsules formed from acidic drops do not unfold when resuspended in water, unlike capsules from basic drops. There is therefore a link between time of buckling and mechanical stability in water of the produced capsules.

The simulations of drops with repulsive and non-repulsive particle-interface conditions reveal a non-linear dependence of buckling radius on the Péclet number. We showed that when particles adsorb at the fluid-fluid interface, buckling occurs regardless of the Péclet number. These results highlight the crucial role of particle adsorption on the onset of buckling.

The observation of the shape of the fluid interface post buckling seem to suggest that the pH dependent adsorption of GO particles to the air-water interface plays an important role in, and possibly controls, the onset of buckling. Our interpretation of the condition for the onset of buckling, based on particle adsorption, is different from the one assumed by many published models for spherical colloids, which consider only the particles completely immersed in the fluid as responsible for buckling [60, 62].

For a range of intermediate concentrations and relative humidities, very controlled buckled structures could be obtained. Analysis of the surface modes of these structures indicate that the particle shell buckles essentially like a inertialess deflated elastic shell. What is remarkable is the repeatability with which these shapes are obtained in our experiments. The shape of deflated elastic shells is notoriously dependent on the presence of defects. In our experiments, non-homogeneities in the particle distribution, if present, do not seem to affect the overall shape of the capsules.

We report an increase in mode number (number of depressions) for increasing evaporation rate, see Fig. 3.9 b. This trend can be explained by the dependence of the mode number n on the slenderness of the shell at buckling, as measured by h_b/R_b. The mode number increases with R_b/h_b, approximately as $\sim (R_b/h_b)^{1/2}$ (Eqn. 3.6), and R_b/h_b in turn depends on the humidity level, as demonstrated by the data in Fig. 3.5.

Spray drying of acidic drops may be useful to obtain stable suspensions of

GO capsules, as we demonstrate in Fig. 3.15 . The emergence of hierarchical folds due to buckling - we report undulations ~ 100 μm accompanied by small scale undulations of the order of 100 nm - could be exploited, for example, to produce hierarchical particulate materials [41, 165].

3.6 Appendix

Appendix A: Drop contact angle during evaporation

The time evolution of the contact angle of a dilute ($\phi_0 \approx 0.57 \times 10^{-5}$) GO drop during evaporation is shown in figure 3.16. The contact angle is approximately 155° for most of the drop evaporation time, implying evaporation in a constant contact angle mode.

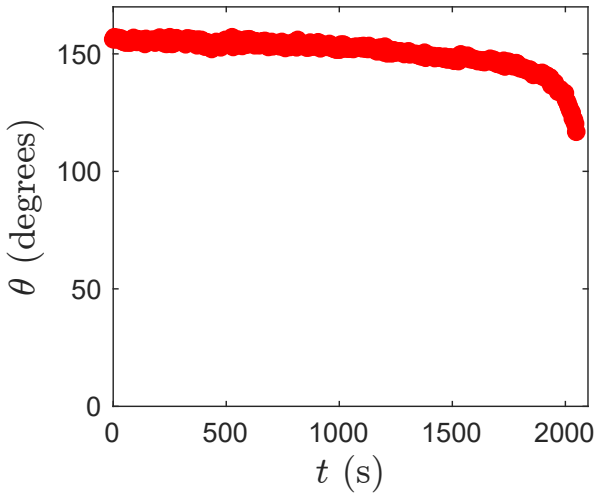

Figure 3.16: Time evolution of contact angle of a GO drop during evaporation.

Appendix B: GO sheet length and thickness estimation

To estimate the GO thickness we used atomic force microscopy (AFM). A GO suspension with initial particle concentration $\phi_0 \approx 5 \times 10^{-7}$ is drop casted onto a silicon wafer with a 300 nm coating of SiO_2 (PI-KEM). Prior to drop casting the silicon wafer is cleaned with acetone, IPA, ethanol and subject to sonication in an ultrasonic bath with Milli-Q water. A region of 20×20 $(\mu m)^2$ is imaged in the AFM using tapping mode. The data is processed with the

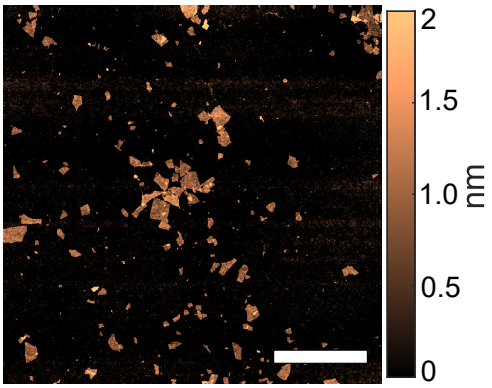

Figure 3.17: AFM image of the GO sheets drop casted on silicon wafer. The color map corresponds to the height data. The white scale bar represents 5 μm.

open-source software Gwyddion to obtain the height map shown in Fig. 3.17. The thickness statistics are obtained by a in-house developed MATLAB code. The measured average sheet thickness is $t = 1.00 \pm 0.14$ nm. The lateral sizes were measured using scanning electron microscopy images of the same silicon wafer. The average sheet length is $\ell = 1.08 \pm 0.44$ μm.

Appendix C: Wavelength of small scale wrinkles

To estimate the wavelength of small scale wrinkles in the SEM image of the buckled aggregate in Fig. 2 c, we compute the auto-correlation of the intensity profile. The intensity autocorrelation can be an approximation of the height-height correlation of the small scale wrinkles in the buckled capsule. The average autocorrelation function becomes zero approximately for $\tilde{x} \simeq 100\ nm$. We take this to be the typical wavelength of the small scale wrinkles.

Appendix D: Radius at the onset of buckling

In Fig. 5 (a) in the main text, the radius at the onset of buckling is found by measuring the deviation of the projected contour of the drop from a circle by using a circularity parameter ζ. In Fig. 5 (b) we introduce a new parameter Φ, the difference in circumference of a fitted ellipse to the drop contour and the measured circumference of the drop contour from the image of the drop. Figure 3.19 shows Φ vs. time (in seconds) for a typical GO drop during evaporation. As the drop undergoes buckling there is a sharp increase in Φ

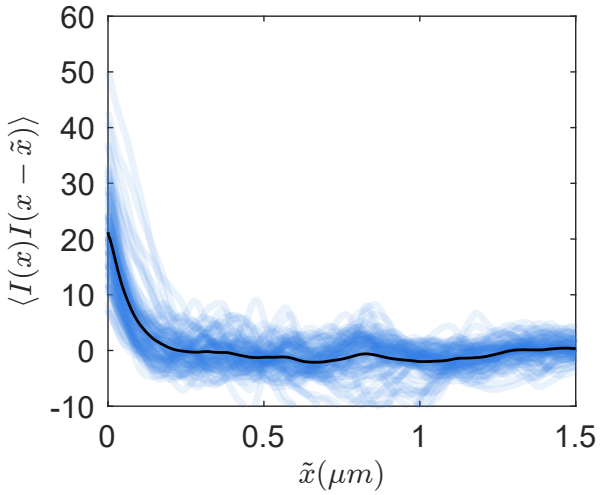

Figure 3.18: Autocorrelation function of the intensity profile from the SEM image of Fig. 2 c. The blue curves indicate the autocorrelation function along each row of pixels and the black curve represents the average over all rows.

which we identify as the onset of buckling time t_b and the corresponding radius R_b.

Appendix E: Capillary evaporation experiments

Figure 3.20 a shows the schematic of the experimental setup (not to scale) to measure the shell volume fraction. A glass capillary tube with internal diameter 0.4 mm is held perpendicular to gravity, with its open end exposed to a humidity controlled chamber. The other end of the tube is attached to a water reservoir to maintain a constant pressure head [162]. The open end of the capillary tube is filled with the GO suspension and the evaporating GO suspension is separated from the water in the reservoir by an air bubble that is trapped between them. The air bubble saturated with water vapour ensures that the GO suspension evaporates only from the open end of the capillary tube.

The height of water in the reservoir remains unchanged during evaporation, as the reservoir diameter is much larger than diameter of capillary tube, maintaining a constant pressure $P_A > P_{atm}$ between the reservoir and the open end of the capillary tube. The higher pressure (P_A) prevents the GO suspension from retracting into the capillary tube from the open end during evaporation

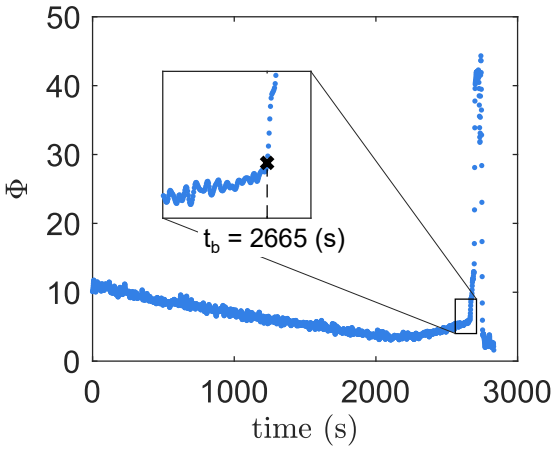

Figure 3.19: Difference (Φ) between the circumference of a fitted ellipse and the circumference measured from the side view image of the drop. Inset shows a sharp increase in Φ for time $t = t_b \approx 2665\ s$.

(see Fig. 3.20 b, where the system is imaged by a camera with a large field of view). The higher pressure also renders the liquid-air interface, at the open end of the capillary, planar. Another camera with zoom lens records the open end of the capillary to visualize the growth of the particle dense layer (see Fig. 3.20 c). Since the capillary tube is held horizontal, the shell formation is not affected by sedimentation. Both the camera are synchronized to capture images at the same instance at 0.05 fps.
The height of the liquid column in the capillary can be found by balancing the mass loss and the evaporation flux. The height of the liquid column H is [163]

$$H(t) = H_0 - \frac{4D(c_s - c_\infty)t}{\pi \rho_\ell r_i} \tag{3.7}$$

Here ρ_ℓ is the liquid density, H_0 is the initial height of the liquid column, c_s is the saturation vapour concentration, c_∞ is the vapour concentration far away from the open end of the capillary and r_i is the internal radius of the capillary. Figure 3.21 shows the normalized liquid column height as a function of time for GO suspension with initial concentration $\phi_0 \approx 5.7 \times 10^{-5}$. The experiments are performed with initial height $H_0 \approx 40$ mm and RH = 32 and 60%. The dashed lines are theoretical predictions from Eqn. 3.7. It can be seen that the experimental data agree well with the linear trend predicted by Eqn. 3.7

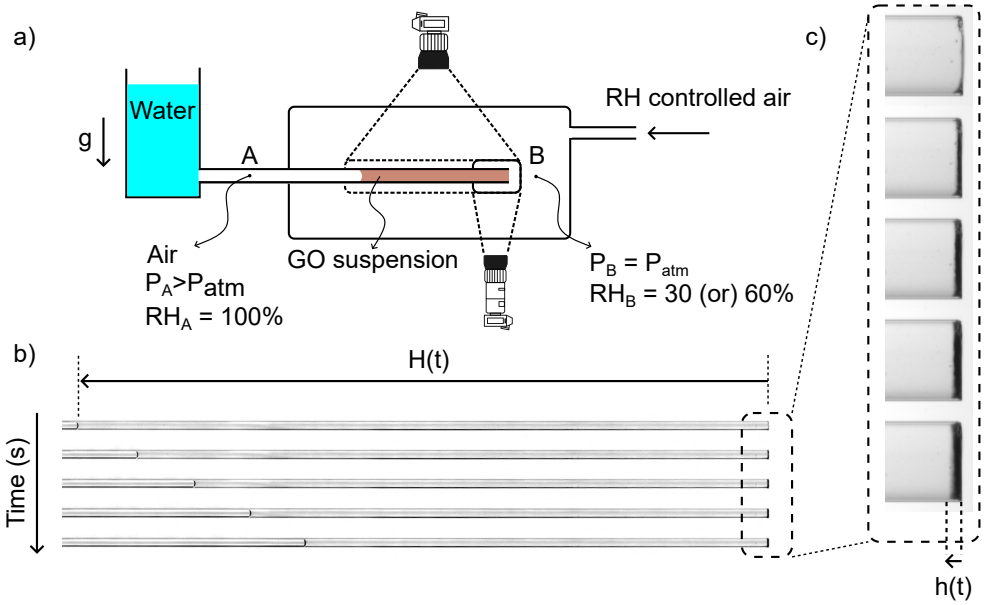

Figure 3.20: a) Schematic of the setup for studying the evaporation of GO suspension from a capillary tube. b) Images from the camera with a large field of view shows the height $H(t)$ of the liquid column of the GO suspension. c) Images from the camera with a zoom lens show the shell layer height $h(t)$.

until $t \approx 6000$ s and $t \approx 15000$ s for $RH = 32$ and 60%, respectively. A slowing down of the evaporation rate occurs for longer times. Possible causes of deviation from Eqn. 3.7 are the recession of the fluid interface into the dense particle layer or the dependence of pressure on the microscopic meniscus curvature [166]. From Fig. 3.21 we calculate the rate of change of height of the liquid column $v_c = 2, 1.26$ μm/s corresponding to RH $= 30, 60\%$, respectively. To quantify the thickness of the dense particle layer, we use the image data from the camera with a zoom lens (see Fig. 3.20 c). Figure 3.22 a shows the open end of the capillary tube with a dense particle layer. The region where the light intensity is measured indicated by a green box which is located just above the tip of the capillary tube. The intensity is averaged in the y direction and plotted as a function of x distance in Fig. 3.22 b. The intensity value changes from approximately 50 to 200, corresponding to the transition from the dense particle layer to the dilute GO suspension. The intensity curves have a sigmoidal shape and it translates in the x direction as time progresses. By finding the displacement of the sigmoid with respect to time we compute the

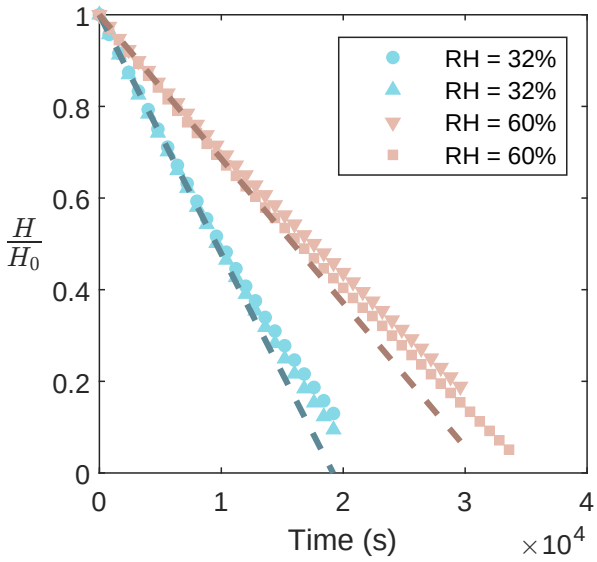

Figure 3.21: Height of the liquid in the capillary normalized by initial height vs. time for two humidity conditions. The initial GO concentration is $\phi_0 \approx 5.7 \times 10^{-5}$. The dashed lines are theoretical predictions from Eqn. 3.7.

velocity of growth of dense particle layer. Figure 3.22 c is a a space-time plot of the intensity over time. The contour line corresponding to the intensity values of 70 visually separates the dense particle layer and the dilute GO suspension. We observe that the dense layer height h scales proportional to $\sqrt{t}$ for long times. In Ref. [166] such dependence was predicted for times for which the fluid interface receded into the particle layer, giving rise to an evaporative mass flux that decreases with increasing h. The growth velocity of the dense particle layer v_{shell} is calculated by a linear fit in the time range where the evaporation rates agree well with the linear diffusive behavior expressed by Eqn. 3.7 (see Fig. 3.21). From mass balance, the packing fraction of the GO at the dense particle layer is $\phi_{shell} \approx (v_c/v_{shell})\phi_0$ [58]. This expression gives $\phi_{shell} = 0.018 \pm 0.004$. The standard deviation is obtained by choosing different values of intensities (70 - 180) to be the threshold for shell layer.

Appendix F: Spray drying experiments

The spray drying experiments are performed in a lab scale spray dryer (Buchi S-300). The initial volume fraction is 0.002 for both acidic and basic suspen-

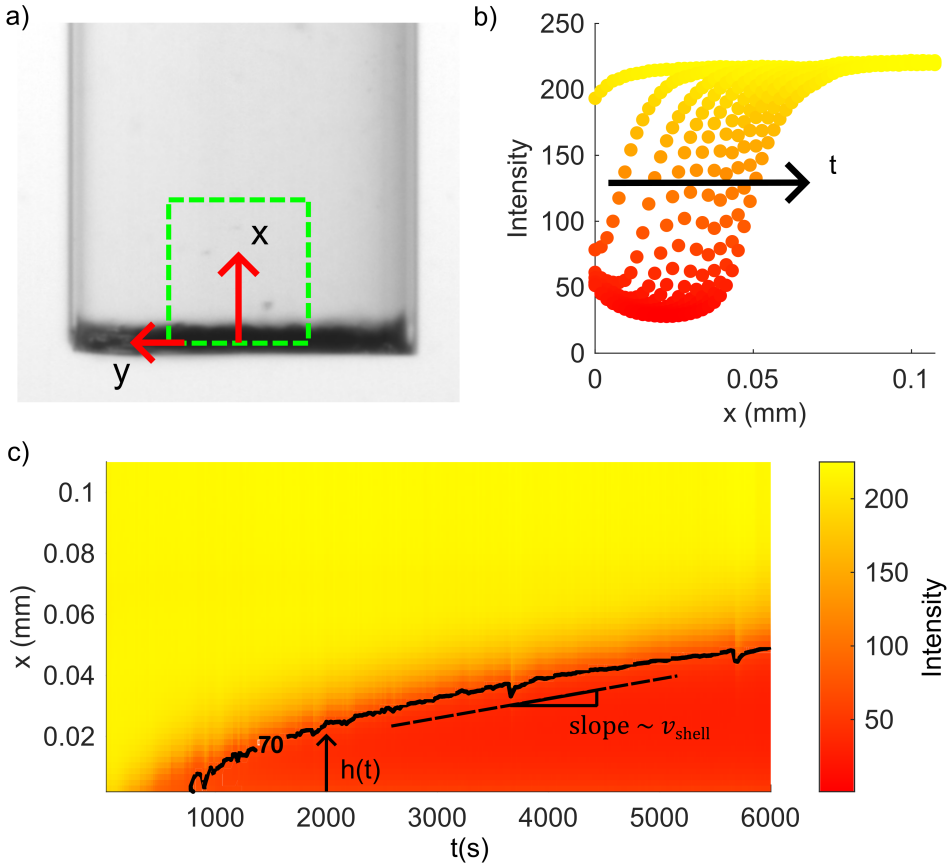

Figure 3.22: a) Image of the open end of the evaporating capillary tube. The green box indicates the area in which light intensity is measured. b) Light intensity in the green box (averaged in the y direction) is plotted against x distance. The arrow indicates the progression in time t. c) Space time plot of the average intensity in the green box over time. The black curve is the contour line corresponding to intensity value 70. The slope of the contour line corresponds to velocity of growth of the dense particle layer v_{shell}.

sions. The suspension is atomized into fine drops of typical radius ≈ 20 μm by a compressed nitrogen at 6 Bars in a spray nozzle. The drops are dried by hot air in a co-flow configuration. The drying air is at 200° Celsius and the air mass flow rate is 30 m^3/hr. Experimental conditions are identical for acidic and basic drops.

Appendix G: Calculation of particle stresses and validation

To compute the average stresses in the bulk of the drop, the drop is divided into n (= 10) shells of equal width δ. The average stress (per unit depth) inside the shell due to particles in the bulk liquid is [167]

$$\sigma^b(r_n) = \frac{1}{A_n}\sum_i\sum_{i\neq j}\vec{F}_{ij}\otimes(\vec{x}_j-\vec{x}_i) + \frac{1}{A_n}\sum_i\vec{F}_{is}\otimes\hat{r}(R-\vec{x}_i\cdot\hat{r}) \tag{3.8}$$

where i is the index of the particles inside the n_{th} shell, r_n is the distance of the shell mid point from the drop center, j is the index of the particles that experience repulsive interaction with particle i and A_n is the area of the n_{th} shell. The symbol $\otimes$ is a dyadic product resulting in a 2 by 2 tensor σ^b. The components are σ^b_{rr}, $\sigma^b_{r\theta}$, $\sigma^b_{\theta r}$ and $\sigma^b_{\theta\theta}$. An equivalent tension (per unit depth) in each shell in θ direction is $\sigma = \sigma^b_{\theta\theta}\delta$. The surface pressure due to particles at the interface is [131]

$$\sigma^s = \frac{1}{P}\sum_i\sum_{i\neq j}\vec{F}_{ij}\otimes(\vec{x}_j-\vec{x}_i). \tag{3.9}$$

Here $P = 2\pi R$ is the perimeter of the drop, i the index of the particles at the drop interface and j is the index of the particles that experience repulsive interaction with particle i. The surface pressure $\Pi = \sigma^s_{\theta\theta}$ is the tangential tension in the interface.

To validate the implementation of the soft potential and calculation of the stresses, we perform simulations of particles inside a circle with periodic boundary conditions. A range of solid volume fractions $(0.005 - 0.84)$ are considered and the isotropic pressure is calculated by averaging over a long time period. In order to compare the data against theoretical models we choose the cutoff length for electrostatic repulsion to be infinitely large (in practice $r_c = 10^6 d_p$). For a system with very large r_c, the isotropic pressure is $P(r_p) \propto F_{p0}/\langle r_p\rangle^3$ [168, 169]. Here $\langle r_p\rangle$ is the average inter-particle distance. Figure 3.23 shows P/P_0 vs. $\langle r_p/r_{p0}\rangle$ for $r_c = 10^6 d_p$. P_0 and $\langle r_{p0}\rangle$ correspond to the isotropic pressure and average inter-particle distance at maximum packing $\phi \approx 0.84$, respectively. The blue dashed line is the theoretical prediction with slope = 1/3.

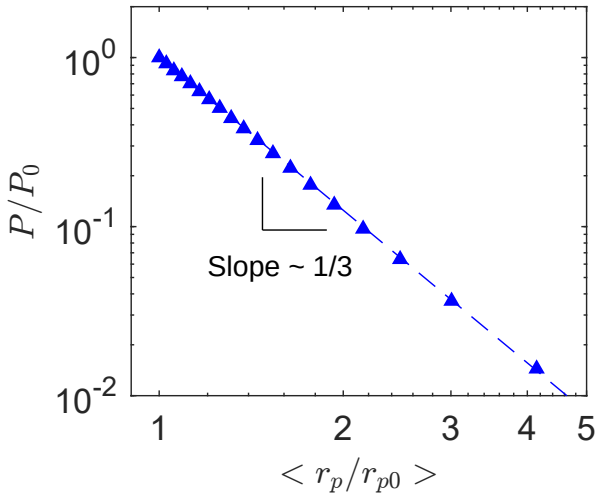

Figure 3.23: Normalized isotropic pressure P/P_0 vs. normalized inter-particle distance $\langle r_p/r_{p0} \rangle$ for $r_c = 10^6 d_p$. The blue dashed line is the theoretical prediction which has a slope of 1/3.

Chapter 4

Conclusions and future work

This chapter begins with a summary of the main conclusions drawn from the experimental and theoretical research presented in this dissertation. We highlight new insights gained on the buckling of monolayers of model plate-like particles and multilayers of nanosheets at fluid interfaces. The need for new rheological studies to quantify stresses in drying suspensions is emphasized and the chapter concludes with a discussion of future research directions.

4.1 Conclusions

The goal of this dissertation is to understand the buckling behavior of monolayers and multilayers of plate-like particles under confinement by fluid interfaces, with the aim of understanding nanosheet mechanics at fluid interfaces. To this end, we first performed experiments with model plate-like particles at fluid-fluid interfaces, as detailed in Chapter 2. Building on insights from the study of monolayer of plate-like particles, Chapter 3 investigates the buckling of multilayers of nanosheets that accumulate near the air-water interface of an evaporating drop. In both chapters, novel experimental techniques were developed to examine the behavior of plate-like particles confined at flat (Langmuir trough) and curved (drops) interfaces. The resulting data provide new insights into how plate-like particles interact at fluid interfaces and highlight differences from the behavior of spherical particles. Based on these experimental findings, mathematical models were developed to describe the buckling response as a function of the physical properties of plate-like particles. The following are the key contributions of this dissertation:

Development of experimental methods

We introduced millimetric sheets as model systems to study the mechanics of 2D nanosheets at interfaces. We showed that Mylar sheets at fluid interfaces produce non-dimensional interface distortions similar to those of 2D nanosheets, making them a suitable model system. The Mylar sheets are monodisperse, optically accessible, and enable controlled, repeatable experiments amenable to theoretical analysis. To characterize the buckled monolayer of Mylar sheets, we designed a custom force sensor to measure the small interfacial forces and developed a novel technique for quantifying the surface topography of buckled monolayers.

In the context of spray drying, we showed that a single drop (GO suspended in water) evaporating on a superhydrophobic substrate is a simplified yet useful model of the spray drying process. The Péclet numbers in the drop evaporation experiments are in the range $150 - 500$, which are comparable to values reported for spray dryers ($Pe \approx 24 - 180$ [61] and $Pe = 5 \times 10^3$ [170]). The advantage of this simplified setup is the ability to directly observe the real-time evolution of the drop shape.

Prediction of buckling wavelength of a monolayer of plate-like particles

Experiments show that monolayers of plate-like particles at fluid interfaces buckle with a wavelength of the order of the particle lateral size L, in contrast to spherical particle monolayers with $\lambda \propto \sqrt{d}$, where d is the diameter of

the spheres [14]. We explained the difference in buckling wavelength scaling based on the bending energy of the particle-laden interface. For monolayers of spherical particle, the bending energy is of the order γd^2 and the buckling wavelength is determined by the balance of bending and capillary energies. Whereas, for plate-like particles, the bending energy is of the order γLt, where t is the thickness of the plate-like particles. For a large aspect ratio $L \gg t$, the bending energy is very small compared to the capillary energy and the buckling wavelength is determined only by capillary energy contributions, which results in buckling wavelength of the order of particle size. We developed a theoretical model that predicts the experimental buckling wavelength and buckling pressure without any fitting parameters.

Buckled monolayers of 2D nanosheets have wavelengths of the order of 10 particle lengths as opposed to model systems with 2 particle lengths [26]. A possible explanation is the presence of bending rigidity in the monolayer due to partial overlaps between plate-like particles. Including overlaps in the mathematical model provides a good prediction of buckling wavelengths observed in monolayers of 2D nanosheets.

Insights on evaporating drops containing nanosheets

Existing models for crumpled capsule formation during spray drying predominantly rely on simulations of evaporating droplets containing single nanosheets [46, 49, 50]. However, experimental studies indicate that dried capsules typically contain multiple nanosheets [45, 48]. Motivated by this knowledge gap we performed experiments to investigate the evaporation of water drops containing multiple GO nanosheets.

The experiments revealed that drop evaporation leads to the formation of a dense layer of GO nanosheets near the air-water interface. Since the formation of a dense layer cannot be directly observed in drop evaporation experiments, we developed complementary experiments involving evaporation of GO suspension in a capillary tube.These capillary experiments enabled the quantification of the solid fraction in the shell layer. The value of shell layer solid fraction was used to estimate the thickness of the shell layer in the drop evaporation experiments.

It may be expected that the accumulation of particles at the interface may reduce the evaporation rate of the suspension drops due to a reduction in surface area available for evaporation. We observed that the evaporation rate remains unchanged. We explain the contradiction by adapting the explanation of Berg and Purcell [142]. The evaporation rate of a spherical drop covered with plate-like particles can be found by solving the Laplace equation for the

vapor concentration field around a spherical surface with uniformly distributed patches that are permeable to diffusion. These patches represent the exposed regions of air-water interface not obstructed by the particles on the drop surface. The evaporation rate remains unchanged if the patches allowing diffusion are uniformly distributed on the surface of the drop and the size of the patches are much smaller than the drop radius.

We have established that a dense layer of GO particles forms near the air-water interface during evaporation and that the shell does not affect the evaporation rate. The next step was to understand the buckling of the shell. We proposed a necessary criterion for buckling of the shell layer in drying drops: $(\gamma - \Pi - \sigma) \approx 0$. Here γ is the interfacial tension, Π is the surface pressure and σ is the tension in the dense layer of particles completely wetted by the fluid. We tested the proposed buckling criterion by varying the interfacial adsorption of GO particles by changing the pH of the suspension. When nanosheets adsorb at the air-water interface, the surface pressure Π is finite and buckling occurs when $(\Pi + \sigma) \approx \gamma$. In case of no particle adsorption, $\Pi \approx 0$ and buckling occurs when $\sigma \approx \gamma$. As a result, the tension σ required for buckling is higher when particle adsorption is absent compared to drops with non-negligible particle adsorption to the air-water interface. The higher tension σ requires the formation of a thicker shell. Since the thickness of the shell increases with time, a delayed onset of buckling is predicted for drops with no particle adsorption at the air-water interface. This prediction agrees well with the experimental results.

We also found that faster evaporation leads to a smaller buckling wavelength for the capsules. This result is explained by earlier jamming at the interface, caused by an increased particle flux towards the fluid interface at higher evaporation rates. As a result, thinner shells of large radius are formed, which, according to elastic shell theory, buckle with smaller wavelengths. The experimental observations are in good agreement with the theoretical predictions.

The pH-dependent interfacial adsorption of GO particles cannot be directly observed in drop evaporation experiments (although the dependence is well-established in the literature [23,66]). Therefore, we performed complementary simulation studies in evaporating 2D drops. The simulations for $Pe \gg 1$ confirmed the observation that the buckling criterion is reached earlier if particle adsorption occurs. For small Pe numbers, the simulations show that a dense layer of particles does not form near the fluid interface and the buckling criterion becomes $(\gamma - \Pi) \approx 0$. The same buckling criterion is valid for evaporation of drops covered with a monolayer of spherical particles [123].

4.2 Future work

4.2.1 Rheology of shell layer in drying suspensions

In Chapter 3, we argued that a necessary condition for buckling is $(\gamma - \Pi - \sigma) \approx 0$. To test this hypothesis, direct measurement of Π and σ in a drying drop would be necessary. Therefore, there is a need for experimental studies that quantify both Π and σ in the shell layer during drying.

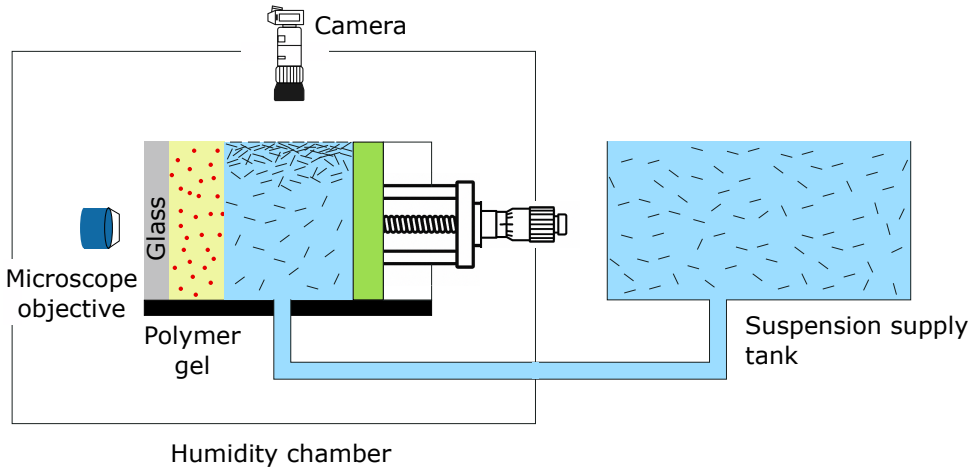

Figure 4.1: Schematic of a conceptual experimental setup proposed to measure the stresses in the shell layer formed by nanosheets during drying.

Figure 4.1 shows a conceptual experimental setup which could be used to study the rheology of shell layer in drying applications. The suspension is dried in a humidity controlled environment between two barriers, one movable and one fixed. The loss of liquid due to evaporation is compensated by using a supply tank with a much larger cross sectional area. As the drying proceeds a dense layer of particles forms at the liquid-gas interface. The movable barrier on the right imposes a prescribed compression displacement on the shell layer. The fixed barrier on the left acts as a stress sensor, which is composed of a polymer gel embedded with fluorescent particles. The tensions Π and σ can be reconstructed by tracking the motion of the fluorescent particles with a microscope objective [171]. The buckling of the interface, if any, can be captured by the camera from the top view. Using this setup, a direct verification of the

proposed buckling criterion is possible.

Predicting the onset of buckling is essential not only for spray dried nanosheets but also for industrial processes such as painting, inkjet printing, coatings, and spray drying of milk powders. While uniform films are desired in printing and coating, wrinkled morphologies are beneficial in applications like spray dried graphene capsules. However, a general framework to understand buckling in complex formulations containing surfactants, polydisperse particles, proteins, and other additives is still lacking. The proposed experimental setup can therefore be instrumental for engineering drying applications.

4.2.2 Buckling of graphene monolayers

In Chapter 2, we show that model plate-like particles buckle with a wavelength of 2 particle diameters. To test the prediction with real nanosheets we performed preliminary experiments with graphene nanosheets in collaboration with Joseph Neilson, Eoin Caffrey and Jonathan Coleman (Chemical Physics of Low-Dimensional Nanostructures, Trinity College Dublin, Ireland).

The graphene sheets are deposited on a water-hexane interface, which has been shown to eliminate overlaps between the sheets [12]. Hexane, being a volatile liquid, evaporates leaving a monolayer of graphene on water-air interface. The monolayer is compressed using Delrin plastic blocks and buckling is observed. The buckled interface is then transferred onto a solid substrate and imaged by SEM. Figure 4.2 shows the SEM images of wrinkled films made from different particle diameters. The three different size classes are produced by cascade centrifugation.

Small wrinkles (shown in insets) and large folds (indicated the by red arrow) are observed in the buckled film. The insets show wrinkles with approximate size of the order of particle diameters for all size classes of graphene, a result qualitatively consistent with the observations made with model plate-like particles and theoretical predictions in Chapter 2. The large folds are attributed to the geometric nonlinearity at large compression displacements and have been reported for spherical particle monolayers [15, 149]. Future work should focus on monolayers composed of size-controlled nanosheets produced via cascade centrifugation. The buckled morphology can be examined by transferring the monolayer onto a solid substrate and imaged using scanning electron microscopy (SEM) or in-situ by employing the get trapping technique [172].

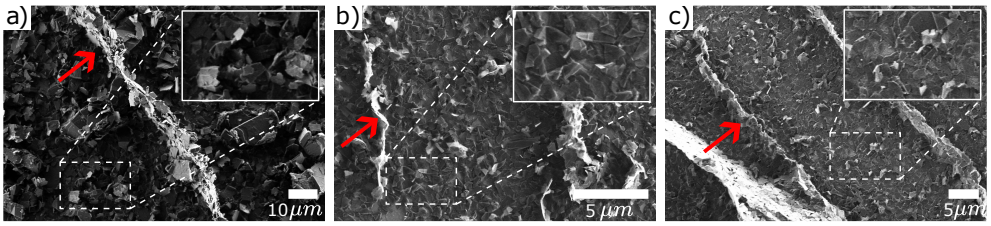

Figure 4.2: Buckled films made from a monolayer of graphene nanosheets. a) Buckled film produced with nanosheets centrifuged at 0.5 krpm, b) buckled film produced with nanosheets centrifuged at 0.5-1 krpm and c) buckled film produced with nanosheets centrifuged at 2-3 krpm. Red arrows show large folds in the buckled films. Insets show relatively flat, zoomed in sections where the corrugations are approximately 2-3 sheet diameters.

Spray coated buckled GO capsules

Spray-dried capsules of graphene oxide, produced in Chapter 3, retain the high surface area of the original nanosheets [46]. These capsules are used as electrodes in energy storage and catalysis applications [11]. However, it is not clear if the high surface area of crumpled capsules is preserved when packed onto a substrate, as in electrode application. To study the packing of cumpled GO capsules, we established a collaboration with Cian Gabbett and Jonathan Coleman (Chemical Physics of Low-Dimensional Nanostructures, Trinity College Dublin, Ireland). We conducted the first study on the microstructure of densely packed crumpled GO capsules. The packing was fabricated by spray-coating a suspension of crumpled GO capsules onto a SiO_2 substrate using a hand spray gun. Figure 4.3 (a) shows a scanning electron microscope image of the top view of the packing. The inset shows a typical crumpled capsule.

Figure 4.3 (b) shows a cross section of the spray coated packing produced by focused ion beam milling made by our collaborator Cian Gabbett. The thickness of the coating is approximately 15 μm. To the best of our knowledge this is the first attempt at visualizing the microstructure. We report the following observations that may be interesting for electrode applications: 1) A highly porous network of crumpled capsules that still retain a high surface area can be produced by spray coating. 2) The corrugated surfaces of the capsules resemble “hook-and-loop fasteners” (similar to Velcro), a feature that could be leveraged to eliminate the need for binders [173].

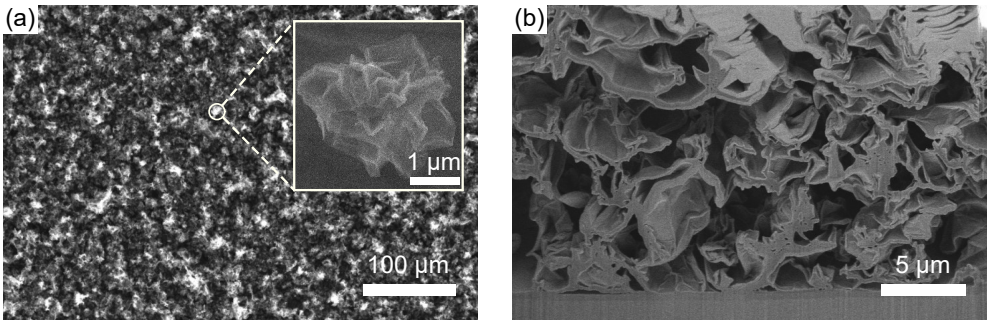

Figure 4.3: Spray coating of a dispersion of crumpled graphene oxide capsules produced by spray drying. (a) SEM image of the top view of the coating. The inset shows the SEM image of an isolated crumpled graphene oxide capsule. (b) SEM image of the cross section of the coating, showing its microstructure.

Evaporating drops with bidispersed particles

In Chapter 3, we used polydispersed GO nanosheets to conduct evaporation experiments. In suspensions containing polydispersed particles, large particles diffuse more slowly than small particles, leading to the formation of a shell layer primarily composed of large particles during evaporation. This behavior is supported by studies on one-dimensional drying of bidispersed particle suspensions [174]. Spray drying has taken advantage of this size-based segregation to fabricate core-shell particles, with small particles forming the core and large particles forming the outer shell [54–56, 175]. Notably, the encapsulation of silicon nanoparticles within a shell of graphene nanosheets has shown great promise as a high-performance anode material for lithium-ion batteries [176]. While unidirectional drying of bidisperse colloidal films has been extensively studied [177], size segregation during the evaporation of droplets remains largely unexplored despite its widespread industrial relevance. Here, we present preliminary simulation results on the evaporation of droplets containing bidispersed particle suspensions.

Figure 4.4 shows the time evolution of particle distribution in an evaporating drop containing two particle size classes. The small particles are ≈ 0.3 μm and the large particles are 1 μm in diameter. The lifetime of the drop ($t_e = 500$ s) is chosen such that the Péclet numbers corresponding to small and large particles are approximately 15 and 46, respectively. The initial drop radius is 100 μm. The interface condition is set to be non-adsorbing for both particle

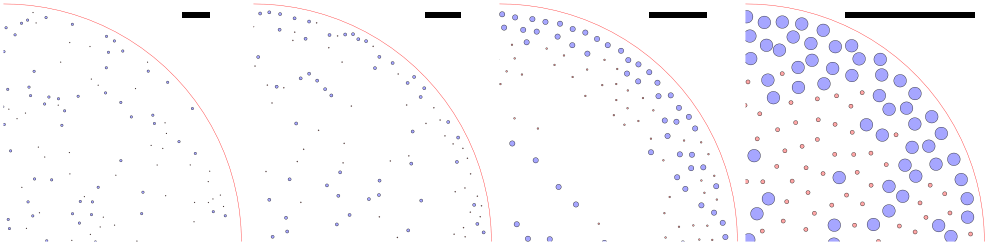

Figure 4.4: Time evolution of particle distribution in an evaporating drop containing two particle size classes. The blue and red particles have diameters of 1 μm and ≈ 0.3 μm, respectively. The normalized time is $\tilde{t} = t/t_e$. All scale bars represent 10 μm.

size classes and there are 200 particles in each size class (a total of 400 particles). The simulations reveal that small particles migrate toward the center, while large particles preferentially accumulate near the air-water interface. Since the interparticle repulsion is independent of particle diameter, the observed size segregation is primarily a consequence of differences in particle diffusivity. We intend to perform additional simulations in the future to gain a better understanding of the formation of core-shell capsules.

Bibliography

[1] A. K. Geim and K. S. Novoselov, "The rise of graphene", Nature materials **6**, 183–191 (2007).

[2] S. Stankovich, D. A. Dikin, G. H. Dommett, K. M. Kohlhaas, E. J. Zimney, E. A. Stach, R. D. Piner, S. T. Nguyen, and R. S. Ruoff, "Graphene-based composite materials", nature **442**, 282–286 (2006).

[3] L. Xiao, J. Damien, J. Luo, H. D. Jang, J. Huang, and Z. He, "Crumpled graphene particles for microbial fuel cell electrodes", Journal of Power Sources **208**, 187–192 (2012).

[4] S. Kalluri, K. H. Seng, Z. Guo, A. Du, K. Konstantinov, H. K. Liu, and S. X. Dou, "Sodium and lithium storage properties of spray-dried molybdenum disulfide-graphene hierarchical microspheres", Scientific Reports **5**, 11989 (2015).

[5] X. Dou, A. R. Koltonow, X. He, H. D. Jang, Q. Wang, Y.-W. Chung, and J. Huang, "Self-dispersed crumpled graphene balls in oil for friction and wear reduction", Proceedings of the National Academy of Sciences **113**, 1528–1533 (2016).

[6] P. Wei, Q. Luo, K. J. Edgehouse, C. M. Hemmingsen, B. J. Rodier, and E. B. Pentzer, "2d particles at fluid–fluid interfaces: assembly and templating of hybrid structures for advanced applications", ACS applied materials & interfaces **10**, 21765–21781 (2018).

[7] E. Pomerantseva, F. Bonaccorso, X. Feng, Y. Cui, and Y. Gogotsi, "Energy storage: The future enabled by nanomaterials", Science **366**, eaan8285 (2019).

[8] C. Arpagaus, A. Collenberg, and D. Rütti, "Laboratory spray drying of materials for batteries, lasers, and bioceramics", Drying Technology **37**, 426–434 (2019).

[9] Y. Tian, Z. Yu, L. Cao, X. L. Zhang, C. Sun, and D.-W. Wang, "Graphene oxide: An emerging electromaterial for energy storage and conversion", Journal of Energy Chemistry **55**, 323–344 (2021).

[10] Y. Wu, W. Wei, R. Yu, L. Xia, X. Hong, J. Zhu, J. Li, L. Lv, W. Chen, Y. Zhao, *et al.*, "Anchoring sub-nanometer Pt clusters on crumpled paper-like mxene enables high hydrogen evolution mass activity", Advanced Functional Materials **32**, 2110910 (2022).

[11] H. Fu and K. A. Gray, "Graphene-encapsulated nanocomposites: Synthesis, environmental applications, and future prospects", Science of The Total Environment 176753 (2024).

[12] J. Neilson, M. P. Avery, and B. Derby, "Tiled monolayer films of 2d molybdenum disulfide nanoflakes assembled at liquid/liquid interfaces", ACS applied materials & interfaces **12**, 25125–25134 (2020).

[13] URL `https://www.graphenea.com/collections/graphene-oxide/products/graphene-oxide-powder`.

[14] D. Vella, P. Aussillous, and L. Mahadevan, "Elasticity of an interfacial particle raft", Europhysics Letters **68**, 212 (2004).

[15] L. Pocivavsek, R. Dellsy, A. Kern, S. Johnson, B. Lin, K. Y. C. Lee, and E. Cerda, "Stress and fold localization in thin elastic membranes", Science **320**, 912–916 (2008).

[16] P. Cicuta and D. Vella, "Granular character of particle rafts", Phys. Rev. Lett. **102**, 138302 (2009).

[17] E. Jambon-Puillet, C. Josserand, and S. Protiere, "Wrinkles, folds, and plasticity in granular rafts", Physical Review Materials **1**, 042601 (2017).

[18] S. Gravelle and L. Botto, "Adsorption of single and multiple graphene-oxide nanoparticles at a water–vapor interface", Langmuir **37**, 13322–13330 (2021).

[19] Y. Hernandez, V. Nicolosi, M. Lotya, F. M. Blighe, Z. Sun, S. De, I. T. McGovern, B. Holland, M. Byrne, Y. K. Gun'Ko, *et al.*, "High-yield production of graphene by liquid-phase exfoliation of graphite", Nature nanotechnology **3**, 563–568 (2008).

[20] V. Nicolosi, M. Chhowalla, M. G. Kanatzidis, M. S. Strano, and J. N. Coleman, "Liquid exfoliation of layered materials", Science **340**, 1226419 (2013).

[21] S. Park and R. S. Ruoff, "Chemical methods for the production of graphenes", Nature nanotechnology **4**, 217–224 (2009).

[22] D. R. Dreyer, S. Park, C. W. Bielawski, and R. S. Ruoff, "The chemistry of graphene oxide", Chemical society reviews **39**, 228–240 (2010).

[23] C.-J. Shih, S. Lin, R. Sharma, M. S. Strano, and D. Blankschtein, "Understanding the pH-dependent behavior of graphene oxide aqueous solutions: a comparative experimental and molecular dynamics simulation study", Langmuir **28**, 235–241 (2012).

[24] B. Audoly and Y. Pomeau, *Elasticity and Geometry: From Hair Curls to the Non-linear Response of Shells* (OUP Oxford) (2010).

[25] L. J. Cote, F. Kim, and J. Huang, "Langmuir- blodgett assembly of graphite oxide single layers", Journal of the American Chemical Society **131**, 1043–1049 (2009).

[26] L. Imperiali, K.-H. Liao, C. Clasen, J. Fransaer, C. W. Macosko, and J. Vermant, "Interfacial rheology and structure of tiled graphene oxide sheets", Langmuir **28**, 7990–8000 (2012).

[27] D. M. Goggin, H. Zhang, E. M. Miller, and J. R. Samaniuk, "Interference provides clarity: direct observation of 2d materials at fluid–fluid interfaces", ACS nano **14**, 777–790 (2019).

[28] R. Aveyard, J. H. Clint, D. Nees, and N. Quirke, "Structure and collapse of particle monolayers under lateral pressure at the octane/aqueous surfactant solution interface", Langmuir **16**, 8820–8828 (2000).

[29] R. A. Wells, H. Johnson, C. R. Lhermitte, S. Kinge, and K. Sivula, "Roll-to-roll deposition of semiconducting 2d nanoflake films of transition metal dichalcogenides for optoelectronic applications", ACS Applied Nano Materials **2**, 7705–7712 (2019).

[30] J. Neilson, E. Caffrey, O. Cassidy, C. Gabbett, K. Synnatschke, E. Schneider, J. M. Munuera, T. Carey, M. Rimmer, Z. Sofer, *et al.*, "Production of ultrathin and high-quality nanosheet networks via layer-by-layer assembly at liquid–liquid interfaces", ACS nano **18**, 32589–32601 (2024).

[31] G. J. Silverberg and C. D. Vecitis, "Wrinkling and periodic folding of graphene oxide monolayers by langmuir–blodgett compression", Langmuir **33**, 9880–9888 (2017).

[32] P. Kralchevsky, I. Ivanov, K. Ananthapadmanabhan, and A. Lips, "On the thermodynamics of particle-stabilized emulsions: curvature effects and catastrophic phase inversion", Langmuir **21**, 50–63 (2005).

[33] P. Kralchevsky and K. Nagayama, *Particles at fluid interfaces and membranes: attachment of colloid particles and proteins to interfaces and formation of two-dimensional arrays*, volume 10 (Elsevier) (2001).

[34] J. Lucassen, "Capillary forces between solid particles in fluid interfaces", Colloids and Surfaces **65**, 131–137 (1992).

[35] P. Singh and D. Joseph, "Fluid dynamics of floating particles", Journal of Fluid Mechanics **530**, 31–80 (2005).

[36] L. Yao, L. Botto, M. Cavallaro Jr, B. J. Bleier, V. Garbin, and K. J. Stebe, "Near field capillary repulsion", Soft Matter **9**, 779–786 (2013).

[37] L. Yao, N. Sharifi-Mood, I. B. Liu, and K. J. Stebe, "Capillary migration of microdisks on curved interfaces", Journal of colloid and interface science **449**, 436–442 (2015).

[38] R. Vehring, "Pharmaceutical particle engineering via spray drying", Pharmaceutical research **25**, 999–1022 (2008).

[39] Y. Fang, S. Rogers, C. Selomulya, and X. D. Chen, "Functionality of milk protein concentrate: Effect of spray drying temperature", Biochemical Engineering Journal **62**, 101–105 (2012).

[40] N. Vogel, S. Utech, G. T. England, T. Shirman, K. R. Phillips, N. Koay, I. B. Burgess, M. Kolle, D. A. Weitz, and J. Aizenberg, "Color from hierarchy: Diverse optical properties of micron-sized spherical colloidal assemblies", Proceedings of the National Academy of Sciences **112**, 10845–10850 (2015).

[41] W. Liu, M. Kappl, and H.-J. Butt, "Tuning the porosity of supraparticles", ACS nano **13**, 13949–13956 (2019).

[42] M. B. Bigdeli and P. A. Tsai, "Making photonic crystals via evaporation of nanoparticle-laden droplets on superhydrophobic microstructures", Langmuir **36**, 4835–4841 (2020).

[43] U. Sultan, A. Götz, C. Schlumberger, D. Drobek, G. Bleyer, T. Walter, E. Löwer, U. A. Peuker, M. Thommes, E. Spiecker, *et al.*, "From meso to macro: Controlling hierarchical porosity in supraparticle powders", Small **19**, 2300241 (2023).

[44] A. V. Shneidman, C. T. Zhang, N. K. Mandsberg, V. C. Picece, E. Shirman, G. K. Paink, N. J. Nicolas, and J. Aizenberg, "Functional supraparticles produced by the evaporation of binary colloidal suspensions on superhydrophobic surfaces", Soft Matter (2024).

[45] J. Luo, H. D. Jang, T. Sun, L. Xiao, Z. He, A. P. Katsoulidis, M. G. Kanatzidis, J. M. Gibson, and J. Huang, "Compression and aggregation-resistant particles of crumpled soft sheets", ACS nano **5**, 8943–8949 (2011).

[46] S. W. Cranford and M. J. Buehler, "Packing efficiency and accessible surface area of crumpled graphene", Physical Review B **84**, 205451 (2011).

[47] D. Parviz, S. D. Metzler, S. Das, F. Irin, and M. J. Green, "Tailored crumpling and unfolding of spray-dried pristine graphene and graphene oxide sheets", Small **11**, 2661–2668 (2015).

[48] W.-N. Wang, Y. Jiang, and P. Biswas, "Evaporation-induced crumpling of graphene oxide nanosheets in aerosolized droplets: confinement force relationship", The journal of physical chemistry letters **3**, 3228–3233 (2012).

[49] X. Ma, M. R. Zachariah, and C. D. Zangmeister, "Crumpled nanopaper from graphene oxide", Nano letters **12**, 486–489 (2012).

[50] Y. Liao, Z. Li, L. Chen, A. B. Croll, and W. Xia, "Crumpling defective graphene sheets", Nano Letters **23**, 3637–3644 (2023).

[51] Q. Liu, Y. Gao, and B. Xu, "Liquid evaporation-driven folding of graphene sheets", Applied Physics Letters **108** (2016).

[52] Q. Liu and B. Xu, "Two-and three-dimensional self-folding of free-standing graphene by liquid evaporation", Soft Matter **14**, 5968–5976 (2018).

[53] Q. Liu, J. Huang, and B. Xu, "Evaporation-driven crumpling and assembling of two-dimensional (2d) materials: A rotational spring–mechanical slider model", Journal of the Mechanics and Physics of Solids **133**, 103722 (2019).

[54] F. Iskandar, Mikrajuddin, and K. Okuyama, "In situ production of spherical silica particles containing self-organized mesopores", Nano Letters **1**, 231–234 (2001).

[55] F. Iskandar, H. Chang, and K. Okuyama, "Preparation of microencapsulated powders by an aerosol spray method and their optical properties", Advanced Powder Technology **14**, 349–367 (2003).

[56] H. Zhou, R. Pujales-Paradela, P. Groppe, S. Wintzheimer, and K. Mandel, "Tuning the morphology of spray-dried supraparticles: Effects of building block size and concentration", Particle & Particle Systems Characterization **39**, 2200127 (2022).

[57] R. Vehring, W. R. Foss, and D. Lechuga-Ballesteros, "Particle formation in spray drying", Journal of aerosol science **38**, 728–746 (2007).

[58] E. Guazzelli and J. F. Morris, *A physical introduction to suspension dynamics*, volume 45 (Cambridge University Press) (2011).

[59] J. Bahadur, D. Sen, S. Mazumder, S. Bhattacharya, H. Frielinghaus, and G. Goerigk, "Origin of buckling phenomenon during drying of micrometer-sized colloidal droplets", Langmuir **27**, 8404–8414 (2011).

[60] N. Tsapis, E. R. Dufresne, S. S. Sinha, C. S. Riera, J. W. Hutchinson, L. Mahadevan, and D. A. Weitz, "Onset of buckling in drying droplets of colloidal suspensions", Physical review letters **94**, 018302 (2005).

[61] J. Archer, J. S. Walker, F. K. Gregson, D. A. Hardy, and J. P. Reid, "Drying kinetics and particle formation from dilute colloidal suspensions in aerosol droplets", Langmuir **36**, 12481–12493 (2020).

[62] M. Milani, T. Phou, C. Ligoure, L. Cipelletti, and L. Ramos, "A double rigidity transition rules the fate of drying colloidal drops", Soft Matter **19**, 6968–6977 (2023).

[63] J. Banhart, "Metal foams: production and stability", Advanced engineering materials **8**, 781–794 (2006).

[64] A. Stocco, E. Rio, B. P. Binks, and D. Langevin, "Aqueous foams stabilized solely by particles", Soft Matter **7**, 1260–1267 (2011).

[65] S. Lam, K. P. Velikov, and O. D. Velev, "Pickering stabilization of foams and emulsions with particles of biological origin", Current Opinion in Colloid & Interface Science **19**, 490–500 (2014).

[66] L. J. Cote, J. Kim, Z. Zhang, C. Sun, and J. Huang, "Tunable assembly of graphene oxide surfactant sheets: wrinkles, overlaps and impacts on thin film properties", Soft Matter **6**, 6096–6101 (2010).

[67] S. Prakash, H. Perrin, and L. Botto, "Buckling of a monolayer of platelike particles trapped at a fluid-fluid interface", Physical Review E **109**, 014801 (2024).

[68] B. P. Binks, "Particles as surfactants—similarities and differences", Current opinion in colloid & interface science **7**, 21–41 (2002).

[69] S. P. Ogilvie, M. J. Large, M. A. O'Mara, P. J. Lynch, C. L. Lee, A. A. King, C. Backes, and A. B. Dalton, "Size selection of liquid-exfoliated 2d nanosheets", 2D Materials **6**, 031002 (2019).

[70] L. Botto, E. P. Lewandowski, M. Cavallaro, and K. J. Stebe, "Capillary interactions between anisotropic particles", Soft Matter **8**, 9957–9971 (2012).

[71] M. Vis, J. Opdam, I. S. Van't Oor, G. Soligno, R. Van Roij, R. H. Tromp, and B. H. Erné, "Water-in-water emulsions stabilized by nanoplates", ACS Macro Letters **4**, 965–968 (2015).

[72] A. Fahimi, I. Jurewicz, R. J. Smith, C. S. Sharrock, D. A. Bradley, S. J. Henley, J. N. Coleman, and A. B. Dalton, "Density controlled conductivity of pristine graphene films", Carbon **64**, 435–443 (2013).

[73] S. J. Woltornist, A. J. Oyer, J.-M. Y. Carrillo, A. V. Dobrynin, and D. H. Adamson, "Conductive thin films of pristine graphene by solvent interface trapping", ACS nano **7**, 7062–7066 (2013).

[74] S. Biswas and L. T. Drzal, "A novel approach to create a highly ordered monolayer film of graphene nanosheets at the liquid- liquid interface", Nano letters **9**, 167–172 (2009).

[75] G. J. Silverberg, A. A. McClelland, S. Griesse-Nascimento, C. Girabawe, J. P. Kadow, L. Mahadevan, and C. D. Vecitis, "Controlling the roughness of langmuir–blodgett monolayers", The Journal of Physical Chemistry B **121**, 5078–5085 (2017).

[76] S. Protière, "Particle rafts and armored droplets", Annual Review of Fluid Mechanics **55**, 459–480 (2023).

[77] S. Razavi, K. D. Cao, B. Lin, K. Y. C. Lee, R. S. Tu, and I. Kretzschmar, "Collapse of particle-laden interfaces under compression: buckling vs particle expulsion", Langmuir **31**, 7764–7775 (2015).

[78] F. Boyer, O. Pouliquen, and É. Guazzelli, "Dense suspensions in rotating-rod flows: normal stresses and particle migration", Journal of Fluid Mechanics **686**, 5–25 (2011).

[79] H. Perrin, M. Wyart, B. Metzger, and Y. Forterre, "Nonlocal effects reflect the jamming criticality in frictionless granular flows down inclines", Phys. Rev. Lett. **126**, 228002 (2021).

[80] M. Backholm and O. Bäumchen, "Micropipette force sensors for in vivo force measurements on single cells and multicellular microorganisms", Nature protocols **14**, 594–615 (2019).

[81] D. Vella and L. Mahadevan, "The "cheerios effect"", American journal of physics **73**, 817–825 (2005).

[82] T. I. Hesla and D. D. Joseph, "The maximum contact angle at the rim of a heavy floating disk", Journal of colloid and interface science **279**, 186–191 (2004).

[83] S. Timoshenko and J. Gere, "Theory of elastic stability mcgraw-hill, 1961", (2009).

[84] N. Taccoen, F. Lequeux, D. Z. Gunes, and C. N. Baroud, "Probing the mechanical strength of an armored bubble and its implication to particle-stabilized foams", Physical Review X **6**, 011010 (2016).

[85] O. Saavedra V., H. Elettro, and F. Melo, "Progressive friction mobilization and enhanced janssen's screening in confined granular rafts", Phys. Rev. Mater. **2**, 043603 (2018).

[86] B. Andreotti, Y. Forterre, and O. Pouliquen, *Granular media: between fluid and solid* (Cambridge University Press) (2013).

[87] D. Vella, A. Boudaoud, and M. Adda-Bedia, "Statics and inertial dynamics of a ruck in a rug", Phys. Rev. Lett. **103**, 174301 (2009).

[88] I. Jorjadze, L.-L. Pontani, and J. Brujic, "Microscopic approach to the nonlinear elasticity of compressed emulsions", Phys. Rev. Lett. **110**, 048302 (2013).

[89] T. S. Majmudar and R. P. Behringer, "Contact force measurements and stress-induced anisotropy in granular materials", nature **435**, 1079–1082 (2005).

[90] D. M. Mueth, H. M. Jaeger, and S. R. Nagel, "Force distribution in a granular medium", Phys. Rev. E **57**, 3164–3169 (1998).

[91] R. P. Behringer and B. Chakraborty, "The physics of jamming for granular materials: a review", Reports on Progress in Physics **82**, 012601 (2018).

[92] J. F. Peters, M. Muthuswamy, J. Wibowo, and A. Tordesillas, "Characterization of force chains in granular material", Phys. Rev. E **72**, 041307 (2005).

[93] D. M. Goggin, R. Bei, R. Anderson, D. A. Gómez-Gualdrón, and J. R. Samaniuk, "Stacking of monolayer graphene particles at a water–vapor interface", The Journal of Physical Chemistry C **125**, 7880–7888 (2021).

[94] J. E. Jones, "On the determination of molecular fields.—ii. from the equation of state of a gas", Proceedings of the Royal Society of London. Series A, Containing Papers of a Mathematical and Physical Character **106**, 463–477 (1924).

[95] A. Lerf, A. Buchsteiner, J. Pieper, S. Schöttl, I. Dekany, T. Szabo, and H. Boehm, "Hydration behavior and dynamics of water molecules in graphite oxide", Journal of Physics and Chemistry of Solids **67**, 1106–1110 (2006).

[96] T. Dyer, N. Thamwattana, and R. Jalili, "Modelling the interaction of graphene oxide using an atomistic-continuum model", RSC advances **5**, 77062–77070 (2015).

[97] R. A. Soler-Crespo, W. Gao, L. Mao, H. T. Nguyen, M. R. Roenbeck, J. T. Paci, J. Huang, S. T. Nguyen, and H. D. Espinosa, "The role of water in mediating interfacial adhesion and shear strength in graphene oxide", ACS nano **12**, 6089–6099 (2018).

[98] C.-h. Liu, S. R. Nagel, D. Schecter, S. Coppersmith, S. Majumdar, O. Narayan, and T. Witten, "Force fluctuations in bead packs", Science **269**, 513–515 (1995).

[99] S. N. Coppersmith, C. h. Liu, S. Majumdar, O. Narayan, and T. A. Witten, "Model for force fluctuations in bead packs", Phys. Rev. E **53**, 4673–4685 (1996).

[100] M. Cavallaro Jr, L. Botto, E. P. Lewandowski, M. Wang, and K. J. Stebe, "Curvature-driven capillary migration and assembly of rod-like particles", Proceedings of the National Academy of Sciences **108**, 20923–20928 (2011).

[101] T. Carey, O. Cassidy, K. Synnatschke, E. Caffrey, J. Garcia, S. Liu, H. Kaur, A. G. Kelly, J. Munuera, C. Gabbett, *et al.*, "High-mobility flexible transistors with low-temperature solution-processed tungsten dichalcogenides", ACS nano **17**, 2912–2922 (2023).

[102] J. Kim, L. J. Cote, F. Kim, W. Yuan, K. R. Shull, and J. Huang, "Graphene oxide sheets at interfaces", Journal of the American Chemical Society **132**, 8180–8186 (2010).

[103] Y. Chen, F. Guo, A. Jachak, S.-P. Kim, D. Datta, J. Liu, I. Kulaots, C. Vaslet, H. D. Jang, J. Huang, *et al.*, "Aerosol synthesis of cargo-filled graphene nanosacks", Nano letters **12**, 1996–2002 (2012).

[104] C.-J. Shih, S. Lin, M. S. Strano, and D. Blankschtein, "Understanding the stabilization of liquid-phase-exfoliated graphene in polar solvents: molecular dynamics simulations and kinetic theory of colloid aggregation", Journal of the American Chemical Society **132**, 14638–14648 (2010).

[105] A. Agrawal, S. Gravelle, C. Kamal, and L. Botto, "Viscous peeling of a nanosheet", Soft matter **18**, 3967–3980 (2022).

[106] J. M. Stockie and S. I. Green, "Simulating the motion of flexible pulp fibres using the immersed boundary method", Journal of Computational Physics **147**, 147–165 (1998).

[107] S. Prakash, E. Krolis, A. Marin, and L. Botto, "Evaporation driven buckling of a drop laden with graphene oxide nanosheets", Soft matter (2025).

[108] L. Pauchard and Y. Couder, "Invagination during the collapse of an inhomogeneous spheroidal shell", Europhysics Letters **66**, 667 (2004).

[109] J. Perdana, M. B. Fox, M. A. Schutyser, and R. M. Boom, "Mimicking spray drying by drying of single droplets deposited on a flat surface", Food and Bioprocess Technology **6**, 964–977 (2013).

[110] C. Liu, Z. Yu, D. Neff, A. Zhamu, and B. Z. Jang, "Graphene-based supercapacitor with an ultrahigh energy density", Nano letters **10**, 4863–4868 (2010).

[111] W. M. El Rouby, "Crumpled graphene: preparation and applications", RSC advances **5**, 66767–66796 (2015).

[112] L. Chen and J. R. Evans, "Drying of colloidal droplets on superhydrophobic surfaces", Journal of colloid and interface science **351**, 283–287 (2010).

[113] Á. G. Marín, H. Gelderblom, A. Susarrey-Arce, A. van Houselt, L. Lefferts, J. G. Gardeniers, D. Lohse, and J. H. Snoeijer, "Building microscopic soccer balls with evaporating colloidal fakir drops", Proceedings of the National Academy of Sciences **109**, 16455–16458 (2012).

[114] C. Seyfert, E. J. Berenschot, N. R. Tas, A. Susarrey-Arce, and A. Marin, "Evaporation-driven colloidal cluster assembly using droplets on superhydrophobic fractal-like structures", Soft matter **17**, 506–515 (2021).

[115] S. Mao, Z. Wen, H. Kim, G. Lu, P. Hurley, and J. Chen, "A general approach to one-pot fabrication of crumpled graphene-based nanohybrids for energy applications", ACS nano **6**, 7505–7513 (2012).

[116] H. Yang, Y. Wang, Y. Song, L. Qiu, S. Zhang, D. Li, and X. Zhang, "Assembling of graphene oxide in an isolated dissolving droplet", Soft Matter **8**, 11249–11254 (2012).

[117] C. S. Handscomb and M. Kraft, "Simulating the structural evolution of droplets following shell formation", Chemical Engineering Science **65**, 713–725 (2010).

[118] L. Pauchard, M. Mermet-Guyennet, and F. Giorgiutti-Dauphiné, "Invagination process induced by 2D desiccation of colloidal solutions", Chemical Engineering and Processing: Process Intensification **50**, 483–485 (2011).

[119] F. Boulogne, F. Giorgiutti-Dauphiné, and L. Pauchard, "The buckling and invagination process during consolidation of colloidal droplets", Soft Matter **9**, 750–757 (2013).

[120] E. Lintingre, G. Ducouret, F. Lequeux, L. Olanier, T. Périé, and L. Talini, "Controlling the buckling instability of drying droplets of suspensions through colloidal interactions", Soft Matter **11**, 3660–3665 (2015).

[121] D. Sen, S. Mazumder, J. Melo, A. Khan, S. Bhattyacharya, and S. D'souza, "Evaporation driven self-assembly of a colloidal dispersion during spray drying: volume fraction dependent morphological transition", Langmuir **25**, 6690–6695 (2009).

[122] V. Poulichet and V. Garbin, "Cooling particle-coated bubbles: destabilization beyond dissolution arrest", Langmuir **31**, 12035–12042 (2015).

[123] C. Gu and L. Botto, "Buckling vs. particle desorption in a particle-covered drop subject to compressive surface stresses: a simulation study", Soft matter **14**, 711–724 (2018).

[124] M. Sperling, P. Papadopoulos, and M. Gradzielski, "Understanding the formation of anisometric supraparticles: a mechanistic look inside droplets drying on a superhydrophobic surface", Langmuir **32**, 6902–6908 (2016).

[125] S. Barwich and M. E. Möbius, "The elastic response of graphene oxide gels as a crumpling phenomenon", Soft Matter **18**, 8223–8228 (2022).

[126] J. W. Suk, R. D. Piner, J. An, and R. S. Ruoff, "Mechanical properties of monolayer graphene oxide", ACS nano **4**, 6557–6564 (2010).

[127] Z. Xu and C. Gao, "Aqueous liquid crystals of graphene oxide", ACS nano **5**, 2908–2915 (2011).

[128] S. Naficy, R. Jalili, S. H. Aboutalebi, R. A. Gorkin III, K. Konstantinov, P. C. Innis, G. M. Spinks, P. Poulin, and G. G. Wallace, "Graphene oxide dispersions: tuning rheology to enable fabrication", Materials Horizons **1**, 326–331 (2014).

[129] J. Sherwood, "Resistance coefficients for stokes flow around a disk with a navier slip condition", Physics of Fluids **24**, 093103 (2012).

[130] F. Toschi and M. Sega, *Flowing matter* (Springer Nature) (2019).

[131] C. Gu and L. Botto, "Direct calculation of anisotropic surface stresses during deformation of a particle-covered drop", Soft matter **12**, 705–716 (2016).

[132] S. K. Sainis, V. Germain, C. O. Mejean, and E. R. Dufresne, "Electrostatic interactions of colloidal particles in nonpolar solvents: Role of surface chemistry and charge control agents", Langmuir **24**, 1160–1164 (2008).

[133] I. Langmuir, "The evaporation of small spheres", Physical review **12**, 368 (1918).

[134] Y. Liu, M. Xu, L. M. Portela, and V. Garbin, "Diffusion across particle-laden interfaces in pickering droplets", Soft Matter **20**, 94–102 (2024).

[135] G. G. J. Bange, "On the quantitative explanation of stomatal transpiration", Acta Botanica Neerlandica **2**, 255–297 (1953).

[136] J. R. Cooke, "Some theoretical considerations in stomatal diffusion: A field theory approach", Acta Biotheoretica **17**, 95–124 (1967).

[137] M. Suzuki and S. Maeda, "On the mechanism of drying of granular beds mass transfer from discontinuous source", Journal of chemical engineering of Japan **1**, 26–31 (1968).

[138] E.-U. Schlünder, "On the mechanism of the constant drying rate period and its relevance to diffusion controlled catalytic gas phase reactions", Chemical Engineering Science **43**, 2685–2688 (1988).

[139] P. S. Epstein and M. S. Plesset, "On the stability of gas bubbles in liquid-gas solutions", The Journal of Chemical Physics **18**, 1505–1509 (1950).

[140] C. B. Muratov and S. Y. Shvartsman, "Boundary homogenization for periodic arrays of absorbers", Multiscale Modeling & Simulation **7**, 44–61 (2008).

[141] A. J. Bernoff and A. E. Lindsay, "Numerical approximation of diffusive capture rates by planar and spherical surfaces with absorbing pores", SIAM Journal on Applied Mathematics **78**, 266–290 (2018).

[142] H. C. Berg and E. M. Purcell, "Physics of chemoreception", Biophysical journal **20**, 193–219 (1977).

[143] E. Shahraeeni, P. Lehmann, and D. Or, "Coupling of evaporative fluxes from drying porous surfaces with air boundary layer: Characteristics of evaporation from discrete pores", Water Resources Research **48** (2012).

[144] L. J. Roemling, G. De Angelis, A. Mauch, E. Amstad, and N. Vogel, "Control of buckling of colloidal supraparticles", arXiv preprint arXiv:2409.00602 (2024).

[145] S. I. Kam and W. R. Rossen, "Anomalous capillary pressure, stress, and stability of solids-coated bubbles", Journal of Colloid and Interface Science **213**, 329–339 (1999).

[146] M. Abkarian, A. B. Subramaniam, S.-H. Kim, R. J. Larsen, S.-M. Yang, and H. A. Stone, "Dissolution arrest and stability of particle-covered bubbles", Physical review letters **99**, 188301 (2007).

[147] C. Monteux, J. Kirkwood, H. Xu, E. Jung, and G. G. Fuller, "Determining the mechanical response of particle-laden fluid interfaces using surface pressure isotherms and bulk pressure measurements of droplets", Physical chemistry chemical physics **9**, 6344–6350 (2007).

[148] P. J. Beltramo, M. Gupta, A. Alicke, I. Liascukiene, D. Z. Gunes, C. N. Baroud, and J. Vermant, "Arresting dissolution by interfacial rheology design", Proceedings of the National Academy of Sciences **114**, 10373–10378 (2017).

[149] K. D. Danov, P. A. Kralchevsky, and S. D. Stoyanov, "Elastic langmuir layers and membranes subjected to unidirectional compression: wrinkling and collapse", Langmuir **26**, 143–155 (2010).

[150] L. Sagis, "Generalized surface momentum balances for the analysis of surface dilatational data", The European Physical Journal Special Topics **222**, 31–38 (2013).

[151] J. Paulose and D. R. Nelson, "Buckling pathways in spherical shells with soft spots", Soft Matter **9**, 8227–8245 (2013).

[152] J. W. Hutchinson, "Buckling of spherical shells revisited", Proceedings of the Royal Society A: Mathematical, Physical and Engineering Sciences **472**, 20160577 (2016).

[153] J. K. Beattie, A. M. Djerdjev, A. Gray-Weale, N. Kallay, J. Lützenkirchen, T. Preočanin, and A. Selmani, "pH and the surface tension of water", Journal of colloid and interface science **422**, 54–57 (2014).

[154] J. W. Hutchinson, "Imperfection Sensitivity of Externally Pressurized Spherical Shells", Journal of Applied Mechanics **34**, 49–55 (1967).

[155] S. S. Datta, S.-H. Kim, J. Paulose, A. Abbaspourrad, D. R. Nelson, and D. A. Weitz, "Delayed buckling and guided folding of inhomogeneous capsules", Physical review letters **109**, 134302 (2012).

[156] A. Abramian, E. Virot, E. Lozano, S. M. Rubinstein, and T. M. Schneider, "Nondestructive prediction of the buckling load of imperfect shells", Physical Review Letters **125**, 225504 (2020).

[157] A. Lee, F. López Jiménez, J. Marthelot, J. W. Hutchinson, and P. M. Reis, "The geometric role of precisely engineered imperfections on the critical buckling load of spherical elastic shells", Journal of Applied Mechanics **83**, 111005 (2016).

[158] F. Derveni, W. Gueissaz, D. Yan, and P. M. Reis, "Probabilistic buckling of imperfect hemispherical shells containing a distribution of defects", Philosophical Transactions of the Royal Society A **381**, 20220298 (2023).

[159] J. Gladden, N. Handzy, A. Belmonte, and E. Villermaux, "Dynamic buckling and fragmentation in brittle rods", Physical review letters **94**, 035503 (2005).

[160] F. Box, O. Kodio, D. O'Kiely, V. Cantelli, A. Goriely, and D. Vella, "Dynamic buckling of an elastic ring in a soap film", Physical Review Letters **124**, 198003 (2020).

[161] A. Sarkar and M. S. Tirumkudulu, "Consolidation of charged colloids during drying", Langmuir **25**, 4945–4953 (2009).

[162] K. Roger and J. J. Crassous, "How the interplay of molecular and colloidal scales controls drying of microgel dispersions", Proceedings of the National Academy of Sciences **118**, e2105530118 (2021).

[163] L. T. Raju, C. Diddens, J. Rodríguez-Rodríguez, M. N. Van Der Linden, X. Zhang, D. Lohse, and U. Sen, "Evaporation of binary liquids from a capillary tube", Journal of Fluid Mechanics **983**, A21 (2024).

[164] S. Knoche and J. Kierfeld, "Buckling of spherical capsules", Physical Review E—Statistical, Nonlinear, and Soft Matter Physics **84**, 046608 (2011).

[165] H. Sun, J. Zhu, D. Baumann, L. Peng, Y. Xu, I. Shakir, Y. Huang, and X. Duan, "Hierarchical 3d electrodes for electrochemical energy storage", Nature Reviews Materials **4**, 45–60 (2019).

[166] H. Pingulkar and J.-B. Salmon, "Confined directional drying of a colloidal dispersion: kinetic modeling", Soft Matter **19**, 2176–2185 (2023).

[167] P. R. Nott, E. Guazzelli, and O. Pouliquen, "The suspension balance model revisited", Physics of Fluids **23** (2011).

[168] P. A. Kralchevsky, K. D. Danov, and P. V. Petkov, "Soft electrostatic repulsion in particle monolayers at liquid interfaces: surface pressure and effect of aggregation", Philosophical Transactions of the Royal Society A: Mathematical, Physical and Engineering Sciences **374**, 20150130 (2016).

[169] C. van Baalen, J. Vialetto, and L. Isa, "Tuning electrostatic interactions of colloidal particles at oil-water interfaces with organic salts", Physical Review Letters **131**, 128202 (2023).

[170] E. Lintingre, F. Lequeux, L. Talini, and N. Tsapis, "Control of particle morphology in the spray drying of colloidal suspensions", Soft Matter **12**, 7435–7444 (2016).

[171] S. A. Maskarinec, C. Franck, D. A. Tirrell, and G. Ravichandran, "Quantifying cellular traction forces in three dimensions", Proceedings of the National Academy of Sciences **106**, 22108–22113 (2009).

[172] V. N. Paunov, "Novel method for determining the three-phase contact angle of colloid particles adsorbed at air- water and oil- water interfaces", Langmuir **19**, 7970–7976 (2003).

[173] H. Chen, M. Ling, L. Hencz, H. Y. Ling, G. Li, Z. Lin, G. Liu, and S. Zhang, "Exploring chemical, mechanical, and electrical functionalities of binders for advanced energy-storage devices", Chemical reviews **118**, 8936–8982 (2018).

[174] J. Zhou, Y. Jiang, and M. Doi, "Cross interaction drives stratification in drying film of binary colloidal mixtures", Physical review letters **118**, 108002 (2017).

[175] H. Chang and K. Okuyama, "Optical properties of dense and porous spheroids consisting of primary silica nanoparticles", Journal of aerosol science **33**, 1701–1720 (2002).

[176] J. Luo, X. Zhao, J. Wu, H. D. Jang, H. H. Kung, and J. Huang, "Crumpled graphene-encapsulated si nanoparticles for lithium ion battery anodes", The journal of physical chemistry letters **3**, 1824–1829 (2012).

[177] M. Schulz and J. Keddie, "A critical and quantitative review of the stratification of particles during the drying of colloidal films", Soft matter **14**, 6181–6197 (2018).

Acknowledgements

During my Ph.D. journey, one of the most valuable lessons I learned about myself is how deeply I enjoy learning and conducting research. For this, I am grateful to my supervisor, *Dr. Lorenzo Botto*, who made it all possible. He first offered me the opportunity to pursue a Ph.D. after a casual conversation about my master's project, a moment that truly surprised me. His door was always open, and what began as a "quick five-minute chat" often turned into half-hour scientific debates (for which I apologize). From Lorenzo, I learned not only how to conduct research, but also how to communicate it clearly and to think critically about questions worth pursuing. He took his role as a Ph.D. advisor with great seriousness, guiding me not only towards a successful doctoral thesis but also preparing me thoroughly for a future career in research. I am especially grateful that his mentorship continues, both scientifically and personally, even beyond my Ph.D. journey.

Special thanks to *Prof. Johan Padding* for serving as my co-promoter and for fostering a pleasant and stimulating atmosphere within the Complex Fluid Processing group. I am also grateful to you and the other committee members for dedicating your time to carefully reading my thesis.

Thanks to *Dr. Hugo Perrin*, who served as my daily supervisor during the first two years of my Ph.D., and from whom I had the privilege of learning the Euler–Lagrange minimization technique. I also thank *Dr. Heng Li* for many stimulating discussions on Stokesian dynamics.

I am also grateful for my collaboration with *Prof. Alvaro Marin* at the University of Twente and his student *Eva Krolis*, whose contributions were essential for Chapter 3 of this thesis. My visit to Alvaro's lab was especially enriching, as I gained valuable insights into evaporation-driven flows. Likewise, my visit to Trinity College Dublin and my collaboration with *Prof. Jonathan Coleman* was highly rewarding, resulting in beautiful SEM images of buckled graphene oxide, one of which now appears on the cover of this thesis.

I also thank *Dr. Simon Gravelle*, *Dr. Paul Grandgeorge*, and *Dr. Adyant*

Agarwal for valuable discussions related to Chapter 2. I am grateful to *Prof. John Hutchinson* for insightful exchanges on shell buckling, to *Prof. Valeria Garbin* for her perspectives on mass transfer across particle-laden interfaces, and once again to *Prof. Jonathan Coleman* for his help with AFM. In addition, I thank *Dr. Emma Hinderink*, *Dr. Hugo Perrin*, *Dr. Alexander Oratis*, and *Rumen Georgiev* for their suggestions on Chapter 3. Finally, I am grateful to *Prof. Thijs Vlugt*, *Dr. Remco Hartkamp*, *Jelle Lagerweij*, and *Darshan Raju* for their helpful input on the simulations of evaporating drops.

My time at P&E was especially enjoyable thanks to my old and new office mates: *Marko, Rishab, Hugo, Heng, Mengmeng, Zero, Irem, Darshan, Sofen, Sannath, Tarun, Letizia, Shaina, Giando*, and *Baptiste*. I am particularly grateful to Giando and Baptiste for always indulging my many questions about simulating particle-laden flows. I also enjoyed spending time with other colleagues in the department, including *Vignesh Murugesan, Arvind Pari, Lorenzo Casagli, An Qi, Sowmya Kumar, Nagaraj Nagalingam, Abhirath Anand, Ning Ji*, and *Lyke van Dalen*.

It is a pleasure to thank my paranymphs, *Marko* and *Xiao*, for their support. Thank you *Marko* for running the marathon with me from the very beginning and for dedicating your proposition number 7 to me. I am equally grateful to *Xiao* and *Floor* for making me feel at home in the Netherlands.

I had the privilege of serving on the PhD Council and as a D&I Ambassador. In these roles, I worked with *Iris, Anna, Vasu, Niharika, Gilles, Jose, Vishal, Jette, Emma, Pedro*, and many others, who inspired me and with whom I collaborated (sometimes successfully, sometimes less so) to make the faculty a more inclusive space. Special thanks go to *Saloum Darboe*, whose dedication and grace made what often felt like a losing battle seem achievable.

I am indebted to the teachers who first inspired me to do research. For my master's thesis, I am grateful to *Dr. Wim-Paul Breugem* and *Dr. Burak Eral*. For my bachelor's thesis, I thank *Prof. Madhu Ganesh*, whose guidance and influence were crucial in shaping my decision to follow this path.

On a personal note, I thank my mom, *Manimegalai*, my unwavering supporter, from whom I draw all my confidence. I am grateful to my sisters, *Neeraja, Swetha, Ashrutha*, and *Srinidhi*, and to my brother, *Ashwanth*, for keeping life outside of research lively. I also thank my father, extended family, and grandparents for their support throughout my education. Thank you *Koen and Nienke* for welcoming me with open arms. Finally, many hugs to my partner *Jip* for her constant love, (im)patience, and enthusiasm.

Bio

Suriyaprakash was born in Cuddalore, Tamil Nadu, India. He earned his Bachelor's degree in Mechanical Engineering from PSG College of Technology, Coimbatore, graduating First Class with Distinction. For his bachelor thesis, he worked at the Indian Space Research Organization (ISRO). He then pursued a Master's degree in Energy, Flow and Process Technology at Delft University of Technology, The Netherlands, graduating cum laude. In his Master's thesis, he studied liquid jet instabilities. By systematically tuning the process parameters, he was able to control jet instabilities to reduce the production of satellite drops. In November 2020, he began his Ph.D. in the Process and Energy Department at TU Delft. His research focused on studying instabilities at fluid-fluid interfaces with adsorbed 2D nanosheets. By combining experiments, theoretical models, and simulations, he investigated how these instabilities can be understood and ultimately controlled to design functional 3D nanostructures. Alongside his research, he served as a member of the Ph.D. Council and acted as the Diversity and Inclusion Ambassador for the Faculty of Mechanical Engineering, contributing to initiatives for a more inclusive academic environment. Following his Ph.D., he joined the Applied Physics Department at Eindhoven University of Technology as a postdoctoral researcher, where he investigates bacteria-driven instabilities in evaporating drops, continuing his passion for understanding and controlling fluid instabilities.

Scientific output

Publications within this dissertation

1. Suriya Prakash, Eva Krolis, Alvaro Marin and Lorenzo Botto (2025). Evaporation driven buckling of drops laden with graphene oxide nanosheets. *Soft Matter*.

2. Suriya Prakash, Hugo Perrin, and Lorenzo Botto (2024). Buckling of a monolayer of platelike particles trapped at a fluid-fluid interface. *Physical Review E*, 109 (1), 014801.

Publications outside this dissertation

1. Yavuz Kamis, Suriya Prakash, Wim-Paul Breugem, and Burak Eral (2023). Controlling the breakup of spiralling jets: results from experiments, nonlinear simulations and linear stability analysis. *Journal of Fluid Mechanics*, 956, p.A24.

2. Heng Li, Lucas Beetsma, Suriya Prakash, Maurice Mikkers and Lorenzo Botto (2023). Analysis and optimization of a multicascade method for the size fractionation of poly-dispersed particle systems via sedimentation or centrifugation. *arXiv*, 2303.05257.

3. Arun Kumar Ramasamy, Madhu Ganesh, Suriya Prakash, and Keerthivasan Rajamani. (2023). Design and performance investigation of modified hybrid parabolic linear fresnel collector. *Energy for Sustainable Development*, 76, 101273.

4. Venkatesh R, Madhu Ganesh, Suriya Prakash, Deva Surya, Ashok Kumar, and Rudramoorthy R.. (2021). Experimental and simulation study of the performance of a desiccant loop cooling system. *Proceedings of the Institution of Mechanical Engineers, Part A: Journal of Power and Energy*, 235(8), pp.1914-1932.